2011

Dynamics and kinematics of eruptive activity at Fuego volcano, Guatemala 2005-2009

John J. Lyons
Michigan Technological University

DYNAMICS AND KINEMATICS OF ERUPTIVE ACTIVITY AT FUEGO VOLCANO, GUATEMALA 2005 – 2009

By

John J. Lyons

A DISSERTATION

Submitted in partial fulfillment of the requirements for the degree of

DOCTOR OF PHILOSOPHY

(Geophysics)

MICHIGAN TECHNOLOGICAL UNIVERSITY

2011

This dissertation, "Dynamics and Kinematics of Eruptive Activity at Fuego Volcano, Guatemala 2005 – 2009," is hereby approved in partial fulfillment of the requirements for the Degree of DOCTOR OF PHILOSOPHY IN GEOPHYSICS.

Department of Geological and Mining Engineering and Sciences

Signatures:

Dissertation Advisor _____
Dr. Gregory P. Waite

Dissertation Co-Advisor _____
Dr. William I. Rose

Department Chair _____
Dr. Wayne D. Pennington

Date _____

Table of Contents

List of Figures

List of Tables

Preface

Volcanoes are the surficial expressions of long-lived pathways that link the depths of the lithosphere with the hydrosphere and atmosphere. The primary function of these pathways is the release of gas, heat and molten rock generated by the rise of hot material from the core-mantle boundary in the form of mantle plumes or from the large-scale mantle convection that continually produces oceanic crust at ridge systems and recycles it in subduction zones. Subduction zones are the site of the vast majority of subaerial volcanic vents worldwide and provide excellent natural laboratories for studying the multitude of processes that arise from the migration and release of volcanic products. Volcanoes release far more gas than what can be dissolved in the erupted magmas, and this excess degassing is a clear indicator that relatively small volcanic vents are the escape route for gases derived from large intrusive magma bodies emplaced at all levels of the crust [*Andres et al.*, 1993, *Rodríguez et al.*, 2004, *Rose et al.*, 1982, *Shinohara*, 2008]. Volcanoes in subduction zones are generally volatile rich due to the large amounts of water and other volatiles that are trapped in mineral phases during hydrothermal alteration of the oceanic crust.

The three most abundant volatile species in subduction zone magmas are H_2O, CO_2 and SO_2, which make up ~95 wt% of total magmatic volatiles [*Shinohara*, 2008, *Wallace*, 2005]. Water accounts for 90 – 95 mol% of total volatiles while CO_2 and SO_2 typically account for 1 – 3 mol% of total volatiles each [*Shinohara*, 2008]. Estimates of the flux of these volatiles through subduction zones indicates that there is an approximate balance of H_2O input into the mantle and that returned to the crust and atmosphere by magmatism [*Wallace*, 2005]. This is not the case for C and S. Only ~50% of the C

subducted into the mantle is recycled back into the atmosphere through degassing, while estimates suggest that only 14 – 25% of S is returned to the surface [*Wallace*, 2005].

Excess degassing results in relatively open vent configurations at many subduction zone volcanoes, often with relatively low amounts of magma erupted. In basaltic systems, the mechanism for sustaining an open degassing pathway is most likely conduit convection in which hot, gassy magma rises buoyantly until reaching the exsolution pressure while cooler, denser, degassed magma simultaneous descends to either crystallize in a deep magma body or be refluxed with gas [*Shinohara*, 2008]. Water and CO_2 behave very differently in magma, and variations in eruptive styles have been attributed to the dominance of one gas over the other. Carbon dioxide exsolves at high pressures and may accumulate at the tops of deep magma storage reservoirs or in other geometric traps along the conduit. Laboratory experiments have shown that gas will accumulate in a foam layer at the roof of a magma chamber, and that this foam eventually becomes unstable [*Jaupart and Vergniolle*, 1988, *Jaupart and Vergniolle*, 1989, *Vergniolle and Jaupart*, 1986, *Vergniolle and Jaupart*, 1990]. The unstable foam collapses into gas slugs that rise buoyantly, deftly navigating changes in conduit geometry and driving strombolian eruptions or generating fire fountains. Spectroscopic measurements of gases released during fire fountaining and strombolian explosions show increased levels of CO_2 versus measurements of passive degassing, suggesting that they are the result of storage of CO_2-rich gas at depth [*Allard et al.*, 2005, *Burton et al.*, 2007].

The exsolution of water from a volatile-saturated magma can have profound effects on eruptive style because of dramatic rheological changes that occur in magma

due to water loss. The most important effect of water loss on basaltic magmas is undercooling [*Sparks and Pinkerton*, 1978]. Decompression-driven water loss causes ~20° C of undercooling per 1 wt% H_2O lost, and arc basalts often contain 3 – 5 wt% H_2O [*Boyd*, 1961, *Roggensack*, 2001, *Sisson and Layne*, 1993]. Undercooling promotes nucleation and crystal growth rates of anhydrous phases, reaching maximum effect at 50 – 100° C [*Kirkpatrick*, 1976, 1977]. A spectacular example of this process was recorded in detail at Mauna Loa during the 1984 north-east rift eruption. *Lipman et al.* [1985] measured an increase in microphenocrysts in erupted lavas from 0.5 to 30% over 20 days without any change in eruptive temperature or bulk composition. Dissolved water also lowers the liquidus temperature and changes the order in which mineral phases occur, so the loss of water also promotes crystal nucleation and growth by rapidly raising the liquidus [*Sparks and Pinkerton*, 1978]. This process of degassing crystallization will lead to basalts with high yield strengths and high apparent viscosities, typically within the upper several hundred meters of the conduit, and can generate explosive eruptions [*Sparks and Pinkerton*, 1978, *Sparks*, 2003].

Ground- and satellite-based remote sensing of the gases, heat and elastic energy associated with the migration and eruption of gases and magma allow us to track and characterize eruptions from a safe distance. Regular satellite over-flights and improved sensor detection levels and spatial resolution allow for the study of eruptive activity over long time periods, which can be particularly useful for comparing with ground-based observations [*Carn et al.*, 2008, *Wright and Flynn*, 2004, *Wright et al.*, 2004]. The proliferation in use of seismic sensors at active volcanoes has lead to a greater

understanding of how magma moves within volcanic conduits and the types of signals that are most often related to different eruptive behavior [*Chouet*, 1996a, *McNutt*, 2005]. This has lead to the ability to forecast changes in eruptive activity and the widespread adoption of seismicity as a fundamental volcano monitoring tool [*Chouet*, 1996b]. The more recent availability of broadband seismometers has greatly increased the timescale over which volcanic events can be studied and a growing number of studies addressing very-long-period (VLP) signals is rapidly advancing our understanding of conduit dynamics [*Aster et al.*, 2008, *Chouet et al.*, 2003, *Chouet et al.*, 2010, *Dawson et al.*, 2011, *Waite et al.*, 2008]. Broadband infrasound microphones are increasingly being deployed alongside broadband seismometers to record the low frequency energy that volcanoes emit to the atmosphere [*Fee et al.*, 2010, *Garcés et al.*, 1998, *Johnson and Lees*, 2000, *Johnson et al.*, 2004, *Matoza et al.*, 2007]. Infrasound records provide a clear complement to seismic data, allowing for rapid identification of explosive events and potentially providing information on changing eruptive styles based on the seismic and acoustic energy partitioning of explosive eruptions [*Garcés et al.*, 1998, *Johnson and Aster*, 2005, *Mori et al.*, 1989].

This body of work focuses on the kinematics and dynamics of eruptions at Fuego volcano, Guatemala over a four year period of observations based on the theories and methods outlined above. The first chapter focuses primarily on the utility of careful, low-tech observations of eruptive activity. I performed these observations while a Peace Corps volunteer stationed at in the small town of Panimaché, site of the INSIVUMEH Fuego observatory. The methods detailed in Chapter 1 were taught to the local observers

and are still in use today as a means of tracking eruptive activity. In 2007, I borrowed a seismic and infrasound station from a visiting scientist and was able to record the first long-duration seismic and infrasound record of the eruptive activity at Fuego. Upon returning to Michigan Tech, I compared my observations with thermal and gas remote sensing data and seismicity, confirming that the methods of simple observations were robust. Chapter 1 also provides an interpretation of a loose cycle of activity that I observed while living at Fuego. This interpretation considers similar cycles recorded at other volcanic systems as well as laboratory models and proposes two possible physical models for the generation of the variability I observed.

The second chapter focuses on the kinematics of explosive events recorded on seismic and acoustic sensors during 2007 – 2009. The primary means of comparing the explosions is to calculate the energy partitioning between the seismic and acoustic records of each event. The two 2008 datasets do not show a clear difference in energy partitioning despite the very different style in explosions that they captured. However, a clear shift in energy partitioning occurred in 2009 and I attribute this to the generation of greater overpressure in the magma, possibly due to either gas slugs ascending from deeper in the conduit or by pressurization of a plug of magma at the top of the conduit. While other authors have attributed short-term variations in energy partitioning to a variety of causes (e.g., changing source depth, changing magma properties, multiple vents), I found it difficult to unequivocally constrain the cause of rapidly changing energy ratios. Instead, the utility of calculating and comparing energy ratios seems to lie with comparing ratios over months or years to look for long-term shifts in behavior.

The third chapter focuses on the strongest explosions recorded in 2009 and the VLP seismicity that is associated with these events. I performed a full waveform inversion of a representative event in the 10 – 30 s band in order to determine the best fit point source of the VLP, which is located 300 m west and 300 m beneath the summit crater. The source time function of the best fit source for a six moment component solution is dominated by the dipole components, suggesting a volumetric source. Forward modeling was performed at this location to constrain the source geometry and it shows that a crack dipping 35° to the southwest combined with a nearly vertical crack is the most likely geometry. We interpret this as a shallow sill, likely controlled by a resistant layer (lava flow) at depth, being fed by a near vertical dike. The pressure history of the sill records an inflation-deflation-reinflation cycle with a maximum volume change of 1570 m^3. Similar pressure cycles have been seen in VLP seismicity at other volcanoes and attributed to the ascent and bursting of large gas slugs [*Chouet et al.*, 2003] or to the brittle failure of a pressurized plug of magma at the top of the conduit [*Chouet et al.*, 2005]. Apparent tilt data, SO_2 emissions [*Nadeau et al.*, 2011] and infrasound records all suggest that brittle failure of a magma plug is the more likely model for generation of the Fuego VLPs. I then consider the magma chemistry and volatile content and determine that the development of a brittle magma with a high yield strength is physically plausible at Fuego. The location of the VLP source west of the summit crater suggests that the deep feeder dike may have migrated from directly beneath the summit to a more westward location, and this has potential hazard implications for those communities, like Panimaché, that surround the volcano.

The fourth chapter investigates the apparent tilt signal derived from the horizontal channels of the seismic data. These are the first deformation signals that I am aware of generated in association with explosions at Fuego, and I describe the waveforms in detail. The tilt waveforms are compared with the broadband and VLP seismic data, and I describe the spectral content of precursory seismic events that appear to affect the tilt signal. The tilt signal is modeled using the same 3-D finite difference method used in the VLP study, which includes the actual topography of the volcano. Topography has been shown to have a strong effect on broadband seismic waveforms [*Lokmer and Bean*, 2010, *Neuberg and Pointer*, 2000], and particle motion plots of the apparent tilt at Fuego suggest strong topographic effects on longer-period tilt signals as well. The source geometry is modeled as a crack, a pipe and an isotropic source and the best fit results are described. Gas emission data recorded during the same period as the seismic data show steadily decreasing emissions for minutes prior to explosions [*Nadeau et al.*, 2011] and I interpret this with the tilt data to suggest that the entire upper cone deforms as a result of the pressurization of the conduit prior to explosions.

Together, these chapters consider the kinematics and dynamics of open vent eruptive activity at Fuego volcano from 2005 – 2009. The goal of this work was a greater understanding of how Fuego works and I think that positive strides have been taken. I chose broadband seismic and infrasound data as my preferred method to study Fuego's eruptions, and this has allowed me to investigate explosions over a wide range of timescales. A wide view has allowed for a more holistic consideration of Fuego's explosions and a more accurate interpretation of what the data are telling us. I believe

that this work substantially adds to the body of scientific knowledge about Fuego's eruptions and can potentially be extended to investigations at other arc volcanoes.

Acknowledgements

Many people and organizations made this work possible and I am extremely grateful to all of you. I was fully supported financially through the National Science Foundation PIRE 0530109 and with instrument support by IRIS PASSCAL.

My time in the Peace Corps was undoubtedly the single most important event that shaped this work. It was not always easy being in the vanguard of the nascent PCMI Program in Natural Hazards, but it has paid huge dividends. Flavio Linares and Peace Corps Guatemala were extremely welcoming and supportive of my work in Guatemala and their curiosity and passion gave me the freedom to blend a potent concoction of development work with scientific inquiry and exploration. My time living with Fuego changed me and how I thought about volcanoes and crystallized within me a desire to learn more about them. The two years living in the village of Panimaché was tough at times but the people were always curious about the gringo rubio and we enjoyed each others' company. Amilcar Calderas and Edgar Antonio Barrios open their lives and the Fuego observatory to me and I will always be indebted to them and their families for their kindness, support and, most of all, profound friendship. I received excellent support from everyone at the Instituto Nacional de Sismología, Vulcanología, Meteorología e Hidrología (INSIVUMEH) in Guatemala, but particularly Gustavo Chigna. Gustavo was like a Guatemalan godfather to me, always looking out for me from a distance and filled with sage advice.

The GMES department at Michigan Tech has been an outstanding place to work and study. It is refreshing and comforting to know that this type of institution exists,

where collaboration, community, exploration and scientific advancement are held up as guiding principles, and none more important than another.

Dr. Bill Rose has taught me volumes and I am deeply grateful to have had the opportunity to learn from him. Bill has unparalleled knowledge, curiosity and mischief and I sincerely hope that some of his magic has rubbed off on me. Bill's sense of creativity and open sharing of ideas has become a model for me and are a benchmark that all scientists should work toward, but not hope to attain. Bill and Nano have also shared to beauty of the Keweenaw with me, in particular the gem of Silver Island, which is like no other place on earth and which I will miss dearly.

Dr. Greg Waite probably didn't expect to have me as his first PhD student, but he has suffered me graciously. Greg has somehow gotten me up to speed on geophysics, seismology and computer programming, which deserves an award. Greg has had unshakable patience with me and has taught me volumes, often taking hours of his time to sit with me to debugging code or discussing eruption dynamics. Greg has the amazing capacity to keep track of an incredible quantity of details while still seeing the big picture, and I strive for this level of vision.

Dr. Jonathan Lees and Dr. Simon Carn have also been supportive committee members and I thank them for improving my work and serving as mentors and role models. Jonathan has been an excellent teacher and confidant, and always has encouraging words of advice tempered with experience.

My family and friends have been incredibly supportive and patient with me as I have slowly found my path, and I thank you all. This work could not have been completed without you.

Abstract

Volcanoes are the surficial expressions of complex pathways that vent magma and gasses generated deep in the Earth. Geophysical data record at least the partial history of magma and gas movement in the conduit and venting to the atmosphere. This work focuses on developing a more comprehensive understanding of explosive degassing at Fuego volcano, Guatemala through observations and analysis of geophysical data collected in 2005 – 2009. A pattern of eruptive activity was observed during 2005 – 2007 and quantified with seismic and infrasound, satellite thermal and gas measurements, and lava flow lengths. Eruptive styles are related to variable magma flux and accumulation of gas. Explosive degassing was recorded on broadband seismic and infrasound sensors in 2008 and 2009. Explosion energy partitioning between the ground and the atmosphere shows an increase in acoustic energy from 2008 to 2009, indicating a shift toward increased gas pressure in the conduit. Very-long-period (VLP) seismic signals are associated with the strongest explosions recorded in 2009 and waveform modeling in the 10 – 30 s band produces a best-fit source location 300 m west and 300 m below the summit crater. The calculated moment tensor indicates a volumetric source, which is modeled as a dike feeding a SW-dipping (35°) sill. The sill is the dominant component and its projection to the surface nearly intersects the summit crater. The deformation history of the sill is interpreted as: 1) an initial inflation due to pressurization, followed by 2) a rapid deflation as overpressure is explosively release, and finally 3) a reinflation as fresh magma flows into the sill and degasses. Tilt signals are derived from the horizontal components of the seismometer and show repetitive inflation

– deflation cycles with a 20 minute period coincident with strong explosions. These cycles represent the pressurization of the shallow conduit and explosive venting of overpressure that develops beneath a partially crystallized plug of magma. The energy released during the strong explosions has allowed for imaging of Fuego's shallow conduit, which appears to have migrated west of the summit crater. In summary, Fuego is becoming more gas charged and its summit centered vent is shifting to the west - serious hazard consequences are likely.

CHAPTER 1

Patterns in Open vent, Strombolian Behavior at Fuego Volcano, Guatemala, 2005-2007

The material contained in this chapter was previously published:

Lyons, J., G. Waite, W. Rose, and G. Chigna (2010), Patterns in open vent, strombolian behavior at Fuego volcano, Guatemala, 2005–2007, *Bulletin of Volcanology*, *72*(1), 1-15

Abstract

Fuego volcano, Guatemala is a high (3800 m) composite volcano that erupts gas-rich, high-Al basalt, often explosively. It spends many years in an essentially open vent condition, but this activity has not been extensively observed or recorded until now. The volcano towers above a region with several tens of thousands of people, so that patterns in its activity might have hazard mitigation applications. We conducted two years of continuous observations at Fuego (2005-2007) during which time the activity consisted of minor explosions, persistent degassing, paroxysmal eruptions, and lava flows. Radiant heat output from MODIS correlates well with observed changes in eruptive behavior, particularly during abrupt changes from passive lava effusion to paroxysmal eruptions. A short-period seismometer and two low-frequency microphones installed during the final six months of the study period recorded persistent volcanic tremor (1-3 Hz) and a variety of explosive eruptions. The remarkable correlation between seismic tremor, thermal output, and daily observational data defines a pattern of repeating eruptive behavior: 1) passive lava effusion and subordinate strombolian explosions, followed by 2) paroxysmal eruptions that produced sustained eruptive columns, long, rapidly emplaced lava flows, and block and ash flows, and finally 3) periods of discrete degassing explosions with no lava effusion. This study demonstrates the utility of low-cost observations and ground-based and satellite-based remote sensing for identifying changes in volcanic activity in remote regions of underdeveloped countries.

1.1. Introduction

Fuego is a stratovolcano (3800 m) with a well-defined summit crater which marks the southernmost expression of the north-south trending Fuego-Acatenango volcanic complex. It is located in Central Guatemala, within the second of eight segments of the Central American volcanic front ([*Carr et al.*, 2002]; Figure 1.1). Fuego has had at least 60 historical subplinian eruptions and several longer periods (i.e., months to years) of low-level strombolian activity. The most recent intense, subplinian activity (VEI 4), which occurred in four main pulses during October 1974, produced ash fall, pyroclastic flows, lava flows, and lahars that displaced local populations and damaged agricultural production [*Nadeau et al.*, 2011]. Low-level strombolian activity persisted until 1979 [*Rose et al.*, 1978] and from 1980 to 1999 Fuego had irregularly spaced subplinian (VEI 1-2) events with periods of repose [*Martin and Rose*, 1981; *Smithsonian Institute*, 1999]. The most recent continuous low-level strombolian activity began with a VEI 2 eruption on May 21, 1999, [*Smithsonian Institute*, 1999] and continued to the time of this writing (November 2008). This current activity is characterized by frequent, short (hundreds of meters) lava flows, pyroclastic explosions, lahars, and paroxysmal, extended-duration (i.e., 24-48 hrs) eruptions that produce longer lava flows (hundreds to thousands of meters), pyroclastic flows, and sustained eruptive columns. This more-or-less continuous activity leads to small eruptions nearly every day and a condition we call “open vent”, indicating that the vertical conduit, which has been the main vent in nearly all historic activity at Fuego, does not get constricted or plugged.

Within the historic record, the current activity is analogous to a period of low-level strombolian activity following the October 1974 eruption and lasting until 1979. *Martin and Rose's* [1981] thorough review of the historic record revealed that periods of persistent low-level activity are not common at Fuego. Unfortunately observations in the 1974-79 period were not detailed enough to make closer comparisons with 1999-2008.

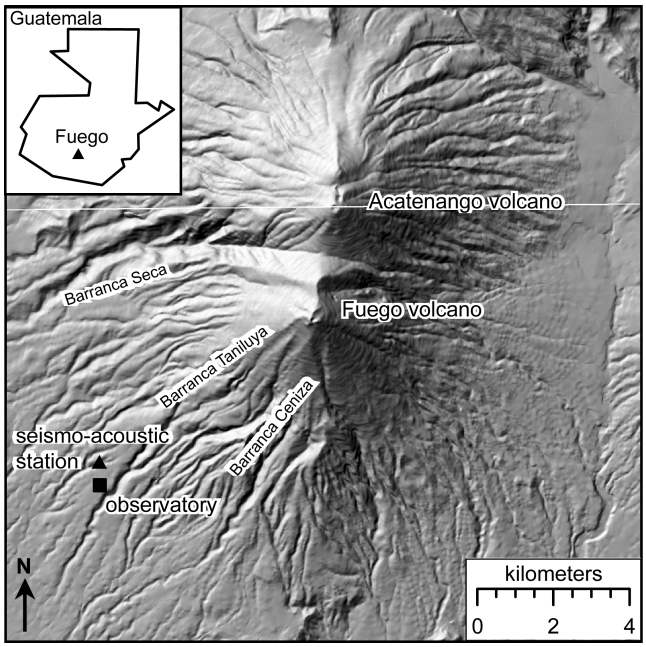

Figure 1.1. Digital elevation model of the Fuego-Acatenango volcanic complex created from 1954 aerial photos. The seismo-acoustic station deployed from January - July 2007 was located 7 km southwest of the active summit of Fuego. Barrancas control emplacement of lava flows, lahars, pyroclastic flows, and rock fall. Elevation difference between the summit of Fuego and the observatory is ~2700 m.

Fuego has produced primarily high-Al basalt (~51% SiO_2) since 1974. Melt inclusions (MI) in erupted olivine indicate that Fuego's magmas, like many other arc basalts and basaltic andesites, contain dissolved H_2O concentrations ranging from 2.1 to 6.1 wt% [*Roggensack*, 2001; *Sisson and Lanei,* 1993]. Studies of recently erupted tephras at Stromboli and Etna found ~50% SiO_2 and 2.8% H_2O (MI) in high-K basalts

[1981] and ~47% SiO_2 and 2.5 to 3.4 wt% H_2O (MI) in alkali basalts [*Roggensack*, 2001; *Sisson and Layne*, 1993], respectively. The high volatile content of Fuego's magmas probably influences eruptive behavior during periods when an open vent condition dominates. Persistent basaltic activity has been observed and documented at other volcanoes worldwide (e.g., Stromboli, Kilauea, Etna, Arenal), but not thoroughly at Fuego. This paper presents a summary of the continuous eruptive activity at Fuego volcano from August 2005 to June 2007. We describe the observed activity and its cyclic nature, and present new, complementary geophysical and satellite data that provide quantitative support for our observations.

1.2. Background

From August 2005 through June 2007 we made nearly continuous observations of Fuego's eruptive behavior from a local observatory manned by the Guatemalan governmental organization responsible for volcano monitoring, the Instituto Nacional de Sismologia, Vulcanología, Meterología e Hidrologia (INSIVUMEH). The observatory has a direct line of sight to the active summit of Fuego and is ~7.5 km southwest of the vent at 1090 m elevation (Figure 1.1). A single short-period seismometer and two low-frequency microphones were installed near the observatory and recorded from January 2007 to July 2007 to supplement daily observations (Figure 1.1).

On the basis of our observations we classify the eruptive behavior observed into three categories: 1) lava effusion and subordinate strombolian explosions, 2) paroxysmal, extended-duration eruptions, and 3) periods of discrete, often pyroclastic, explosions with

no concurrent lava effusion. The three types of activity were observed to occur in an ordered, repeating cycle of lava effusion and strombolian explosions, followed by a paroxysmal eruption, and finally explosions with no lava effusion. The complete cycle was observed five times during the two-year observation period and two complete cycles were sampled during 2007 with the seismo-acoustic station.

1.3. Descriptions of Observed Eruptive Behavior

1.3.1. Passive Lava Effusion and Subordinate Strombolian Explosions

Lava flowed from the summit crater into one or more of the incised canyons distributed around the southern half of the volcano for more than half of the period of 2005-2007 (Figures. 1.1, 1.2). Long periods (days to weeks) of low output effusion alternated with short periods (hours to days) of high output effusion, which occurred only during the paroxysmal eruptions described below. Typical lava flow dimensions during the low-rate effusive periods are 50-400 m long by 20-50 m wide and 2-4 m thick. These estimates were made on the basis of visual observations and field measurements of older accessible flows. The active flows were inaccessible due to the short lengths of the flows, steep slope and instability of the upper edifice, and the hazard from rock falls. Aerial observations of the summit region of Fuego show that some proximal lava flows have a pahoehoe texture, whereas an accessible portion of a particularly long flow (~4000 m) from 2003 in the Taniluya canyon shows that distal lava flows are exclusively 'a'a. This suggests that Fuego lava flows convert to 'a'a during flow down steep barrancas. At night the lava flows are incandescent and clearly visible from the observatory. The

majority of a flow would appear as dull orange ribbons and patches of incandescent lava within a black matrix of chilled lava (Figure 1.3).

When effusive activity began, lava flows originating from Fuego's summit crater were coherent for several tens of meters down slope and lengthened to as much as several hundreds of meters within a period of hours to days. It was most common for a lava flow to grow for a period of several days or weeks before reaching a steady state, after which the front neither advanced nor retreated significantly for periods of weeks to months. Observations and infrared images suggest that the nearly constant flow lengths were preserved through a balance of magma flux into the flow and lava calving from the sides and nearly fixed front of the flow (Figure 1.3).

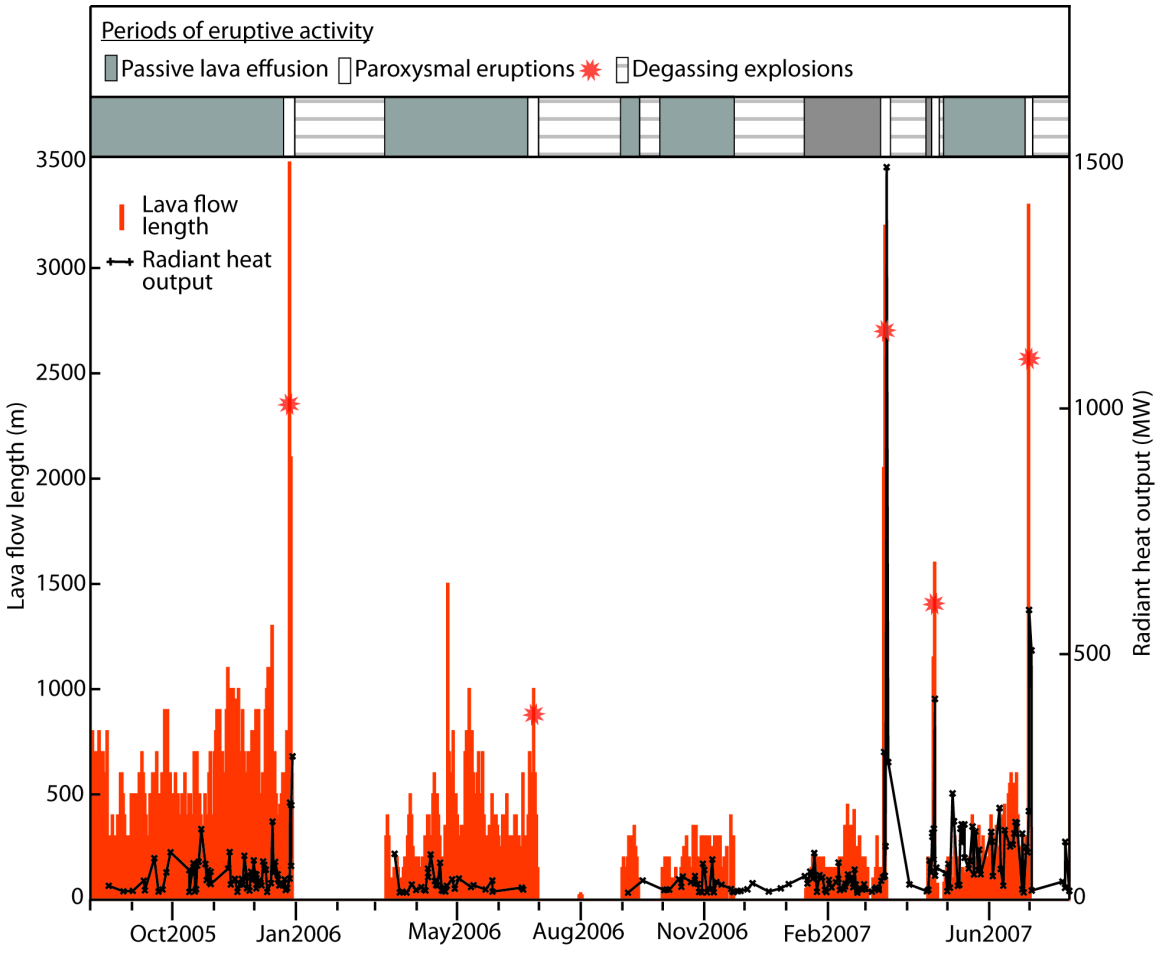

Figure 1.2. Observed daily lava flow lengths of all active lava flows (red) and total radiant heat output in MW (black) calculated from MODVOLC acquisitions of nighttime MODIS data [*Métrich et al.*, 2001]. The three distinct periods of activity identified by observations are also plotted (bar, above). Note the repeating pattern, 1) passive effusion, 2) paroxysmal eruption, 3) degassing explosions. The first period of passive effusion was ongoing at the start of this study, and the ultimate period of degassing explosions continued after the end of this study.

When output rate was relatively low, lava flow lengths changed slowly; however, during the paroxysmal eruptions (discussed below) the lava flows grew to ≥500 m in less than 24 hours. The long, rapidly emplaced flows were short-lived, suggesting that effusive intensity, and thus magma flux, is sometimes highly variable at Fuego over short

timescales, similar to activity at other basaltic systems such as Kilauea [*Métrich et al.*, 2004], Etna [*Wright et al.*, 2004], and Stromboli [*Parfitt and Wilson*, 1994].

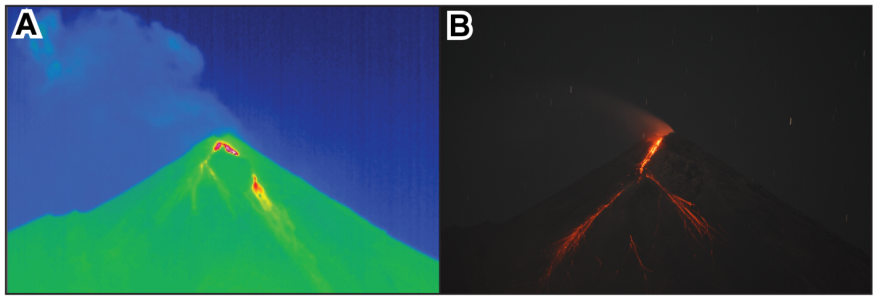

Figure 1.3. Thermal IR imagery (14 January 2007) and photograph (26 February 2007) taken from the observatory of short (~100 m and 300 m, respectively) lava flows emanating from the summit crater of Fuego. IR image from an Infratec Variocam camera operating in the wavelength range 8 - 13.5 μm with an image resolution of 320 x 240 pixels. Note that a portion of the lava flow in the thermal image is obscured by a large bulge of old lava that sits high on the SW flank of Fuego. Both images illustrate how passive lava flows at Fuego maintain short lengths over weeks to months by shedding blocks of lava from the flow front and sides.

1.3.1.1. Minor strombolian explosions

Fuego produced many hundreds of explosions during lava effusion in a style best classified as *strombolian* [*Lautze et al.*, 2004]. The explosion clouds rose 50-500 m above the summit and varied widely in ash content. The explosions were often silent when observed from 7-10 km or produced a weak to moderate popping noise infrequently accompanied by a weak shock wave that would rattle windows and metal roofs. When observed at night, the explosions sprayed incandescent magma up to 100 m above the crater and provoked small incandescent rock falls around the summit. The frequency of explosions varied from none to several tens per hour; often explosions came in series,

with the strongest explosion first, followed tens of seconds later by one or more weaker explosions.

1.3.1.2. Degassing during lava effusion

Audible degassing from Fuego, observed 7-10 km from the vent, occurred predominately during periods of lava effusion and was manifest as two distinct noises, best described as 'chugs' and 'jetting'. The chugging sounded very similar to the noise of a steam locomotive, with individual chugs occurring once every 1-4 seconds. The duration of the chugging varied from several seconds to tens of minutes of continuous chugging and chugging intensity varied from barely discernible to audible over almost all anthropogenic noise. Intensity would sometimes vary within individual sets of chugs, typically with faint chugging building to stronger chugs. When observed at night, chugging or jetting was often associated with minor incandescent ejecta and preceded increased lava flow activity (incandescence in the flow front and sides and more abundant rock fall) by a few minutes. Chugging has been documented at many volcanoes that have similar activity and magmatic and volatile contents as Fuego, including Langila [*Calvari et al.*, 2005], Semeru [*Blackburn et al.*, 1976], Arenal [*Mori et al.*, 1989], Karymsky [*Schlindwein et al.*, 1995], and Sangay [*Benoit and McNutt*, 1997]. *Benoit and McNutt* [1997] attributed chugging to rhythmic degassing of a gas-charged magma. *Johnson and Lees* [*Johnson*, 2007; *Lees and Ruiz*, 2008] and *Lees and Ruiz* [1997] observed a linear correlation between explosion pressure and interexplosion time; they favor a model where pressure accumulates within a clogged conduit and is episodically

vented. At Fuego, the chugging seems to represent more energetic degassing or a specific vent condition, but is not modeled in detail here.

1.3.2. Paroxysmal Eruptions

Five paroxysmal, long-duration eruptions occurred during the observation period (Figure 1.2). The eruptions began with intermittent periods of weak gas chugging that built into continuous chugging and finally louder explosions every 0.5-3 seconds that persisted for 24-48 hours. The continuous explosions fueled sustained eruptive plumes of gas and fine ash, which developed quickly after the onset of each eruption. The plumes rose 1-4 km above the summit crater and stretched 15-25 km in the downwind direction (Figure 1.4). A period of lava effusion always preceded the paroxysmal eruptions, and continued until the end of each eruption.

Similar eruptions in the current period of activity have been classified as strombolian [2000]. However, the eruptions observed during 2005-2007 contained elements of both classic strombolian- and hawaiian-type eruptions and may be better described as transitional eruptions following the work of [2008] and [Smithsonian Institution, 1999]. The 1973 eruption of Heimaey volcano also displayed this type of eruptive activity with explosions 0.5-2 seconds apart that produced a sustained eruption cloud reaching 6-10 km and continuous lava effusion [*Parfitt and Wilson*, 1995].

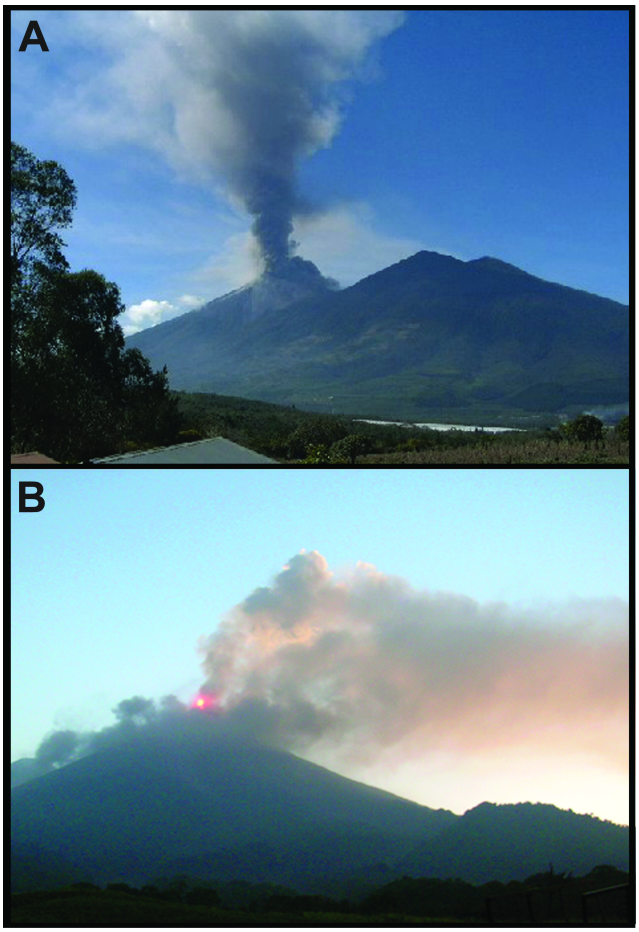

Figure 1.4. Photographs from paroxysmal eruptions of Fuego during the study period. A: 27 December 2005 (view is to the west from the town of Alotenango ~10 km from summit), notice small pyroclastic flow moving north from the base of the eruptive column. B: 16 March 2007 (view is to the northeast from observatory), notice overriding ash cloud from a small block and ash flow descending down Barranca Seca (left of eruptive column).

Paroxysmal eruptions were spectacular at night, spraying clots and curtains of incandescent magma 50-300 m above the crater (Figure 1.5). During the most energetic periods of activity, nearly overlapping explosions produced sustained fountains of incandescent ejecta. The explosions were clearly heard 15 km from the summit, and the strongest explosions produced shock waves that rattled windows and metal roofs 8 km

from the summit. Increased lava effusion during paroxysmal eruptions (Figure 1.2) frequently produced simultaneous flows in three to five of the canyons on the southern half of the cone. Lava effusion peaked during the most energetic explosive activity and terminated abruptly at the end of every paroxysm (Figure 1.2). During four of the five paroxysmal eruptions observed, a second vent on the southwestern flank ~100 m below the summit vent (Figure 1.5) produced a lava flow and explosions every 2-5 seconds. Explosions and lava effusion always continued from the main crater when the flank vent was active but the timing of explosions at the two vents did not coincide.

Fuego's paroxysmal eruptions are capable of producing pyroclastic flows that could reach several villages within 5-15 km of the vent and are the most significant hazard at the current level of activity. All of the eruptions observed during 2005-2007 produced block and ash flows that developed from the downslope fronts of active lava flows. Nighttime observations during the eruption of 26-27 June 2006 showed that small pyroclastic flows would begin near or at the front of active lava flows several hundred meters below the summit. A small area near the front of the flow grew dark at the onset of each collapse, with the ash cloud quickly engulfing the entire summit. Careful observations showed that lava flow growth was aided by agglutination of still-plastic pyroclasts falling onto the upper reaches of the lava flow [*Parfitt*, 2004]. Loading of the near-vent portion of the lava flows through this process may have triggered a given lava flow to collapse and form pyroclastic flows [*Blackburn et al.*, 1976].

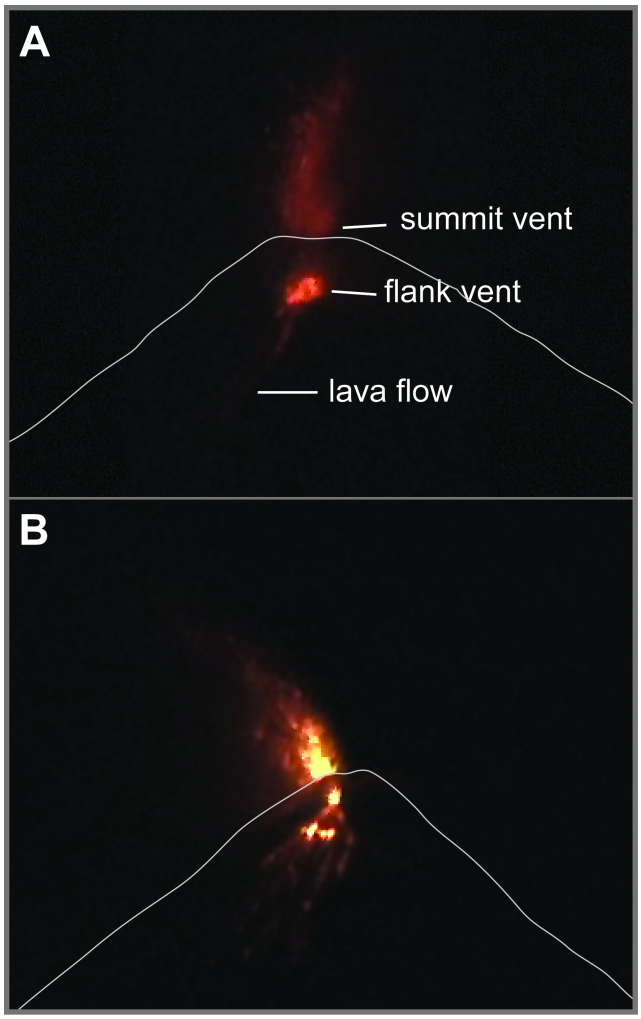

Figure 1.5. Nighttime images of paroxysmal eruptions at Fuego taken from a video camera at the INSIVUMEH observatory 7.5 km from the summit crater (Figure 1.1). Grey line outlines the profile of the upper cone. A: 15 March 2007 eruption with incandescent ejecta reaching ~250 m above the summit crater. The primary summit crater vent and the flank vent were simultaneously active during the eruption. The flank vent was located ~100 m below the summit in the direction of Barranca Taniluya. B: 1 July 2007 eruption with both vents active. Bubble bursts and a lava flow emanated from the flank vent and deposited material in Barranca Taniluya.

Velocities of pyroclastic flows that accompanied the 26-27 June 2006 paroxysm ranged from 25 km/hr to as high as 150 km/hr. During peak activity, a pyroclastic flow generated at the front of an active lava flow traveled 5 km down the Barranca Ceniza in

two minutes. Near the end of the paroxysm, a small block and ash flow began as a lava flow front collapsed several hundred meters below the summit. The thin, narrow pyroclastic flow descended several hundred meters, came to rest, then was remobilized tens of seconds later and descended several hundred meters more. This pattern repeated several times as the flow slowly descended over 4 km in 9 minutes.

Although paroxysmal eruptions always followed periods of lava effusion and minor strombolian explosions, neither our group nor the local volcano observers from INSIVUMEH were able to unequivocally forecast their onsets. Increased audible chugging always preceded these eruptions, but increases in the intensity and duration of chugging often occurred without a subsequent eruption. Likewise, increased incandescence (seen at night) from the summit crater always preceded an eruption, but was commonly followed only by minor increases in lava flow length.

The eruptions began very rapidly with the onset of sustained explosions that ejected pyroclasts from the summit crater. The end of the eruptions was nearly as abrupt, often starting with a decline in the intensity and frequency of explosions and a decrease in the amount of ash in the plume and then a decrease in the length of lava flows and occurrence of pyroclastic flows. When activity began to decrease, it typically took several hours to reach complete quiescence. Following an eruption, Fuego was typically quiet for several days, producing only a passive degassing plume prior to the onset of the degassing explosions.

1.3.3. Degassing Explosions

The explosions that occurred during periods of effusion were distinct from those produced when no lava flows were active in terms of audible volume and frequency, ash content, size of explosion cloud, frequency of occurrence. Explosions in the absence of lava effusion, which we term degassing explosions, were typically louder, more ash-rich, ejected more ballistics, and occurred less frequently than explosions during lava effusion. Discrete degassing explosions began within days of the end of a paroxysmal eruption, (Figure 1.6) and lasted for about a week. Dark grey explosion clouds exited the summit crater at a rate of 1-5 per hour and quickly rose several hundred to 2000 m above the summit. The explosions were not audible 7.5 km from the summit; the audible acoustic energy may have been absorbed or muffled by debris from the previous paroxysmal eruption overlying the fragmentation zone as suggested by [*Head and Wilson*, 1989] and [*Wilson and Head*, 1981].

Figure 1.6. Photograph of a large degassing explosion on 21 March 2007 at 0728 hours local time, five days after the end of the 15-16 March paroxysmal eruption and quiescence of lava effusion. View is to the northeast from the observatory. Column is ~2000 m height above the summit. A weak audible report accompanied this explosion. Similar explosions during this period caused short periods (3-5 min) of ashfall up to 10 km from Fuego.

The short period of silent, ash-rich explosions evolved to less ashy, but much noisier blasts. Grey to bluish-white eruptive clouds from these events rose hundreds of meters above the summit crater and, ~20 seconds after the visible onset of the explosion, a loud report was heard at 7.5 km from the summit. The loudest explosions were heard 21 km from the summit, while the accompanying shock wave rattled windows and shook metal roofs up to 12 km from the summit. As the transition from degassing explosions to lava effusion began, explosions would become more frequent and increasingly ash-rich. In some cases, short periods of weak gas chugging would follow explosions. At night, an incandescent pulsing or flashing within the crater accompanied the chugging and could be seen projected in the degassing plume above the summit. As magma neared the surface, the explosions (observed at night) threw incandescent pyroclasts above the summit and generated minor rockfalls. Renewed effusion began with increased

incandescent rockfall generated at some point on the rim of the summit crater, probably the low point where the crater was no longer able to contain the new lava. Within days of the appearance of a sustained lava flow, the ash content of the explosions decreased significantly and the explosions changed from muffled blasts to shorter, sharper reports signaling a return to the passive lava effusion stage.

1.4. Data Overview

1.4.1. Lava Flow Length and Mean Daily Lava Output Rate

The eruption characterization described was derived from visual observations. Daily lava flow lengths are estimated by summing the total lengths of all active lava flows visible to the authors with those reported by INSIVUMEH observers from different sectors of the volcano. Lava flow lengths were estimated from a scaled profile of the volcano drawn on an observatory window. Repeated measurement of active lava flow lengths by JJL and the two volcano observers routinely resulted in agreement of ±50 m. While somewhat qualitative, they are the only data consistently available for the whole of the observations reported here.

A fixed cross-sectional area of 60 m^2 was used for all lava flow volume calculations based on widths of flows measured in aerial photos and observed in the field, and thicknesses of flows observed in the field. The daily lava flow length multiplied by the cross-sectional area is then divided by a complete day to produce a mean daily lava output rate [*Murata et al.*, 1966]. This approximation most likely over-estimates the cross-sectional area of shorter flows by up to a factor of 3 and underestimates the cross-

section of longer flows, especially during paroxysmal eruptions, up to a factor of 3. We assume that the entire volume of the lava flow from the previous day is destroyed by calving of that flow, thereby allowing us to use the whole length from any given day rather than the difference between lengths observed on that day and the previous day. Basaltic flows emplaced on steep slopes (>30°) at Stromboli have been shown to lose up to 70% of their erupted volume due to flow front collapse [*Mori et al.*, 1989]. Our assumption of total loss by collapse probably overestimates the amount of calving by at least 30%.

Calving was the primary indication of the location of active flow fronts. We assume that calving is a direct result of magma flux into the head of the flow. If a flow was not observed to be shedding blocks, we assumed that input had stopped, and that the output rate was zero. A more detailed set of observations and a higher sampling rate are necessary to reduce the assumptions we make here and better constrain the calving rate, which is an important factor to include in output or effusion rate calculations for volcanoes that emplace flows on steep slopes.

1.4.2. Thermal Output

Thermal alerts for volcanoes worldwide are obtained from NASA's moderate resolution imaging spectroradiometer (MODIS) through the automated volcanic thermal alert algorithm MODVOLC [*Harris et al.*, 2007]. Low-spatial-resolution, high-temporal-resolution thermal data from MODIS has been used successfully to remotely monitor new and ongoing volcanic eruptions worldwide [*Lodato et al.*, 2007]. On average, one satellite image is acquired every 12 hours. The MODVOLC algorithm uses differences

in short-wave radiation (4 μm) emitted by hot volcanic deposits (bands 21 and 22), and long-wave radiation (11 μm) from background surfaces (band 32) to determine anomalous hot spots at georeferenced volcanoes worldwide [*Wright et al.*, 2002; *Wright et al.*, 2004]. The resultant hot spots are posted to a website (http://modis.higp.hawaii.edu/) in near-real-time. Radiative heat flux was determined from spectral radiance via a simple empirical relationship described in detail in *Kaufman et al.* [*Flynn et al.*, 2002; *Patrick et al.*, 2005; *Wright et al.*, 2005] and *Wright and Flynn* [*Wright et al.*, 2002]. Our heat flux calculations use only nighttime data in order to avoid a potential source of error from solar reflections and solar heating [1998].

The MODVOLC algorithm is tuned to rapidly detect volcanic hotspots worldwide and there are limitations for using the data to estimate heat output. Short, narrow lava flows produced by Fuego during parts of the study may fall below the detection limit of MODVOLC and not trigger an acquisition. Furthermore, visual images are not co-collected with each hotspot acquisition so it is it difficult to assess the effects of atmospheric clouds and eruption plumes on the spectral data. No other ground-based or satellite-based thermal data are available for Fuego and no error estimates for MODVOLC data are published so we can not quantify error in the heat loss calculation. However, *Wright and Flynn* [2004] show that the heat flux determined from the MODVOLC data at Erta Ale are consistent with both short-term ground-based measurements and longer-term satellite data using different methods. It is important to note that we are using the radiative heat output as a relative, long-term metric of eruption

intensity to compare with our observational data, and to not attempt to model the flux directly.

1.4.3. Seismic and Acoustic Data

A seismo-acoustic station installed ~7 km southwest of the summit of Fuego during the last six months of the study period consisted of a Geospace GS-1 short-period vertical seismometer and two low-frequency microphones (Figure 1.1). Data were recorded nearly continuously from 16 January-7 July 2007 (172 days). Time and frequency-domain analysis of seismic records from the entire data set showed that volcanic tremor between 1 and 3 Hz was present during all three periods of eruptive behavior (Figure 1.7), similar to well-documented tremor at other volcanoes with persistent basaltic eruptions (e.g. Pavlof [*Wright and Flynn*, 2004]; Stromboli [2004]; Etna [*McNutt*, 1986]). Three periods of lava effusion and strombolian explosions, three paroxysmal eruptions, and two complete periods of degassing explosions occurred while the seismo-acoustic station was operating (Figure 1.8).

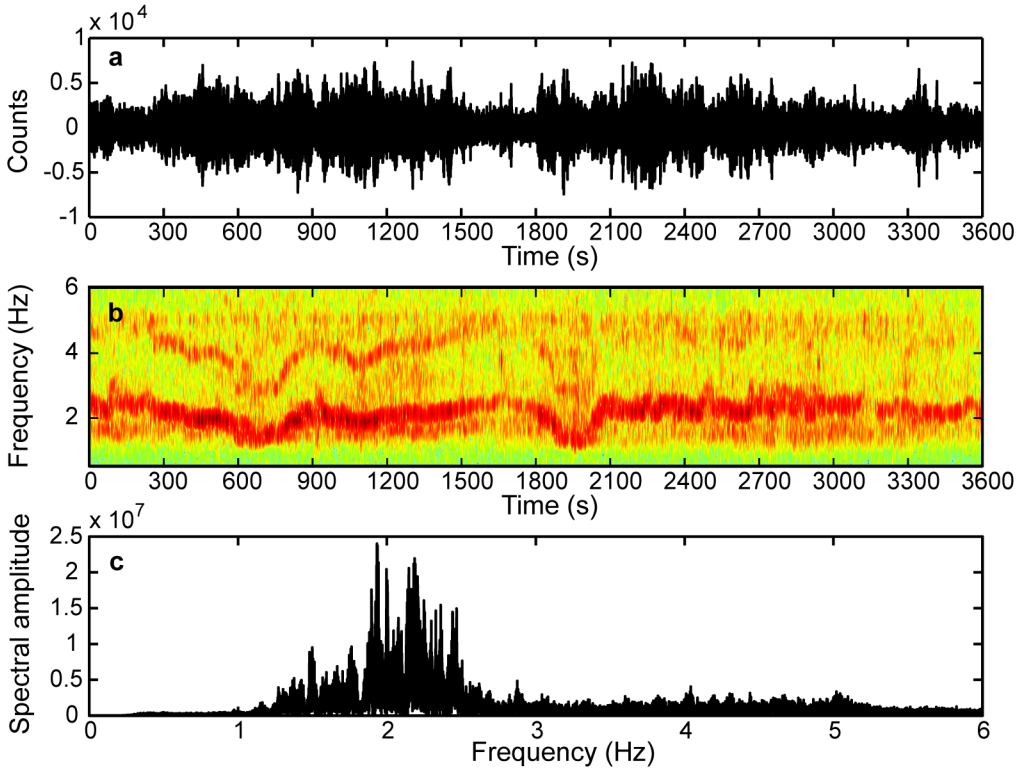

Figure 1.7. Waveform (a), spectrogram (b), and spectrum (c) of a representative hour of harmonic tremor from Fuego recorded 13 June 2007. The seismic data were filtered between 0.5 and 6 Hz, due the presence of an anthropogenic harmonic oscillator that produced signals in the 8-10 Hz range. Frequency content was determined by computing a fast Fourier transform (FFT) over the hour-long time series data in 500 sample (5 s) windows with a 250 sample (2.5 s) overlap between windows. The spectrogram (b) shows how the frequency glides over relatively short timescales, while the spectrograph (c) illustrates how harmonic tremor varied between 1 and 3 Hz during the study period.

1.5. Data Analysis

1.5.1. Lava Flow Lengths and Thermal Output (August 2005-July 2007)

Fuego effused visible lava flows from the summit crater for 461 (63.2%) out of the 730 days of the study period, while for 266 days (36.8%) no effusion was observed (Figure 1.1). Active flows shed blocks from the front and sides of the flow, which were visible as dust plumes during the day and incandescence at night. The average length of all lava flows active during periods of passive effusion and strombolian explosions (i.e.,

excluding paroxysmal eruptions) is 371 m. The average length of all the active lava flows during the paroxysmal eruptions is 1960 m, or 5.3 times greater than during passive effusion. The average duration of effusive periods, including the paroxysmal eruptions, was 38.8 days, while periods of no effusion averaged 30.0 days long.

The observed lava flow length and the total radiant heat output correlate well for the duration of the study (Figure 1.2). The radiant heat output dropped below the MODVOLC detection limit at nearly the same time as observed lava flow activity ceased and explosive activity changed after extended periods of effusion in 2005 and early 2006 (Figure 1.2). This suggests that the lava flows produced during this period were relatively thin and cooled quickly, which agrees with proximal flow characteristics in aerial photos and our observed estimate of lava flow dimensions. The MODVOLC heat output estimates correlate with the rapid increases in lava flow length for four of the five paroxysmal eruptions (Figure 1.2). The 20-21 June 2006, paroxysm was not detected by MODVOLC, but this eruption occurred during the rainy season in Guatemala, and the volcano was cloud-covered for much of the eruption. Similar to the observed lava flow lengths, radiant heat outputs increase rapidly at the onset of paroxysms and then decrease rapidly at their conclusions. Beginning late in 2006, spikes in MODVOLC data occurred during periods when no lava flow activity was observed (Figure 1.2). High radiant heat measurements during periods with no observed effusion, along with increasingly shorter periods of lava quiescence and more frequent paroxysmal eruptions in the second half of the study, may indicate that the free surface of the magma column remained closer to the surface during this period compared to the first half of the study.

1.5.2. Mean Daily Lava Output Rate (August 2005-July 2007)

On the basis of the lava flow length data and estimated cross-sectional area, we were able to make an estimate of the mean daily lava output rate (Figure 1.9). This nomenclature follows the work of *Harris et al.* [*Falsaperla et al.*, 1998] and is useful because it provides a metric of eruption intensity, assuming that calving completely destroys the lava flow each day.

The time-averaged bulk rock output rate during the entire study period is 0.18 m^3 s^{-1}; however, the rate varied by more than two orders of magnitude between the lowest and highest daily mean output rates, 0.021 m^3 s^{-1} and 2.43 m^3 s^{-1}, respectively. Our output values are similar to longer-term bulk rock discharge rates at the two other continuously active volcanoes in Guatemala. From 1954-2001 the time- averaged discharge rate at Santiaguito volcano was 0.38 ± 0.08 m^3 s^{-1}, while at Pacaya volcano the time-averaged discharge rate was 0.22 ± 0.02 m^3 s^{-1} from 1961-2001 [Durst et al. *in review*]. The 2002 -2003 effusive eruption of Stromboli volcano had many characteristics similar to Fuego's ongoing activity. The time-averaged discharge rate for that eruption was 0.32 m^3 s^{-1} with a measured variation of 0.1-0.7 m^3 s^{-1} [*Alparone et al.*, 2007].

Based on our output rate, the total volume of lava produced during this period is 11.3×10^6 m^3. This estimate does not include tephra deposits, which may be significant during the paroxysms, because most tephras were deposited on inaccessible portions of the cone. The most recent georeferenced aerial photographs from Fuego are available from 2001 and 2006. Using the photos and our knowledge of where most of the

deposition has occurred in recent years, we were able to delineate an area of maximum growth of the upper cone. We estimate a uniform thickness of new material of between 10 and 50 meters on the basis of measureable landforms, which gives a total volume increase of 9-48 x 10^6 m^3 over six years. Assuming a steady rate of growth, the volumetric growth of the upper cone during the study period would be 3-16 x 10^6 m^3, which is comparable to our volume estimate from the output rate.

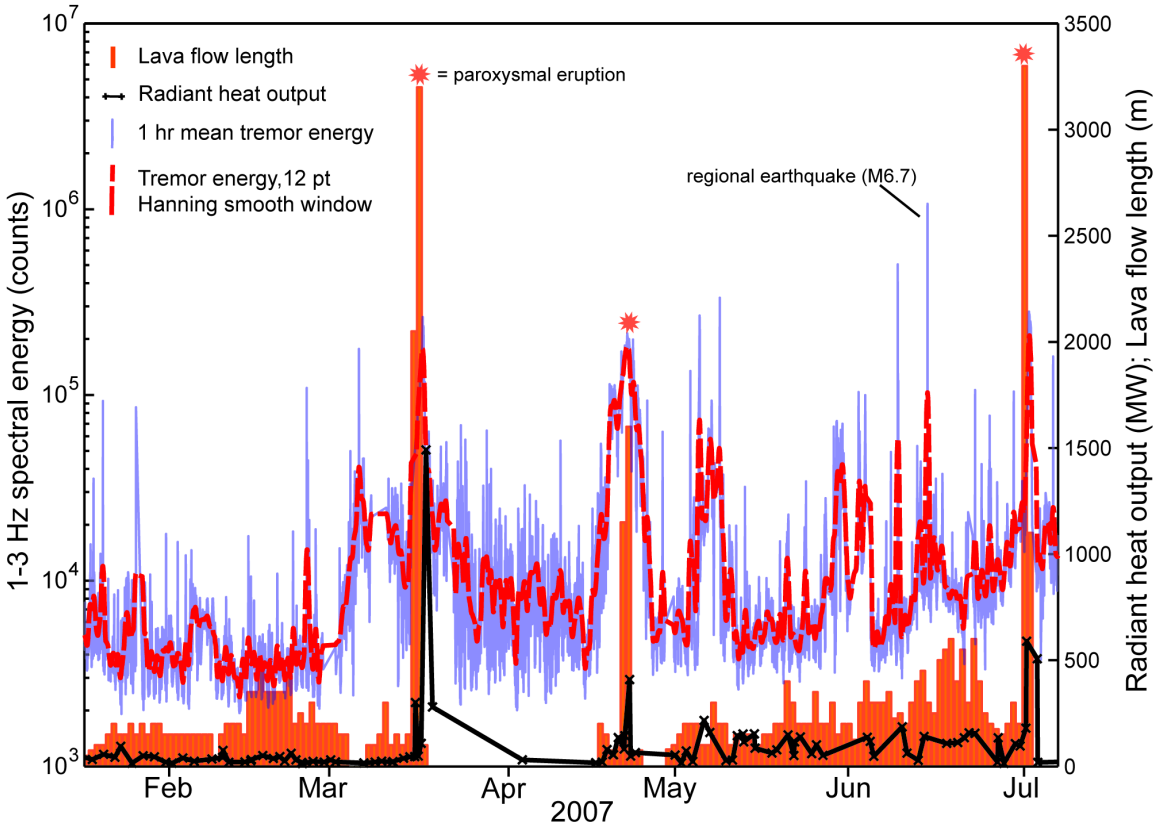

Figure 1.8. Lava flow lengths (orange bars), radiant heat output (black), and tremor energy (blue and red) from 16 January-7 July 2007. Vertical bars represent daily total active lava flow lengths (right axis label), as in Figure 1.2. Radiant heat output (black line with crosses; right axis label) determined from MODIS, as in Figure 1.2. Faint grey trend is the hourly mean seismic energy calculated only in the 1-3 Hz band (left axis label). A 12-point Hanning smoothing window was applied to the hour-long mean seismic energy data (dashed line). Paroxysmal eruptions on15-16 March, 20-21 April, and 1-2 July (asterisks) were recorded clearly in all three datasets.

1.5.3. Seismicity, Lava Flows, and Thermal Output, January 16-July 7, 2007

Installation of the seismo-acoustic station in 2007 provided another means to track volcanic activity quantitatively and improved the temporal resolution of monitoring at Fuego. We used spectral energy in the 1-3 Hz band to quantify tremor energy. The typical dominant tremor frequency was 2 Hz, but the wider band was chosen so we would capture all the energy during gliding episodes (Figure 1.7). One or more overtones of this fundamental frequency were occasionally observed. In order to examine the entire dataset, we computed hourly means of spectral energy in this band. Overall, tremor energy correlates well with both the observed lava flow lengths and the thermal output, except during degassing explosions (Figures 1.8, 1.10). The paroxysmal eruptions are recorded in the tremor energy, as peaks 10-50 times larger than the background tremor energy. These peaks coincide with spikes in thermal output and lava flow lengths. Peak tremor energy is similar for the three paroxysms, but the shapes of the tremor amplitude spikes vary (Figure 1.8).

During the 2000 Southeast Crater eruption of Mt. Etna, *Alparone et al.* [2007] observed one of three patterns of tremor amplitude increase and decay during 62 of 64 lava fountaining episodes. Different patterns dominated during different stages of the eruption suggesting they were characteristic of specific states of the magmatic system. We recorded two distinct tremor evolution patterns during three paroxysms at Fuego. The 15-16 March eruption, which showed the longest increase in background tremor energy (~20 days) and had a higher intensity spike during the two days of paroxysmal activity, is similar to the tower-shaped events of *Alparone et al.* [*Lodato et al.*, 2007] that

dominated toward the end of the Etna eruption. While our record of the July paroxysm is incomplete, it appears similar to the March eruption. These tower events indicate a rapid change in the activity. The 20-21 April eruption shows a shorter (~10 days), smoother increase and decrease in tremor energy symmetric about the two days of paroxysmal eruption, similar to bell-shaped events that dominated the beginning and middle phases of the 2000 Etna eruption. If more events can be recorded and studied at Fuego, these changes in tremor morphology may become useful for modeling the variable source processes.

The similarities in lava flow length and thermal output for the March and July paroxysms highlight differences between these events and the April paroxysm. Maximum lava flow lengths for the April event were half those observed for both the March and July eruptions, while the thermal output of the March event was nearly four times greater than that of the April event. Lava flow length and tremor energy are remarkably similar for the March and July eruptions, although the thermal output appears to be significantly lower for the paroxysmal July eruption. This is likely due to the fact that the July eruption occurred during the rainy season, and significant cloud coverage was observed during the eruption, whereas the March and April eruptions were cloud-free.

Tremor energy spiked several times during periods of passive effusion to levels approaching those associated with paroxysmal eruptions. The majority of these spikes are due to tremor bursts that are similar in spectral content and waveform to the intense tremor that is characteristic of all paroxysmal eruptions. Several short-lived spikes in

Figure 1.8 are due to regional or teleseismic earthquakes that produce energy in the tremor band. The largest spike in tremor energy not associated with a paroxysmal eruption occurred at the beginning of May 2007, concurrent with the onset of a period of lava effusion that lasted until the 1 July, 2007 eruption (Figure 1.8). The similarity between the seismic signal of a paroxysmal eruption and that of passive effusion suggests that these two different types of activity are driven by magma migration and/or gas release in the plumbing system at Fuego. Subtle spikes in the thermal output also typically accompany the increases in tremor energy, although they are much weaker than the thermal output recorded during paroxysmal eruptions. This is further evidence that the tremor at Fuego is directly related to magma migration in the conduit.

Frequency gliding in volcanic tremor has been identified at a number of volcanoes worldwide (e.g., Arenal, Karymsky, Montserrat, Lascar, Sangay, Semeru). Gliding occurs when the fundamental tremor band, and any corresponding overtones, undergo equal shifts in frequency with time [2003]. Gliding occurs throughout the seismic record during the study period at Fuego, and during all three types of eruptive activity identified. It was observed most often prior to and following paroxysmal eruptions (typically ~1 week before or after). Gliding and harmonic tremor are found less frequently in the acoustic record, only occurring simultaneously with tremor gliding in the seismicity. *Garcés et al.* [2003] observed similarity in seismic and acoustic tremor and gliding at Arenal, suggesting it reflects strong coupling of the magma's free surface with the atmosphere. Gliding has been attributed to repeatable changes in physical properties of the melt (i.e., bubble concentration) over short timescales due to degassing events or

explosions, changes in the length of a magmatic resonator, or pressure fluctuations [*Benoit and McNutt*, 1997; *Garcés et al.*, 1998; *Lees*, 2004]. At Karymsky and Sangay, gliding has been attributed to systematic increases or decreases in time between chugging events [1998]. Increasing frequency gliding at Fuego most often correlates with decreasing tremor amplitude, but sometimes the opposite effect is seen. A detailed examination of gliding at Fuego will be presented elsewhere.

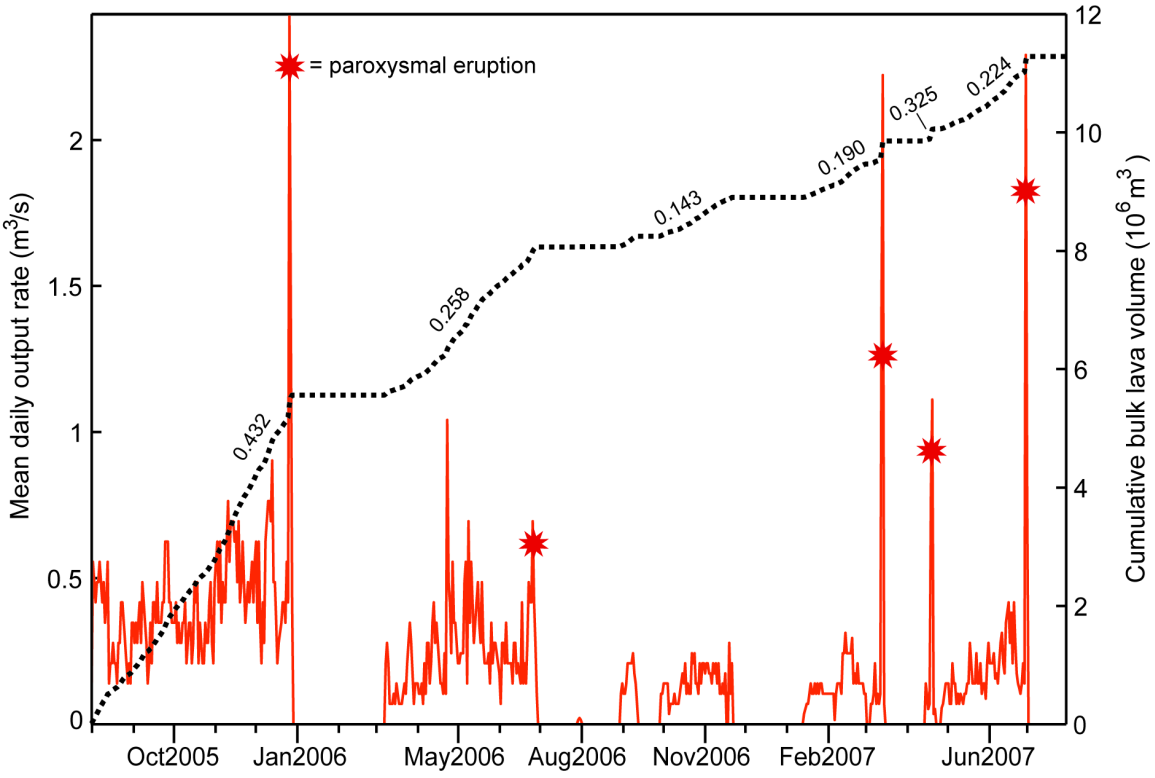

Figure 1.9. Mean daily lava output rate (orange line) and cumulative erupted volume (dotted line) from August 2005-July 2007. Slope of each major period of effusion, including the paroxysmal events (asterisks), is the number shown above the cumulative trend.

The cumulative tremor energy, cumulative active lava flow length, and cumulative thermal output (Figure 1.10) mirror the general agreement among the three

datasets demonstrated earlier. Subtle changes in tremor energy during passive lava effusion can sometimes be correlated with small changes in thermal output, which cannot always be seen in lava flow data (i.e., several increases during May). Paroxysmal eruptions are associated with sharp increases in each parameter, while periods with no lava effusion show no thermal output. Cumulative tremor energy is continuous during periods without lava effusion and remains nearly the same as during passive effusion. Continued tremor with no effusion suggests that tremor is not due to magma flow, but that the magmatic system is still resonating strongly, likely due to a gas-charged magma column residing at a shallow depth below the vent [*Julian*, 1994]. The characteristics of the degassing explosions produced during periods without lava effusion support the model of a closed or choked vent, in which gas overpressure can build above the degassing magma column [*Lees et al.*, 2004; *Lees and Ruiz*, 2008].

The sharp increase in cumulative tremor energy, thermal output, and lava flow length scale proportionally for the March and July paroxysmal eruptions (Figure 1.10). The 21 April paroxysm, however, produced significantly more tremor energy than commensurate with the observed lava flow length or the thermal output, and twice that of either the March or July eruptions. Because both the lava flow length and the thermal output are controlled by the amount of magma erupted at the surface, the data imply that less magma was erupted during the April eruption than during either the March or July eruptions. Having less magma erupt during a seismically more energetic eruption is not expected, but may be caused by the release of more gas and less magma relative to the

other paroxysms. A choked or restricted conduit that somewhat restricted the flow of magma but allowed gas to escape could be envisaged.

1.5.4. Infrasound

Infrasound recordings complement seismic data for studying the variability and evolution of volcanic explosions and for monitoring changes in eruptive behavior. Relatively simple paths from sources to receivers, compared to seismic recordings, permit more direct interpretations of infrasound data [*Chouet*, 1985]. The infrasound record quantifies the observations of explosions described above. Explosions are more frequent and have lower peak-to-peak amplitudes during periods of effusion. Periods without effusion typically have fewer but higher-amplitude "degassing explosions". Degassing explosions have impulsive onsets interpreted as rapid outward expansion of trapped gas (Figure 1.11a). The coda of ash-poor explosions decays rapidly (Figure 1.11a); these explosions are associated with a small explosion cloud primarily composed of gas. Ash-rich degassing explosions continue to vent gas and ash for tens of seconds and have an extended infrasonic coda following an impulsive onset. *Johnson et al.* [2004] proposed the fragmentation of a pressurized foam layer as the mechanism for producing the extended infrasound signal.

Explosions that occur several times per hour during effusion often have an impulsive onset and short, tremor-like coda (Figure 1.11b). These explosions are superimposed on a nearly continuous tremor-like signal that may represent degassing processes such as chugging or jetting. Explosions observed during effusive periods always ejected incandescent material and gas but produced very little ash. The

explosions are most likely due to bubbles rising through the magma column and bursting at the free surface of the magma in the summit crater. The two examples shown in Figure 3.11 are representative events from a period of degassing explosions (Figure 1.11a) and a subsequent period of lava effusion (Figure 1.11b). The pressure amplitude is reduced to a distance of 1 km from the summit, assuming spherical spreading of acoustic energy where amplitude decays as the inverse of distance from the volcano. *Johnson et al.* [2004] recorded explosions from Fuego in 2003, with reduced pressures of up to 100 Pa that sounded like distant thunder at 2.6 km. The explosion we recorded in Figure 1.11a rattled windows and shook metal roofs with a loud crack that sounded like thunder directly overhead at a distance of 7.5 km from the summit. This suggests that the apparently low 21 Pa of excess pressure calculated for this event is a minimum value; the actual reduced pressure may be several times larger due to unmodeled path affects such as refraction.

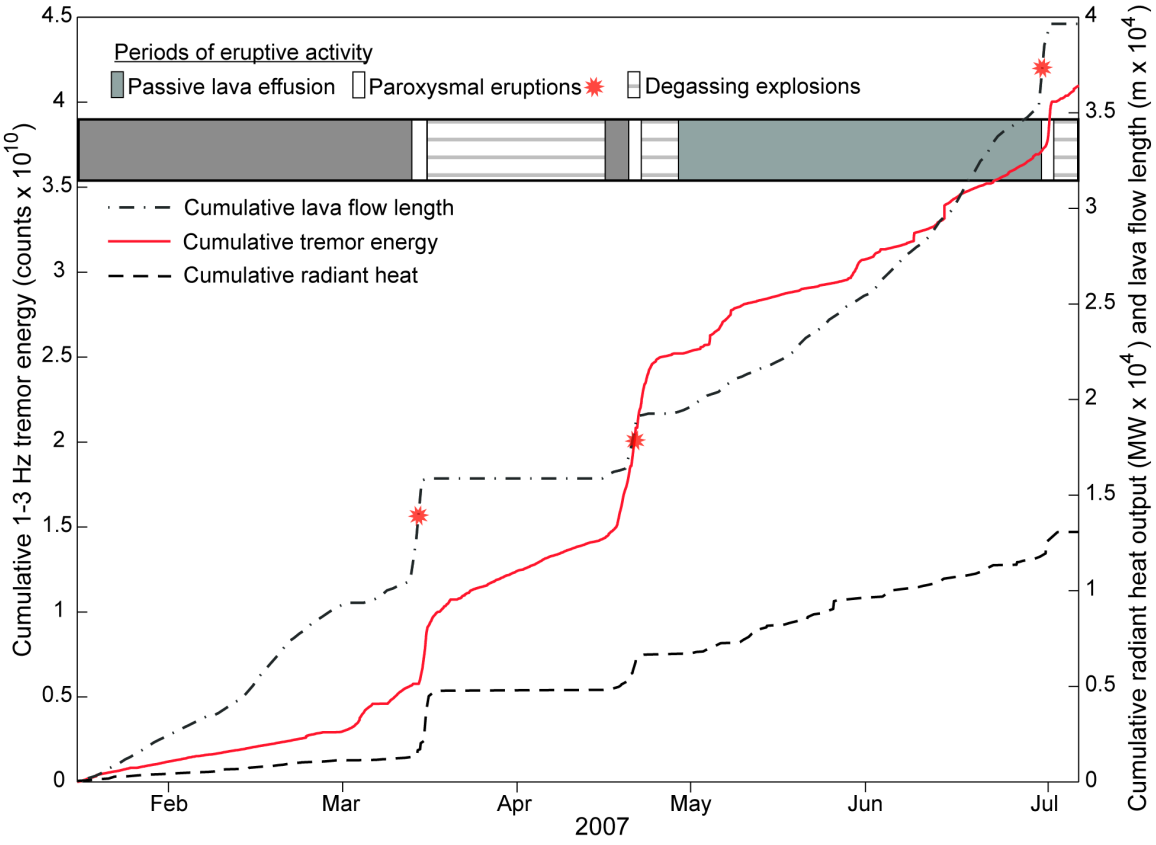

Figure 1.10. Cumulative tremor energy (red), radiant heat output (dashed) and lava flow lengths (dot-dash line) from 16 January-7 July 2007, and observed periods of activity (bar above).

A dramatic change in the characteristics of explosions observed by infrasound accompanied the emergence of a new lava flow, first seen on 1 May 2007. The excess pressure recorded at 7 km for the explosion on 27 April 2007 is 21 Pa, while on 1 May 2007 the excess pressure had dropped to 0.50 Pa, or 42 times less than three days prior. This corresponds directly to changes in the dynamics and processes acting in the upper conduit. Overpressure generated in the conduit can be many times greater during periods of degassing explosions than during passive effusion because the conduit is effectively sealed and significant amounts of gas can be trapped, possibly below a solidified cap of

lava. During effusion, the conduit remains open, and gas bubbles can escape unimpeded through the free surface of the magma column at the summit, as small strombolian explosions. This demonstrates the utility of infrasound in monitoring activity at Fuego and supplies further quantitative support for our delineation of periods of activity based on observations.

1.6. Discussion

We found no documentation of the occurrence of regular, long-duration passive lava effusion (i.e., weeks to months) preceding paroxysmal eruptions at other basaltic arc volcanoes. A similar sequence was observed repeatedly, however, during the 1969-71 Mauna Ulu eruption of Kilauea volcano [*Swanson et al*., 1979], providing some insight into the eruptive behavior at Fuego. During the Mauna Ulu eruption, long periods of passive effusion preceded episodes of sustained lava fountaining that lasted from 4.5 hours to 3 days. Following a fountaining episode, the lava column dropped below the lip of the vent and was often observed to be tens of meters below the vent. Over time the level would rise again and produce pahoehoe flows as it overtopped the vent, eventually leading to another fountaining event. The eruptive sequences observed at Fuego may be analogous to the progressions of activity during the Mauna Ulu eruption, with the magma chemistry and tectonic setting imparting significant temporal and behavioral differences during each period of activity.

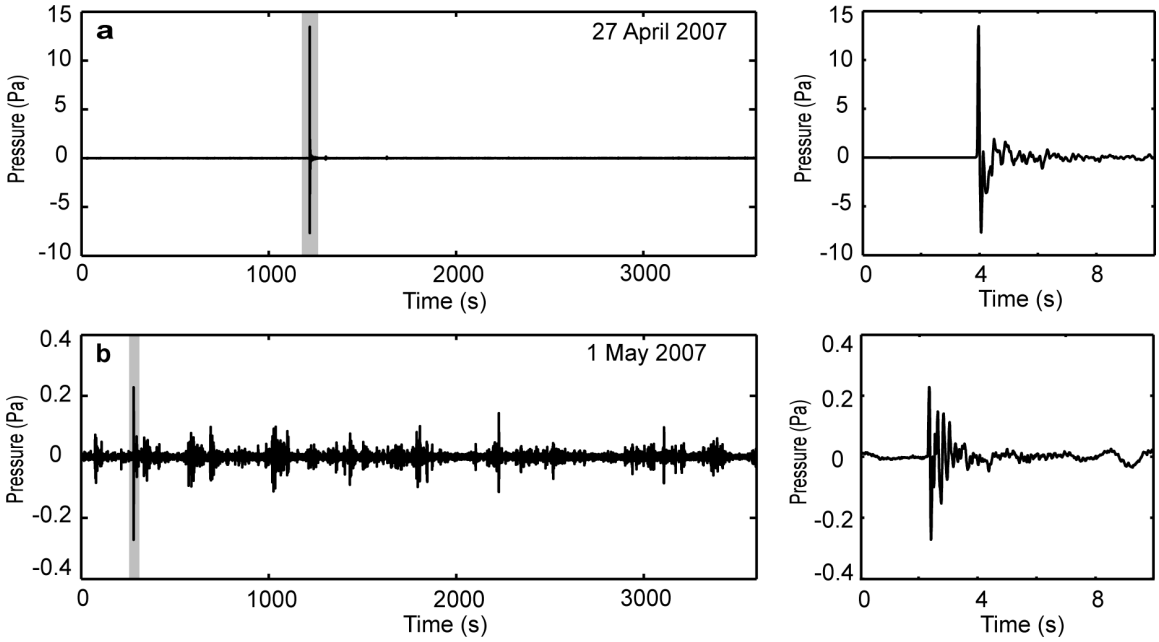

Figure 1.11. Infrasound traces during periods of a) degassing explosions and b) lava effusion and minor strombolian explosions. Pressure amplitude is reduced pressure equivalent at 1 km from the source.

Observed eruptive behavior of Mt. Etna to activity we saw at Fuego. The 2000 Southeast Crater eruption of Mt. Etna consisted of 64 individual eruptive events that occurred in a sequential pattern of 1) slow effusion and gradual increase in strombolian explosions, then 2) paroxysmal eruption of sustained lava fountains that produced long lava flows and columns of gas and ash, and finally 3) decrease in volcanic tremor and return to strombolian activity followed closely by the end of the eruptive episode [2004]. These events are similar to Fuego's eruptive sequences, with a key difference in eruptive cycle duration. Paroxysmal events at Etna were 20 minutes to 9 hours in duration, whereas Fuego's paroxysms typically lasted 24-48 hours and were preceded by weeks or months of passive effusion. Despite this difference, the similarities in tremor-dominated

seismicity and cycles of eruptive behavior suggest that using Mt. Etna as an analogue to Fuego is constructive.

Fourier transform infrared spectroscopy (FTIR) performed at Etna during one paroxysm of the 2000 Southeast Crater eruption found that gas emissions during the eruption had higher ratios of CO_2/S and S/Cl than previous measurements at Etna, and could not be accounted for by simple bulk degassing of Etna basalts during the eruption [*Swanson et al.*, 1979]. On the basis of this finding, *Allard et al.* [2005] invoke a model for Etnean paroxysms whereby a layer of volcanic gas accumulates at a structural discontinuity within the shallow plumbing system. The ascent and eruption of that gas pocket drives the paroxysms.

This model is similar to the foam layer model of *Jaupart and Vergniolle* [1988; 1989], whereby hawaiian and strombolian activity is driven by accumulation of gas in a foam layer at some structural discontinuity within the volcanic plumbing system. Moreover, they cite the characteristics of the 1969-71 eruption of Mauna Ulu (Kilauea volcano) in support of their experimental results. They propose that both passive effusion and paroxysmal phases of activity can be explained by 1) gas accumulation and growth of a foam layer allowing a period of slow effusion, followed by 2) collapse of the unstable foam layer into a gas slug that can move around the structural discontinuity and up the conduit, driving the fountaining upon its arrival at the surface. Evacuation of the foam layer at depth creates an available volume that may be filled by magma draining from the conduit. This is cited as the cause of rapid lava lake draining following the sixth fire fountaining episode in the Mauna Ulu eruption and may explain a period of decreased

activity or repose following paroxysms [*Jaupart and Vergniolle.*, 1988]. In this model, CO_2 is the primary volatile species accumulating at depth and creating large bubbles, while H_2O only exsolves very small bubbles in the upper few hundred meters of the conduit.

The growth of a foam layer is controlled by gas flux and magma viscosity and must reach a critical thickness in order to collapse [*Vergniolle and Jaupart*, 1986]. If either liquid viscosity or gas flux is insufficiently high, then foam will flow passively around the chamber roof or structural discontinuity into the conduit resulting in continuous effusive behavior. However, if the viscosity or gas flux is sufficiently high, then cyclic foam growth and collapse will occur and could produce cycles of activity similar to those observed at Fuego.

An alternative model for generating the wide range of eruptions styles seen in basaltic systems is the magma rise-speed-dependence model [*Vergniolle and Jaupart*, 1986]. At low magma rise speeds, bubbles ascend and coalesce into larger bubbles that eventually reach the free surface of the magma and burst, producing classic strombolian activity. At higher magma rise speeds, nucleating bubbles have little differential movement relative to the magma, thus much less coalescence occurs. As the magma-gas mixture ascends, it reaches the ~75% volume exsolved gas threshold of fragmentation, or run-away coalescence, deeper within the conduit. The mixture continues to ascend and decompresses, accelerating rapidly to producing a hawaiian-style lava fountain. Increasing magma rise speeds would allow for a transition in eruptive behavior similar to that observed at Fuego [*Jaupart and Vergniolle*, 1989]. With increasing magma rise

speed, widely-spaced strombolian explosions would transition into more violent and frequent explosions, much like what we observed during the transition from passive effusion and strombolian explosions to paroxysmal eruptions at Fuego. Moreover, *Parfitt and Wilson* [1995] and *Parfitt* [2004] argue that the volatile species driving explosive basaltic activity is H_2O, not CO_2 as put forth by *Vergniolle and Jaupart* [1994].

A shift in activity appears to have occurred over the course of the study period that may provide insight into conduit dynamics at Fuego. Longer periods of passive effusion and fewer paroxysmal events towards the beginning of the study gave way to shorter periods of effusion and more frequent paroxysmal eruptions in 2007 (Figure 1.9). Decreasing lava output occurs during the course of the study period, but explosivity increases. The overall decrease in output rate observed in Figure 1.9 may indicate a changing conduit configuration. A lower magma flux through the conduit would result in narrowing of the magma pathway due to enhanced cooling, crystallization, and degassing at the conduit-wallrock interface [*Parfitt*, 2004]. Partial choking of the conduit could impede the upward migration of bubbly magma, which would decrease output rate. This process could cause gas-rich magma to accumulate below the choked conduit, possibly forming a foam layer, similar to the model of *Jaupart and Vergniolle* [1986]. Additionally, changes in the foam layer thickness due to variable deep gas flux or changing magma viscosity would contribute to temporal variations in the eruptive cycles observed. The inverse relationship between frequency of paroxysmal events and output rate is difficult to relate to the magma rise speed model because the model predicts that higher effusion rates should correlate with more paroxysmal eruptions, not lower effusion

rate. If, as our data suggest, the volcano is becoming less open-vent in nature resulting in an increase in explosivity, it has significant hazard implications that warrant further research at Fuego.

1.7. Conclusions

We describe two years of daily observations of eruptive behavior at Fuego volcano, in an open-vent period of activity. The volcano was persistently active, and we observed a repeating cycle of activity: 1) passive lava effusion and minor strombolian explosion, followed by 2) paroxysmal eruptions, and finally 3) degassing explosions without lava effusion. A mean daily lava output rate of 0.18 m^3 s^{-1} was estimated from lava flow lengths. During paroxysmal events, the output rate increased by an order of magnitude. Thermal outputs from MODIS and active lava flow lengths show a robust correlation over the entire duration of the study. Our work shows that regular, systematic collection of observational data can be useful in tracking changes in volcanic activity, particularly in developing nations at populated volcanoes.

Continuous seismic data collected during the last six months of the study. Fuego produced constant, but variable-amplitude harmonic tremor during all three styles of eruptive behavior. Comparison of thermal output, tremor energy, and lava flow lengths during 2007 shows that all three data types correlate during periods of passive lava effusion and paroxysmal eruptions, but that tremor energy is emitted at the same level during periods of degassing explosions without effusion, as during periods of passive

effusion. Tremor amplitude shows promise as an eruption forecasting tool if more eruptions can be recorded and a longer continuous record constructed and analyzed.

Of the three types of activity observed during the study, the paroxysmal eruptions are the most hazardous to local populations. Our data suggests the possibility that Fuego may be shifting toward less of an open-vent configuration, which could lead to an increase in the frequency of explosive events. More detailed studies of these events and improvements in monitoring would help elucidate their source processes and potentially assist local scientists in eruption forecasting.

Acknowledgements

JJL would like to thank Eddy Sanchez, INSIVUMEH, and the Peace Corps for field support during the study period. The authors gratefully acknowledge Jeff Johnson for his field and equipment support and Rob Wright for MODVOLC data. The authors thank Rüdiger Escobar and Jose Palma for stimulating and insightful discussions. Thoughtful critiques by John Stix, Sonia Calvari and an anonymous reviewer improved the manuscript. This work was funded by NSF-PIRE 0530109 and the Peace Corps.

CHAPTER 2

Seismic and Acoustic Energy Partitioning in Explosions at Fuego volcano 2007-2009: A Potential Metric for Tracking Activity at Open-Vent Volcanoes

2.1. Introduction

Volcanic explosions that originate in the shallow plumbing system radiate energy into both the ground and atmosphere. Simultaneous recordings of this energy using seismic and infrasonic sensors provide an opportunity to characterize explosive events based on the amount of energy that propagates through the ground versus through the atmosphere. At volcanoes that erupt frequently (typically strombolian or vulcanian) continuous records may allow for detailed tracking of the variability in the ratio of infrasound to seismic energy released. Changes in energy partitioning over time, when considered with other monitoring observations, has the potential to provide valuable information on changing eruption dynamics at open vent volcanoes and possibly elucidate the dominant physical process responsible for changing activity. The effort to systematically record variations in seismic and infrasound energy partitioning is being greatly aided by the recent proliferation in the deployment of infrasound microphones alongside broadband seismic sensors at active volcanoes.

Variability in explosive energy partitioning has been observed at active volcanoes worldwide and has typically been attributed to source processes, although changing atmospheric conditions can also produce variability. At Fuego, and at many of the volcanoes highlighted below, large changes in explosive energy ratios have been recorded over such short timescales (seconds to minutes) that they cannot be caused solely by changing atmospheric conditions. Significant variability in seismic and acoustic ratios have been reported at Arenal [*Gilbert and Lane*, 2008], Karymsky [1988], Erebus [*Garcés et al.*, 1998; *Hagerty et al.*, 2000], Stromboli [*Johnson and Lees*, 2000;

Johnson and Aster, 2005], Shishaldin [*Rowe et al.*, 2000] and Langila [*Ripepe et al.*, 1993]. In each case, the variability was attributed to changes in the eruption dynamics. However, very few examples exist where explosive energy partitioning has been carefully studied over long periods that included substantial changes in eruptive behavior.

Fuego produces explosions that are, from an audio-visual standpoint, highly variable [*Lyons et al., 2010*]. Some events produce a loud report lasting several seconds accompanied by incandescent ejecta and a small eruptive cloud that is ash-poor. Other explosions emit a low rumble or are silent but eject an ash-rich eruptive cloud for tens of seconds to minutes. Between these end-members exists a spectrum of explosions of various intensities and eruptive characteristics that can likely provide valuable information about evolving eruption dynamics. Three years of seismic and infrasound records were recorded at Fuego volcano, Guatemala along with detailed descriptions of the explosive activity. We recorded hundreds of explosions at Fuego over three years (2007 – 2009) of seismic and acoustic recordings, as well as detailed audio-visual observations. We report results from a study of seismic and infrasonic energy release during explosions and how energy partitioning varies between the ground and the atmosphere. The results are discussed in terms of potential links to explosion source processes or non-volcanic sources. We end with a comparison of the Fuego data to that of other volcanoes and suggest ways to improve similar future studies.

2.2. Eruptive Activity

Fuego has been persistently erupting for decades (see *Lyons et al*., 2010 for a review) but the current eruptive phase began with a VEI 2 eruption on 21 May 1999 [*Smithsonian Institute*, 1999]. Fuego has maintained a relatively open-vent eruptive style that includes long periods of passive effusion, regular explosions and short-lived, more violent eruptions [*Lyons et al.*, 2010]. Explosion characteristics during 2007 – 2009 varied greatly and we observed that the presence or absence of an active lava flow had a strong influence on explosive characteristics (see detailed descriptions in Chapter 1.3.). Explosions occurring during active effusion are best described as strombolian, with abundant incandescent ejecta and little ash. Explosions generated during periods without effusion vary greatly in character; some are short-lived and eject incandescent similar to vulcanian explosions while others are longer duration, do not eject incandescent material and are ash-rich. The explosions studied in the 2007 data set span all the current explosions types, while the shorter deployments in 2008 and 2009 capture less variability. The January and June 2008 datasets recorded periods of ash-rich explosions and strombolian explosions, respectively. The 2009 record begins just after the cessation of an active lava flow and captured a wide variety of events, but the largest explosions were more similar to vulcanian than strombolian explosions.

2.3. Data Acquisition

Data was recorded in 2007, 2008 and 2009 using short-period and broadband seismic and broadband infrasound sensors. The 2007 data were recorded near the

observatory maintained by the Instituto Nacional de Sismologia, Vulcanología, Meterología e Hidrologia (INSIVUMEH) ~7 km southwest of the active vent at an elevation of 1100 m (Figure 2.1). The seismic and acoustic station consisted of a Geospace GS-1 short-period (1 Hz) seismometer and two low-frequency microphones (30 s low corner) recording on a Reftek 130 digitizer operating in continuous mode at 100 samples per second and equipped with Global Positioning Systems (GPS) timing. Data were collected nearly continuously from 16 January – 7 July 2007 (172 days). In 2008, data were collected ~1 km north of the active summit vent at 3600 m elevation during 14 – 16 January and 27 June – 1 July using Güralp 40T (0.02 – 30 s) and 3 ESPC seismic sensors (0.02 – 60 s) and All Sensors differential pressure transducers (0.001 – 50 s) with a ± 250 Pa dynamic range (Figure 2.1). The 2009 data were recorded using the same instruments as in 2008, with stations distributed azimuthally around the upper cone, but with the closest station located within meters of the closest station location in both 2008 experiments.

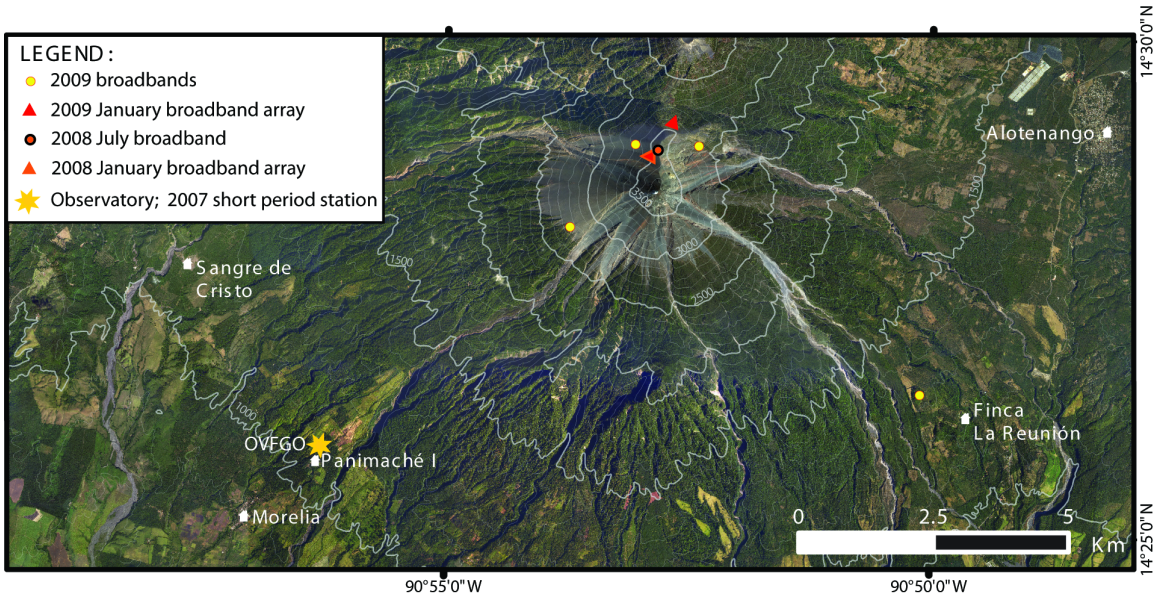

Figure 2.1. Map of Fuego volcano with the locations of the 2007, 2008 and 2009 seismic and infrasound stations. Population centers are also shown with names in white. Contour interval is 100 m.

2.4. Seismic and Acoustic Energy Partitioning

Explosive energy partitioning can be determined in three main ways: 1) comparing the seismic amplitude and ground-coupled air wave amplitude in the seismic traces (no dedicated acoustic sensor), 2) calculating the maximum amplitude of the explosion in the seismic and acoustic traces and comparing the ratio and 3) calculating the amount of radiated seismic and acoustic energy released over the duration of the explosive event. The third method was developed by Johnson and Aster [Smithsonian Institution, 1999] and dubbed the volcano acoustic seismic ratio (VASR). The first method allows for a qualitative analysis of the ratio of seismic to acoustic energy released; however, a detailed study of the partitioning is difficult because the only recording of the energy released in to the atmosphere comes as the ground-coupled air

wave, which is convolved with the seismic wave. Comparing the maximum amplitude of the seismic and infrasound signal is an improvement over having only one measurement, but the duration of the events is not considered and it is often the case that the ground-coupled air wave produces the highest amplitude signal in the seismic trace. Many explosions also diverge from being simple, short impulses and produce signals that are recorded in both the seismic and the acoustic channels for tens of seconds to minutes.

The VASR method is an improvement over simple maximum amplitude ratios because it includes all the energy released over the course of an explosion. This is a more accurate representation of the total explosive energy released, particularly for long-lived events. However, use of the VASR has not been widely adopted and comparison of the VASR between more volcanoes is needed for validation. We apply this method to the seismic and infrasound records at Fuego because we had four datasets spanning three years that included explosions that had a wide variety of characteristics, and because the VASR for strombolian explosions at Erebus and Karymsky volcanoes had already been calculated and could be compared to the Fuego VASR [*Johnson and Aster*, 2005].

2.4.1. VASR Method

Low frequency acoustic energy radiated isotropically from a monopole source into a hemispherical half space can be expressed as the integral of the squared pressure (ΔP^2) divided by the speed of sound in the atmosphere ($c_{atmosphere}$) and the air density ($\rho_{atmosphere}$) after *Johnson and Aster* [2005]:

$$E_{acoustic} = \frac{2\pi r^2}{\rho_{atmosphere} c_{atmosphere}} \int \Delta P(t)^2 \, dt \qquad (2.1)$$

Estimating the seismic energy radiated by explosions is more difficult due to the more complex and unknown path and the presence of both P and S body waves and surface waves. *Johnson and Aster* [2005] make the simplifying assumption that velocity waveforms are representative of seismic kinetic energy density at the receiver location, and, via the equipartition theorem, that the kinetic energy density is equal to the potential energy density. The total seismic energy is then equal to the product of the square of the particle velocity (U^2), the density of the earth (ρ_{earth}) and a fixed P-wave velocity (c_{earth}) integrated over the edifice volume, after *Johnson and Aster* [2005]:

$$E_{seismic} = 2\pi r^2 \rho_{earth} c_{earth} \int U(t)^2 \, dt$$

(2.2)

This equation assumes isotropic radiation from a source located on the top homogenous half space. The ratio of the estimated acoustic energy ($E_{acoustic}$) to the estimated seismic energy ($E_{seismic}$) results in the volcanic acoustic seismic ratio (VASR):

$$VASR = \frac{E_{acoustic}}{E_{seismic}} \qquad (2.3)$$

VASR is non-dimensional and was developed with the goal of being able to elucidate changing explosion source processes at volcanoes with frequent explosions, as well as a metric to compare explosive energy partitioning between different volcanoes.

2.4.2. Fuego VASR

Individual explosions were handpicked from each dataset using hour long seismic and infrasound traces bandpass filtered from 0.5 – 10 Hz with a 2-pole zero-phase-difference Butterworth filter. Picking was done with a MATLAB® algorithm that allows the user to zoom in on events and inspect them in detail prior to event picking. Once the onset of an event is selected by the user, the algorithm determines the end of the event by comparing the amplitude of the pre-explosion noise with that of the coda. In cases where anomalously high background noise existed, usually due to high winds in the infrasound or strong tremor in the seismic, we manually picked the end of the explosion by fixing the window length over which the calculations were run. Fixed parameters for the energy calculations are: $c_{atmosphere}$ (340 m/s), $\rho_{atmosphere}$ (1.2 kg/m^3), ρ_{earth} (2000 kg/m^3) and c_{earth} (2500 m/s). The distance from source to receiver for the 2007 dataset is 7 km, while a 1 km distance was used for the 2008 and 2009 datasets. In addition to the VASR, the following parameters are calculated for each explosion: start time, event duration, maximum amplitude, acoustic to seismic amplitude ratio, total seismic energy and total acoustic energy. These parameters were determined for 967 explosions in 2007, 19 explosions in January 2008, 42 explosions in June 2008, and 243 explosions in 2009. In each case the vertical component was used to calculate the seismic parameters and two

microphones were used to view and calculate the acoustic parameters in order to confirm that events were not spurious wind or atmospheric noise.

2.5. Results

2.5.1. 2007 Explosive Energy Partitioning

The energy partitioning values from the 967 explosions analyzed over 6 months in 2007 show a wide range in values (VASR 0.0013 – 2.56). Unfortunately, no clear correlation between periods of eruptive behavior and the VASR value exists (Figure 2.2). We attribute this to the lateral distance (7 km) and ~3 km elevation difference between the sensors and the vent (Figure 2.1). At distances greater than several kilometers from the vent the spreading of acoustic energy becomes non-spherical, which would lead to erroneous acoustic energy values [*Johnson and Aster*, 2005]. Although the seismic record is certainly scattered, reflected and refracted due to the inhomogeneity of the path, the acoustic waves are also susceptible to refraction and ducting due to wind and temperature variations in the atmosphere [2005]. *Fee and Garćes* [2007] recorded diurnal variations in infrasound at Pu`u `Ō`ō which they attributed to the nocturnal boundary layer (NBL). The NBL causes sound waves that would normally get refracted up into the atmosphere during the day to be refracted downward at night. This effect and the strong difference in direction and velocity of winds at 1 km and 4 km elevation are the most likely source of error in the 2007 VASR values. While it is possible to account for wind and temperature variations, detailed records are not available for the area including Fuego so we are unable to correct the 2007 infrasound data reliably.

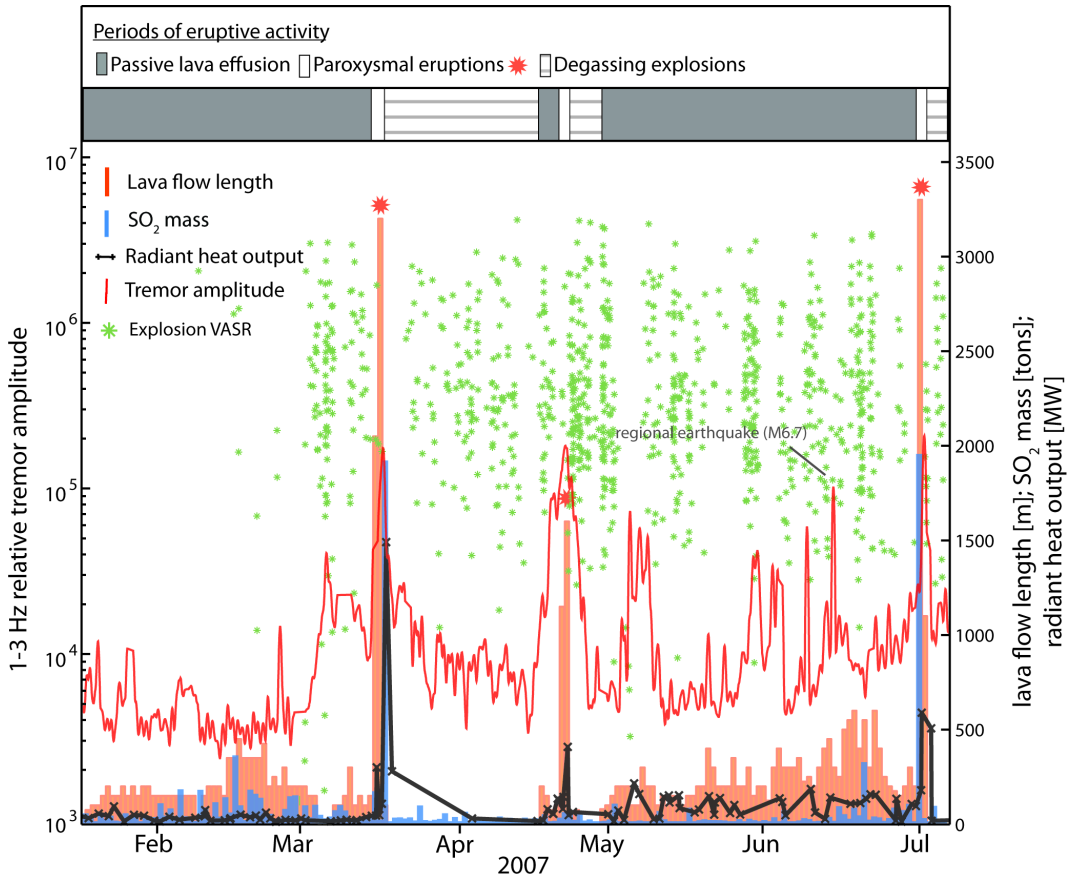

Figure 2.2. Explosion VASR for 967 explosions recorded during 2007 plotted on a log scale (not shown). VASR values plotted with lava flow length, SO_2 emissions, heat output and tremor amplitude (see Chapter 1.4. for details).

2.5.2. 2008 Explosive Energy Partitioning

The two periods of seismic and infrasound recordings in 2008 recorded different styles of explosive activity. The explosions recorded in January are deemed degassing explosions after *Lyons et al.*[2010] and are best characterized by relatively impulsive seismic and infrasound signals with high-amplitude, long-lived codas (Figure 2.3). These explosions released ash-rich plumes, often continuously for 60 – 120 s (Figure 2.3). The explosions recorded in June and July 2008 are most like the strombolian explosions occurring during periods of passive lava effusion [*Lyons et* al., 2010]. According to the

INSIVUMEH observers stationed at Panimaché, a short (~150 m) lava flow was actively flowing from the summit crater onto the southwestern flank for the duration of our experiment. The strombolian explosions are best characterized by impulsive infrasound onsets and simple N-shaped waveforms with little or no code (Figure 2.4). The seismic waveforms are emergent and low frequency and the ground-coupled air wave is often the highest amplitude portion of the signal (Figure 2.4).

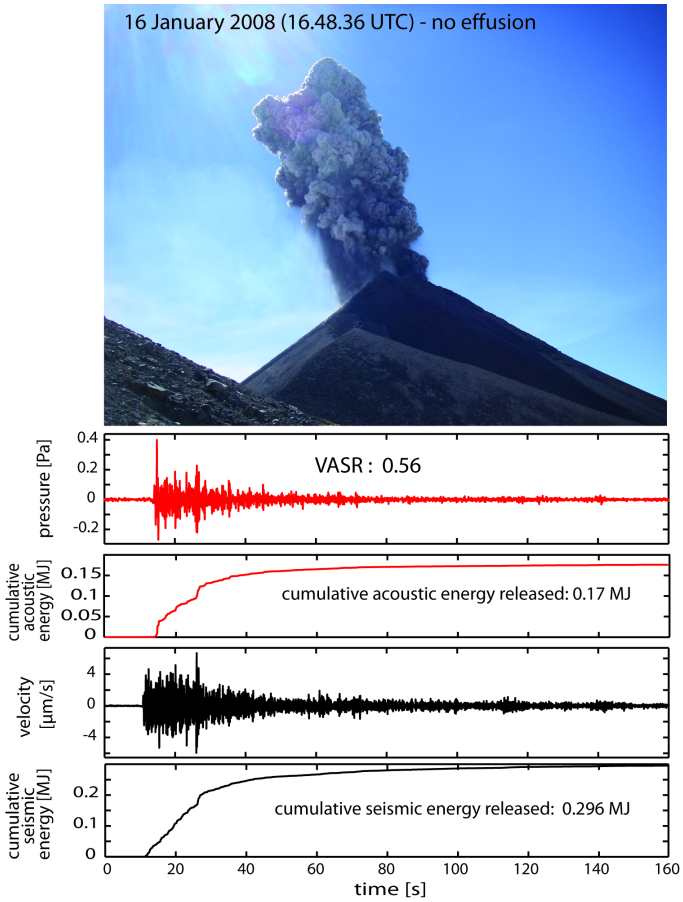

Figure 2.3. A representative degassing explosion recorded during the January 2008 experiment. Acoustic pressure history and cumulative energy released is shown in red and seismic velocity and cumulative energy released is shown in black. The VASR for this event is 0.56.

Figures 2.3 and 2.4 show the cumulative seismic and acoustic energy releases for two representative explosions during the 2008 experiments. The two different styles of explosive eruption are reflected in how they release energy. The degassing explosion releases energy slowly and over a longer period of time, whereas the strombolian explosion releases all the acoustic energy and most of the seismic energy within the first seconds of the explosion onset. The degassing explosion also shows more complexity in the waveform, with the highest seismic amplitude recorded ~10 s after the onset of the explosion (i.e., ~25 s, Figure 2.3). The same peak is seen in the infrasound but the amplitude is not as high, although the secondary event can be clearly seen as a sharp increase in both the cumulative energy plots (Figure 2.3).

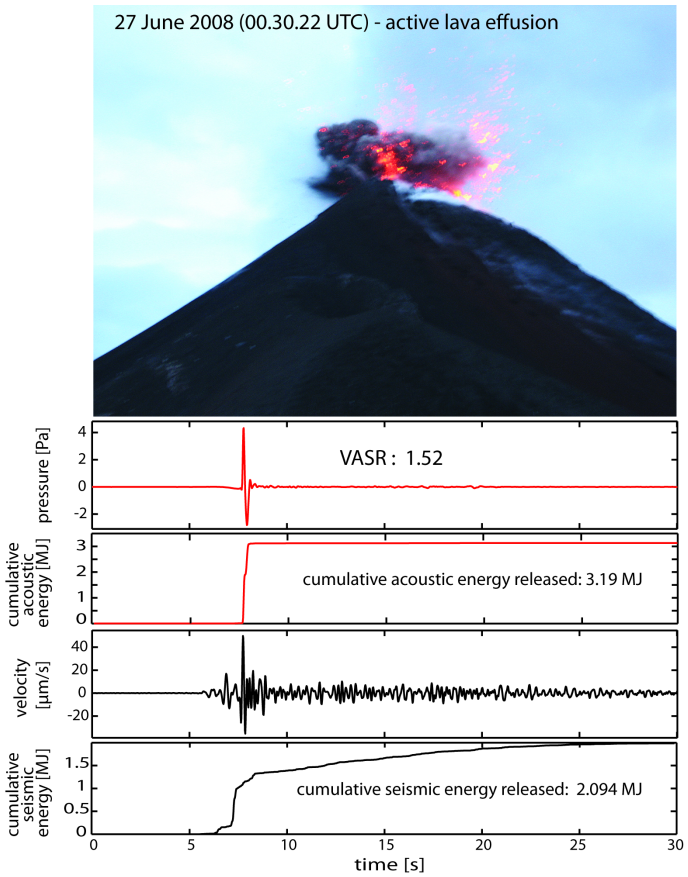

Figure 2.4. A representative strombolian explosion recorded during the June / July 2008 experiment. Acoustic pressure history and cumulative energy released is shown in red and seismic velocity and cumulative energy released is shown in black. The VASR for this event is 1.52.

Table 2.1 shows the difference between the durations of the events in January 2008 and June / July 2008. However, despite the clear difference in observed explosive character and duration, the average VASR numbers are similar (Table 2.1). This highlights a potential shortcoming of this method: the VASR can remain constant if the seismic and acoustic energies increase or decrease concomitantly. This seems unlikely for drastic changes in eruptive behavior, but it is possible that for minor changes in activity the VASR is not a sensitive indicator. Another possibility is that the short

duration of the 2008 experiments did not provide a sufficiently representative dataset of explosions to investigate minor changes in VASR.

Table 2.1 2008 and 2009 Explosion Statistics[a]

	January 2008	June / July 2008	January 2009
mean VASR	4.31 (1.93)	5.95 (4.07)	46.17 (50.87)
mean seismic duration (s)	151.50 (58.86)	106.87 (54.79)	107.18 (81.05)
minimum seismic energy[b]	0.18	0.05	0.002
maximum seismic energy[b]	1.06	7.28	44.91
mean seismic energy[b]	0.15 (0.08)	0.46 (0.52)	0.51 (1.36)
mean acoustic duration (s)	58.66 (19.98)	8.38 (5.91)	15.63 (15.03)
minimum acoustic energy[b]	0.10	0.03	0.004
maximum acoustic energy[b]	1.72	32.67	2194.10
mean acoustic energy[b]	0.66 (0.51)	3.41 (5.67)	46.01 (172.18)

[a]19, 42 and 243 explosions are used in the calculations for the January 2008, June/July 2008 and January 2009 experiements, respectively. [b]All energy values are reported in megajoules (MJ). Standard deviation of duration and energy are reported in parethesis.

2.5.3. 2009 Explosive Energy Partitioning

The explosive activity recorded in 2009 falls outside the three broad categories put forth by *Lyons et al.*[2010]. INSIVUMEH observers reported that a small lava flow had been active until ~1 week prior to our arrival, at which time effusion ceased and was absent for the duration of the experiment. Explosions in 2009 had a wide spread in energy release, spanning 4 and 6 orders of magnitude for seismic and infrasound, respectively (Table 2.1). The average seismic duration and energy released for explosions in June / July 2008 and January 2009 does not vary significantly. However, a

major change occurred in the infrasound with large explosions producing pressures over 1000 Pa at ~1 km. This results in acoustic energy releases that are on the order of 100 times greater than the largest explosions record in 2008.

Figure 2.5 illustrates the variation in the VSAR during the 2009 experiment. This ~30 minute period was particularly active with four explosions clearly recorded in the seismic and infrasound, three of which are relatively strong explosions that typically occurred several hours apart during the rest of the experiment. The infrasound waveforms are relatively simple and short duration for all the explosions; however, the seismic waveforms vary significantly between events. The differences in the explosion seismicity for these 4 events clearly impacts the VASR results (Figure 2.5) and highlights the importance of considering waveforms and spectral content along with VASR. For example, the onsets of explosions 1 and 2 are similar, but explosion 2 has a secondary increase in amplitude that is absent in explosion 1. There is a striking difference in the amplitude of the explosion onset and the amplitude of the secondary pulse between the seismic and infrasound traces (Figure 2.5a and b). The high amplitude of the secondary seismic signal relative to the secondary infrasound signal suggests that, with respect to the initial event, substantially more of the energy released in the secondary event couples to the ground than the atmosphere, causing the large VASR change from explosion 1 to explosion 2.

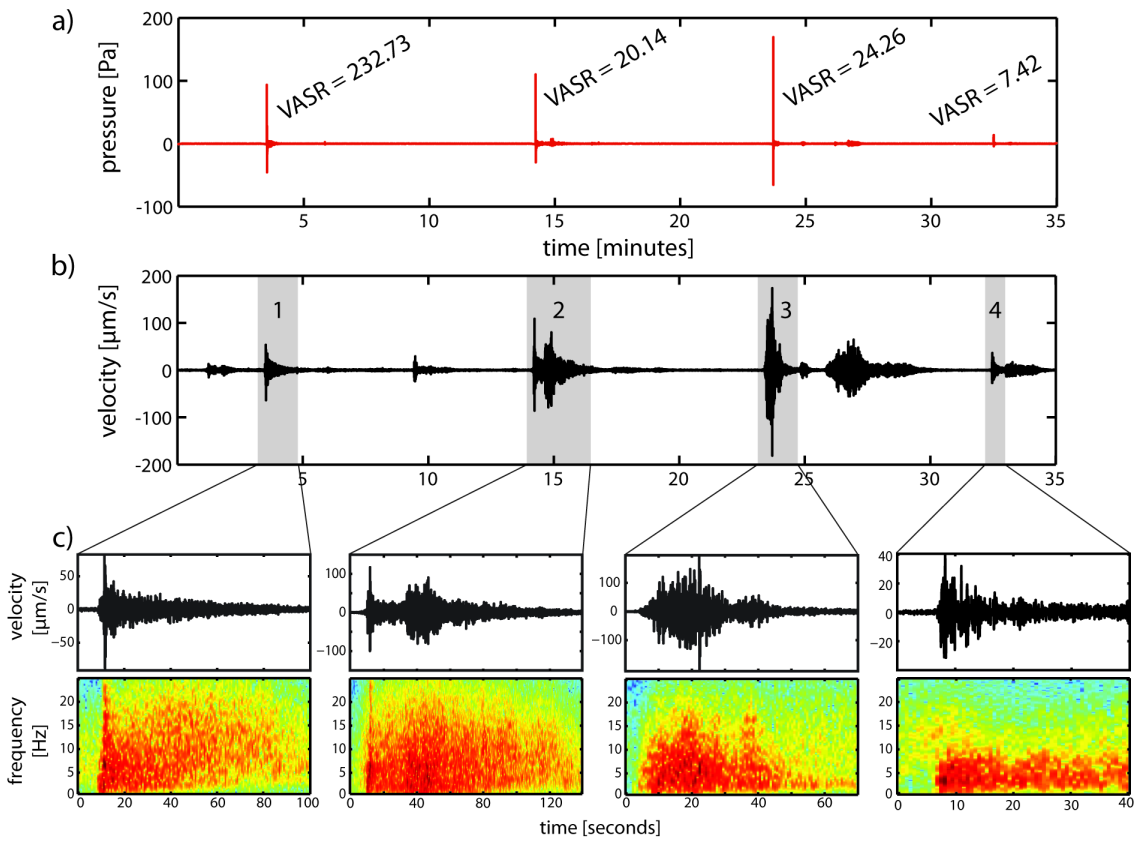

Figure 2.5. Infrasound (a) and seismicity (b) during 35 minutes of activity on 20 January 2009. Four explosions were recorded that show rapidly changing VASR values (a) and are numbered 1 – 4 for reference (b). Grey boxes in (b) highlight section of seismic traces used for the expanded traces and spectrograms in (c).

The seismic and infrasound amplitudes are highest overall for explosion 3, but the VASR is ten times lower than explosion 1. The seismicity of the third explosion also lacks the impulsive and broadband onset that explosions 1 and 2 share, and instead shows a more emergent, low-frequency signal that increases in amplitude until the arrival of the ground-coupled air wave ~15 s after the onset of seismicity. The station where this data was recorded was ~900 m from the summit vent of Fuego and using the speeds of sound for the earth and atmosphere from section 2.4.2. we would expect the infrasound arrival to lag the seismic arrival by just over 2 seconds for a co-located source. This is not the

case for explosion 3 and points to a significant change in dynamics between explosions 1 and 2 and explosion 3. Despite producing more overpressure than explosions 1 and 2, the ground-coupled air wave of the third explosion is not clearly discernable in the spectrogram, unlike in the first and second events. This is most likely due to the strength of the low frequency seismic signal dominating over the higher frequency ground-coupled air wave.

Explosion 4 is significantly less energetic in the seismic and infrasound than the other 3 explosions. The onset is relatively impulsive similar to explosions 1 and 2 but the high frequency component of the ground-coupled air wave is either missing or overwhelmed by the strength of the low frequency seismicity like explosion 3. The fourth explosion is overall the lowest frequency event and has the lowest VASR. One potentially interesting trend in this series of explosions is the general shift toward predominance of low frequency seismic energy and a concurrent decrease in the VASR values; however, sequences like these are rare and many more would have to be studied in order to validate this observation.

2.5.4. Validation of Seismic Energy Release

We used different seismic sensors during 2008 and 2009 and, although very near, installed the sensors in slightly different locations. In order to be sure that changes in the seismic energy calculations were not due to different instrument noise or site changes, we test the seismic background levels during three periods of background noise when volcanic activity was low. Fuego regularly produces tremor, but each 100 s time window represents a time when tremor was very low or absent. The data are filtered from 20 – 3 s

to further exclude the bands that normally contain volcanic energy, and then the seismic energy is calculated. Table 2.2 shows the results of the noise test and Figure 2.6 is a plot of the vertical channel for one of the time samples from each experiment period. These results show that there is little variation in the background noise between instruments or sites, and we can attribute variations in calculated seismic energy to changes in seismic energy radiated from the explosions.

Table 2.2. Seismic Noise Test 2008 - 2009[a]

sample time	duration (s)	seismic energy ($MJ*10^{-4}$)
1/16/2008 17:45	100.2	1.4806
1/16/2008 21:13	100.04	1.358
1/17/2008 1:03	100.24	2.1532
mean January 2008	100.16	1.6639
6/28/2008 20:55	100.21	1.4761
6/27/2008 21:39	100.08	1.3001
6/29/2008 10:35	100.13	1.8839
mean June 2008	100.14	1.5534
1/11/2009 20:44	100.18	1.196
1/12/2009 9:25	100.22	2.494
1/13/2009 0:47	100.13	2.0698
mean January 2009	100.18	1.9199

[a]Grey bar highlights the averge results for each experiment.

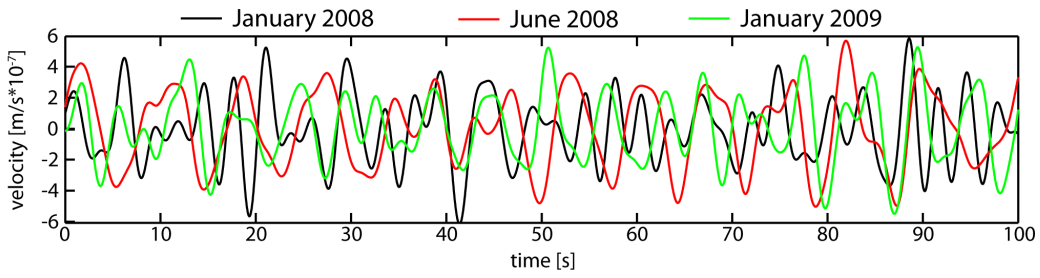

Figure 2.6. Seismic traces from the vertical channel of volcanically quiet periods during each experiment in January 2008, June 2008 and January 2009. The results confirm that differences in sensor or site response are not the primary cause of variation in the seismic energy released between experiments.

2.6. Discussion

The variability in explosive energy partitioning recorded at volcanoes around the world has been attributed to numerous source processes, changes in vent and conduit geometries and variations in source depth. *Mori et al.* [1989] presented some of the first observations of variations in seismic signals and ground-coupled air waves for explosions at Langila volcano. They noted that explosion signals often contain either sharp seismic onsets with relatively weak air wave arrivals or weak, emergent seismic onsets and sharp air wave arrivals. This relationship was attributed to changing explosion source depth, with deeper explosions coupling more strongly into the ground and producing weaker ground-coupled air waves. An intermediate type of explosion was also observed at Langila where a large ash cloud and strong seismic signal were observed with little or no acoustic signal. *Mori et al.* [1989] suggested that for these events the majority of the explosive pressure was expended by pushing the explosion out through a clogged vent.

Garćes et al. [1998] and *Hagerty et al.* [2000] recorded time-varying explosive energy partitioning for explosions at Arenal volcano, and report a frequent trade-off

between seismic and infrasound amplitudes, like at Langila. However, they discount the possibility that the variation represented changes in source depth because the latencies between explosion P-wave and infrasound first arrivals were consistent. Instead they prefer the model of *Benoit and McNutt* [1997] in which an unsteady supply of magma leads to density stratification and highly variable acoustic velocities over short distances in the shallow conduit. The time-varying energy partitioning is a result of changing impedance of the gas-charged magma, where the explosions originate. The explosion energy preferentially couples to either the earth or atmosphere, depending on which more closely matches the impedance of the magma. The acoustic velocity of the magma is able to change velocity relatively quickly due to the explosive release of overpressure and progressing degassing.

Rowe et al. [2000] compare seismic and acoustic amplitude ratios for hundreds of lava lake explosions at Erebus using $\log_{10}$ seismic amplitude / acoustic amplitude and found long periods of stable ratios punctuated by short periods with high variability. They attributed most of the variability, manifest as low seismic / acoustic ratios, to the smallest bubble bursts occurring in the low-velocity (i.e., poor seismic coupling) upper layer of a density-stratified lava pond. A shift in magma properties that would affect viscosity (i.e., temperature, volatile content, composition) could similarly be envisaged to influence energy partitioning. *Johnson and Aster* [2005] outline four important variables that may result in variable VASR values, some of which are detailed in the previous examples: 1) plume density (Langila) , 2) variable impedance contrasts (Arenal, Erebus), 3) depth to source (Langila) and 4) source dimensions. As noted earlier, the difficulty

arises in attributing variable VASR to a single dominant variable rather than multiple factors acting in concert.

The four explosions in Figure 2.5 all occur within a sufficiently short period to eliminate changes in conduit dimensions as a potential source of the variable VASR. The progressive shift from higher to lower frequencies in seismic energy could be the result of changing impedance as the magma was progressively degassing following explosion 1 and sound speed was increasing. However, the significant change in latency between the seismic onset and arrival of the ground-coupled air wave between explosions 1 and 2 and explosions 3 suggests that the explosion source depth increased between event 2 and 3 (Figure 2.5). A deeper source depth would cause result in more of the explosive energy being transmitted through the ground, resulting in the lower VASR values between explosions 1 and 3. A deeper source would also result in the preferential transmittance of lower frequency energy and the attenuation of higher frequency energy. Explosions 1 and 2 have the separation between the seismic and acoustic arrivals expected for shallow sources, but very different VASR. This difference is almost certainly due to the change in the energy partitioning for the secondary event (Figure 2.5), but what is unclear is how the secondary event is related to the initial explosion. From the infrasound and seismic arrivals it does not appear that the two events are spatially separated. It is possible that in the ~30 s between the initial explosion and the highest amplitude of the secondary event that the magma acoustic velocity changed sufficiently to cause the drop in the VASR, but seemingly equally likely is that material from the initial explosion clogged the vent and caused a preferential reduction in the amount of elastic energy available to produce

infrasound [*Johnson and Aster*, 2005]. Another possibility is that the events are not genetically related and should not be considered together for a single VASR. It becomes clear that for comparing individual explosions the VASR results in non-unique interpretations and might be more useful when used in conjunction with other data and careful consideration of waveform and spectral attributes. Cluster analysis has been used to identify families of explosions on large datasets and could be useful for further analysis of the 2009 data along with any longer-term datasets collected in the future [*McGreger and Lees*, 2004].

Figure 2.7 shows the seismic and acoustic energy calculated for all the explosions recorded in 2008 and 2009 plotted with fields depicting the extent of energy released in explosions at Karymsky (1998 – 1999) and Erebus (1999 – 2000) volcanoes from *Johnson and Aster* [2005]. The Erebus data are plotted together because of the remarkable consistency in the ratio of explosive energy released. Erebus has a long-lived lava lake and explosions are typically bubble bursts at or near the surface of the lava, which indicates a highly repetitive and temporally stable source [*Rowe et al.*, 1998; *Rowe et al.*, 2000]. The Karymsky explosions display much more variability both within and between datasets, and is attributed to a more complex conduit and vent geometry and explosion mechanism than at Erebus [*Johnson and Aster,* 2005]. Given the uncertainty in interpreting short-term variability in energy partitioning, studying longer-term variations and comparing volcanoes with different magma chemistry and tectonic environments might prove more relevant.

Explosive energy ratios for the two 2008 Fuego datasets generally overlaps, although the strombolian explosions have a tendency to produce more energetic explosions (Figure 2.7). The 2009 data show a much wider variation in energy ratios and explosion energy released, but the most interesting change is the shift toward higher energy events, particularly in the infrasound. Since the 2008 and 2009 data were collected at the same distance and elevation from the vent using the same instruments, we can assume that this shift represents a real change in explosive energy partitioning. The 2009 explosions were qualitatively more energetic based on our audio and visual observations, and the infrasound confirms that much higher overpressures were being generated in 2009 than in 2008. Greater overpressures could be generated by bring gas slugs up from a greater depth or increasing the yield strength of the magma by increasing viscosity and crystal content.

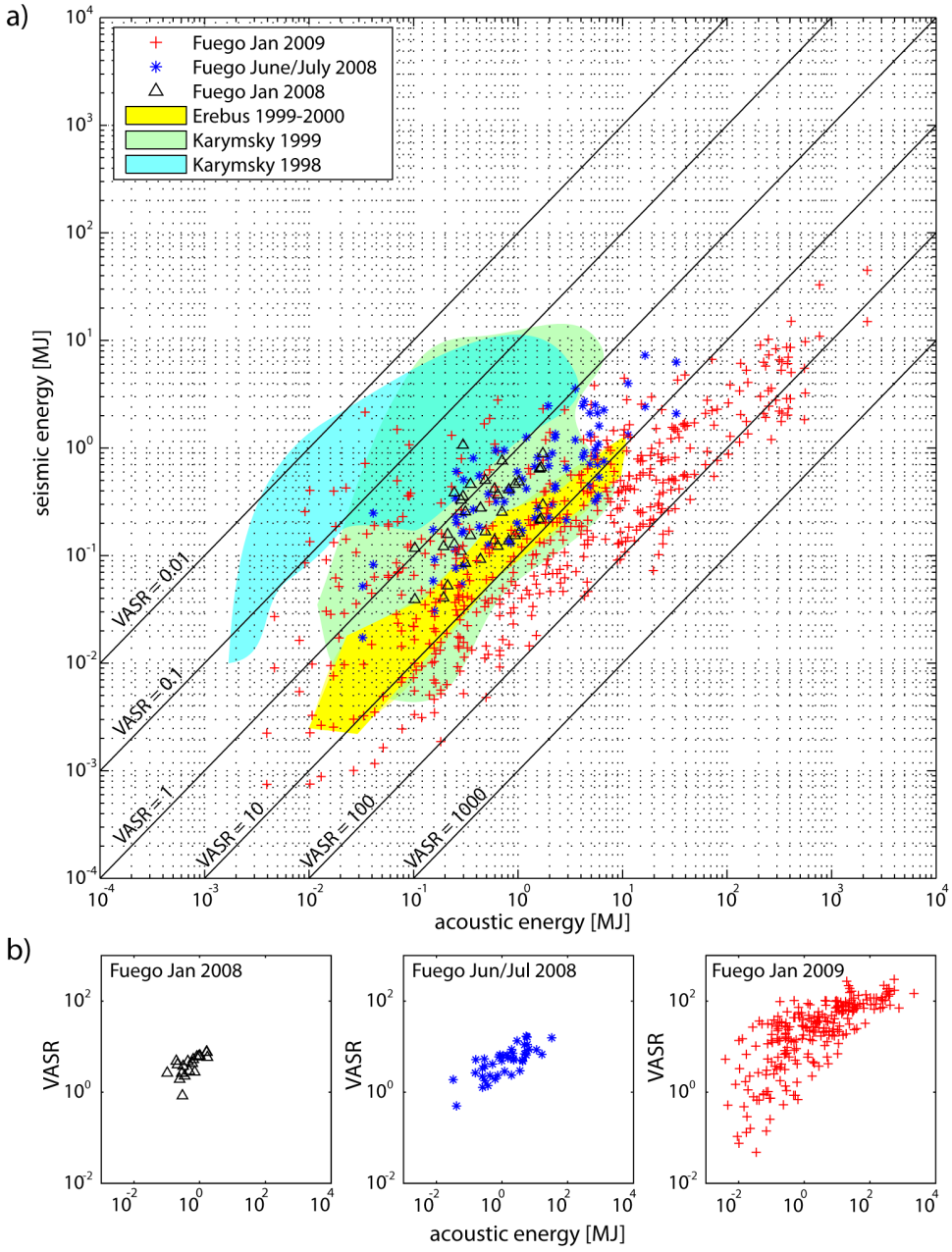

Figure 2.7. Seismic and acoustic energy ratios (a) for explosions recorded at Fuego in 2008 and 2009, plotted together with data from Karymsky and Erebus (*after Johnson and Aster* [2005]). VASR for individual experiments at Fuego (b) shows greater variability in the 2009 explosions.

Based on the seismic and acoustic signals and our observations of the explosions, we think that it is highly unlikely that the 2009 explosions were simple bubble bursts. These explosions produced substantial incandescent ejecta and threw meter-sized bombs hundreds of meters from the vent, which seems unlikely from simple bubble bursts. Fuego magmas are volatile rich (2.1 – 6.1 wt% H_2O) [*Johnson and Lees*, 2000; *Johnson and Aster*, 2005] and the loss of water from basalts during ascent causes undercooling, which promotes crystal growth and further exsolution, and results in basalts with high yield strengths [2005]. This model applies to Fuego and may explain the shift in energy partitioning between 2008 and 2009 (Figure 2.6). Chapter 3 explores the energetic explosions recorded in 2009 and the insights they provide about eruption dynamics at Fuego and conduit geometry.

2.7. Conclusions

We analyze the seismic and acoustic energy partitioning for explosions recorded at Fuego volcano during four separate experiments from 2007 – 2009 in order to test the validity of the VASR method and its utility in understanding the causes of variable energy partitioning. Six months of explosions recorded in 2007 recorded 7 km from the summit vent do not show any correlation with activity. This is most likely due to modification of the infrasound by wind and refraction off thermal boundary layers that can become dominant at the distance and a difference in elevation of (~ 3 km) between the source and the sensors. The 2008 and 2009 experiments were conducted at ~ 1 km from the summit and produced much improved results. Two different styles of

explosions were recorded between January 2008 and June 2008. The January 2008 degassing explosions were less energetic, longer duration and erupted more ash than the June 2008 strombolian explosions, which were accompanied by lava effusion. The average VASR in January 2008 is 4.31 and in June 5.95. Visually and audible, the explosions were very different and were the result of different source processes, but the energy partitioning ratios did not reflect this difference, possibly aided by small sample populations.

A greater number of explosions were recorded in 2009 and a large degree of variability in explosive energy release was found. We investigated variable energy partitioning in four explosions that occurred in ~30 minutes and found that the VASR can act as a guide toward interpreting the cause of short-term changes in energy partitioning. However, waveform comparisons, spectral content and other types of data are needed in order to more fully understand the cause of rapid shifts in energy partitioning. A potentially more useful application of the energy partitioning ratios is to look at how energy partitioning changes over the long-term and how it can be related to eruptive activity, and also how energy partitioning compares between volcanoes. Comparing the 2008 and 2009 Fuego explosions to existing data from Karymsky and Erebus, we see that Fuego produces explosions with a wider range in energy release, and also that volcanoes with very open conduits and lava lakes are more likely to have more stable energy partitioning. The most interesting result of this comparison is the clear shift toward higher acoustic energy release at Fuego between 2008 and 2009. We attribute this shift toward greater overpressure to be due to an increase in magma viscosity and the

development of a yield strength, possibly due to degassing-induced crystallization in a stagnant magma column.

CHAPTER 3

Dynamics of Explosive Volcanism at Fuego volcano Imaged with Very-Long-Period Seismicity

The material contained in this chapter has been submitted for publication:

Lyons, J.J., G.P. Waite**,** Dynamics of explosive volcanism at Fuego volcano imaged with very-long-period seismicity, *Journal of Geophysical Research*, in review

Abstract

The current activity at Fuego volcano, Guatemala is characterized by frequent explosions, intermittent lava flows and persistent degassing. Seismic and infrasound data of explosive activity recorded in January 2009 on a temporary broadband network show that explosive intensity is highly variable. The largest explosions are accompanied by very-long-period (VLP) earthquakes that show considerable waveform similarity over the 19 days of recording. Waveform inversion of the seismic data in the 10 – 30 s band was performed to constrain the location of the source centroid and to model the source mechanism of the VLP events. The location of the synthetic source that best fits our data lies 300 m below and 300 m west of the summit crater. The calculated moment tensors indicate a volumetric source, which is modeled as a near-vertical dike feeding a SW-dipping (35°) sill that intersects the summit crater. The pressure history of the sill is interpreted as: 1) an initial inflation due to pressurization, followed by 2) a rapid deflation as overpressure is explosively release, and finally 3) a reinflation as fresh magma flows into the sill and degases. This cycle is attributed to the development of a brittle plug at the top of the magma column and effective sealing of degassing pathways due to degassing crystallization as water exsolves and the magma is undercooled. Data from apparent tilt, SO_2 concentrations and infrasound records support this interpretation. The VLP source location west of the summit may indicate migration of the magma pathway, which has hazard implications.

3.1. Introduction

Fuego volcano is a 3800 m stratovolcano and the southernmost expression of the north-south trending Fuego – Acatenango massif that contains at least 5 known eruptive centers. It is located in the western highlands of Guatemala and is situated within the second of eight segments of the Central American volcanic front [*Carr*, 2002]. Fuego has produced more than 60 historical subplinian eruptions which punctuate months to years of low-level open-vent activity. The most recent subplinian eruptions (VEI 4) occurred in October 1974 and produced intense ash fall, pyroclastic flows, lahars and lava flows that greatly impacted local populations [*Rose at al.*, 1978]. The Fuego – Acatenango complex has produced at least two large (2.4 and 9 km^3) debris avalanches in prehistoric time and studies suggest that a partial edifice collapse to the south remains a significant hazard [*Vallence et al.*, 2002; *Vallence et al.*, 1995]. Since 1974, Fuego has erupted high-Al basalts and basaltic andesites (~51% SiO_2) that are relatively volatile-rich (2.1 – 6.1 wt% H_2O) [*Roggensack*, 2001; *Sisson and Layne*, 1993].

The most recent period of activity began on 21 May 1999 with a VEI 2 eruption that transitioned into open-vent activity interspersed with infrequent paroxysmal eruptions (VEI 2 – 3) that last for 1 – 2 days and occur approximately annually [*Smithsonian Institute*, 1999]. The open vent activity is characterized by continuous background degassing from the summit crater (~340 t d^{-1} SO_2), frequent explosions and intermittent lava effusion [*Lyons et al.*, 2010; *Rodriguez et al.*, 2004]. Seismicity accompanying open vent activity includes harmonic and non-harmonic tremor, explosion earthquakes, long period (LP) earthquakes, and very-long-period (VLP) earthquakes

[*Smithsonian Institution*, 1999]. Variations in the style of open-vent activity and explosion characteristics were described in detail by *Lyons et al.* [2010], but no detailed characterization of the seismic source mechanism of the explosions has been performed. Infrasound recordings of explosions at Fuego in January 2003 showed an impulsive onset and extended coda that was speculated to be caused by initial pressure release and then progressive fragmentation of a pressurized foam in the conduit [*Johnson et al.,* 2004]. Six months of continuous infrasound recorded in 2007 highlighted the waveform and amplitude variability of infrasound generated during explosive activity, but the limited number of sensors and relatively large, 7 km distance from the source prohibited further interpretation of source mechanisms *Lyons et al.* [2010].

The seismic and acoustic arrays that we deployed in January 2008 and 2009 recorded the first broadband seismic and infrasound data capable of a quantitative analysis of the source mechanism of the explosions at Fuego. The explosions we recorded in 2008 had emergent onsets, low amplitudes in the seismic and infrasound, long durations (30 – 90 s) and produced ash-rich plumes but no incandescent ejecta. In 2009 the characteristics of the explosions changed significantly; they had impulsive onsets and high amplitude seismic and acoustic signals. The duration of the explosions was shorter than in 2008 and substantial incandescent tephra and bombs accompanied the blasts. Large explosions were interspersed with more frequent and weaker emissions of gas and ash. Local observers from the Instituto Nacional de Sismología, Vulcanología, Meteorología e Hidrología (INSIVUMEH) reported cessation of a small active lava flow 1 week prior to our experiment and no lava effusion was observed during the course of

the experiment. Images of SO_2 emissions taken with an ultraviolet camera located 1 km north of the summit show two active degassing sources, one near the center of the summit crater and another located near the western edge of the crater [*Nadeau et al.,* 2011]. The central vent sourced all the major explosions during our experiment, while the western vent produced mainly passive degassing and some weak gas and ash emissions.

Volcanic tremor and LP events dominate the seismicity throughout the experiment with the numerous explosive events overprinting what were often hours of continuous harmonic and non-harmonic tremor. Explosions frequently triggered minutes of high-amplitude tremor but other explosions would disrupt tremor, only to have the tremor return at the same frequency and amplitude tens of seconds after the explosion. The most striking change in the seismic and infrasound record between 2008 and 2009 is the regular appearance of very-long-period (VLP) signals coincident with the explosions, which are not common in the 2008 data. Non-explosive VLP signals were recorded infrequently during the 2009 experiment but are outside the scope of this paper. VLP signals were either not produced or not recorded by our network for the more frequent small explosions and gas and ash exhalations, so the focus of this study is the most energetic explosions.

VLP seismic signals are being recorded more frequently at active volcanoes all over the world as broadband sensors become more resilient and affordable. The VLP wavelengths are typically tens to hundreds of kilometers, which aids in analysis because the waveforms are not susceptible to modification by the small-scale velocity heterogeneities that exist in volcanic piles. VLP events accompanying volcanic

explosions have been studied at Stromboli [*Chouet et al.*, 2003; *Chouet et al.*, 2008], Mount Erebus [*Aster et al.*, 2003; *Rowe et al.*, 1998], Asama [*Ohminato et al.*, 2006], Popocatépetl [*Arciniega-Ceballos et al.*, 1999; *Chouet et al.*, 2005] and Kilauea [*Chouet et al.*, 2010] in order to elucidate seismic source mechanisms and infer source volumes and conduit geometries. The proposed mechanisms for producing explosive VLP signals include: gas slug transport through variable conduit geometries (Stromboli), rapid gas slug expansion and burst driving conduit oscillations (Mount Erebus and Kilauea), diffusive-elastic conduit pressurization (Popocatépetl) and viscous drag of rapidly ascending magma on conduit walls (Asama).

In this paper, we use a modified version of the linear inversion method of *Ohminato et al.* [1998] to model the source mechanism of VLP seismic waveforms recorded during explosive eruptions in January 2009. We begin with a description of the broadband seismic and infrasound network and the data, followed by the waveform inversion and forward modeling methodology. Finally, we provide an interpretation of the results and discuss the source dynamics of explosions at Fuego.

3.2. Broadband Seismic and Infrasound Network

Our seismic data were recorded on a network of 10 three-component broadband seismometers, 6 on loan from the Incorporated Research Institutions for Seismology Program for Array Seismic Studies of the Continental Lithosphere instrument center and 4 from Michigan Tech (Figure 3.1). Infrasound data were recorded on eight broadband microphones co-located in pairs with seismometers at stations F900, F9NW, F9NE and

F9B. The network configuration was designed to provide maximum azimuthal coverage and spacing from the summit to allow location of shallow events. However, the steep topography, deep ravines and eruptive activity significantly limited our access to the southern half of the volcano. All sites required reconnaissance, installation and servicing by foot.

Six of the sites were equipped with Güralp CMG 40T sensors (0.02 – 30 s) and four sites featured Güralp 3 ESPC sensors (0.02 – 60 s). The infrasound sensors were All Sensors differential pressure transducers (0.001 – 50 s) with a ± 250 Pa dynamic range. Data were recorded on 10 Reftek 130 digitizers operating in continuous mode at 100 samples per second and equipped with Global Positioning Systems (GPS) timing. Station locations were determined with handheld GPS units to within 2 – 5 m. The horizontal components of all the sensors were oriented in the field with compass measurements.

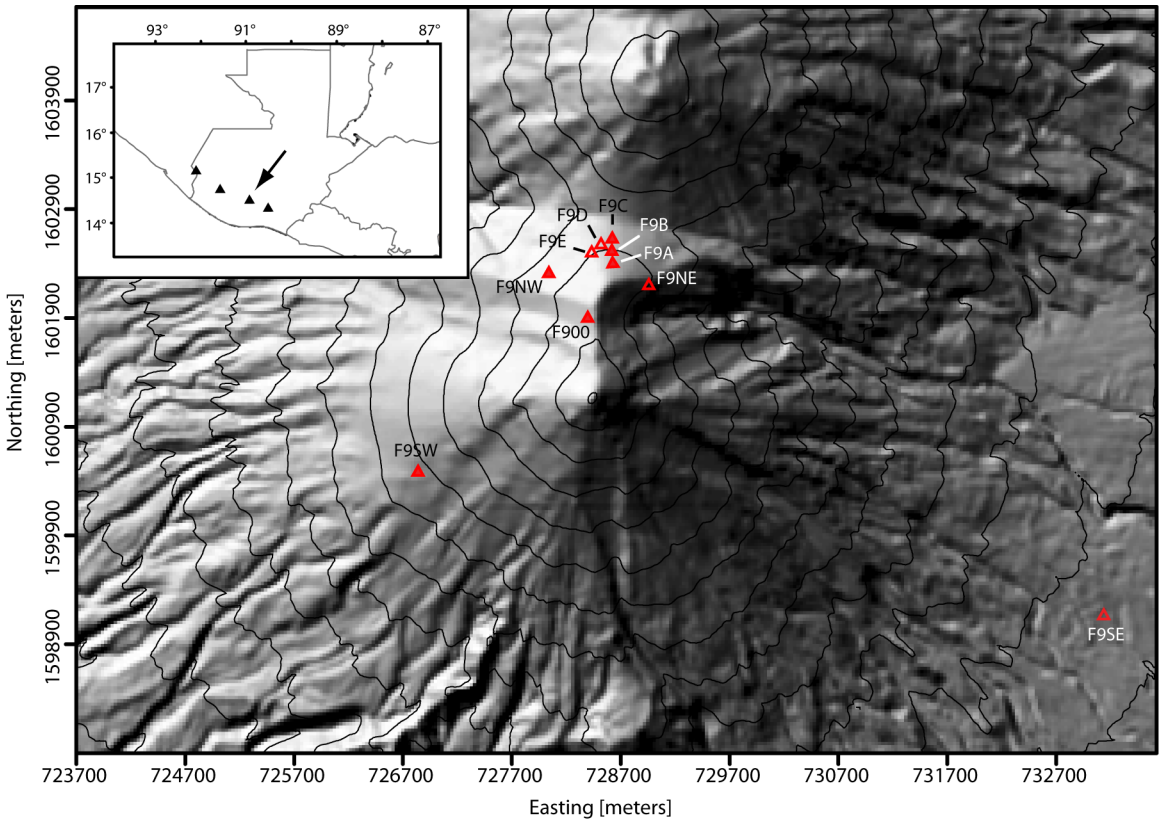

Figure 3.1. Hillshade digital elevation model (DEM) of Fuego volcano with 200 m contour interval. Triangles show seismic stations deployed in 2009. Filled symbols are stations used in the waveform inversion; open symbols were not used in the inversion. Inset map shows the location of the Fuego – Acatenango complex in the chain of active volcanoes in Guatemala.

While our experiment ran for 19 days from 8 January through 26 January, the difficulty of access and the threat of vandalism or theft prohibited deployment of solar panels at some sites so continuous operation of all 10 stations was restricted to 19 January through 21 January. Station F9SE was installed 5 km from the summit of Fuego due to poor access and is not included in the analysis because VLP signals were not clearly recorded at this distance. Station F9NE was vandalized early in the experiment and the seismometer appears to have been knocked out of level, so these data are also not included in the VLP analysis. INSIVUMEH operates a single vertical component 1 Hz

seismometer 6 km to the southeast of the summit that telemeters continuous data to Guatemala City for monitoring but we did not use this data because the sensor did not record the VLP signals.

3.3. VLP Data

VLP signals accompanying explosions were recorded most clearly on the closest stations, with amplitude quickly decaying with increasing station distance from the summit. Strong explosions were always accompanied by broadband seismic and infrasound energy as well as VLP energy (Figure 3.2). The VLP component of the signal is extracted by deconvolving the instrument response and then filtering with a two-pole, zero-phase-shift Butterworth band-pass filter with corners at 30 and 10 s. We chose this band to include as much VLP signal without introducing additional noise between the low corner of our 30 s instruments and the oceanic microseism. Figure 3.3 demonstrates the effect of varying the filter corners on a representative signal from an explosion on 19 January 2009. The low corner is fixed at the low corner of the different sensors, 30 s (Figure 3.3a) and 60 s (Figure 3.3b), and the upper corner varies from 18 to 5 s. The spectral peaks for the 30 s sensor show energy broadly peaked from 14 – 21 s, as does the north channel of the 60 s instrument. The east and vertical channels of the 60 s instrument have a slightly lower peak at 27 s. Both sets of spectra show that a 10 s upper corner captures most of the VLP energy without introducing significant microseism noise. The spectra from the 60 s sensor demonstrate that the VLP signal is mostly above 30 s, although the 10 – 30 s band misses some of the VLP signal (Figure 3.3b).

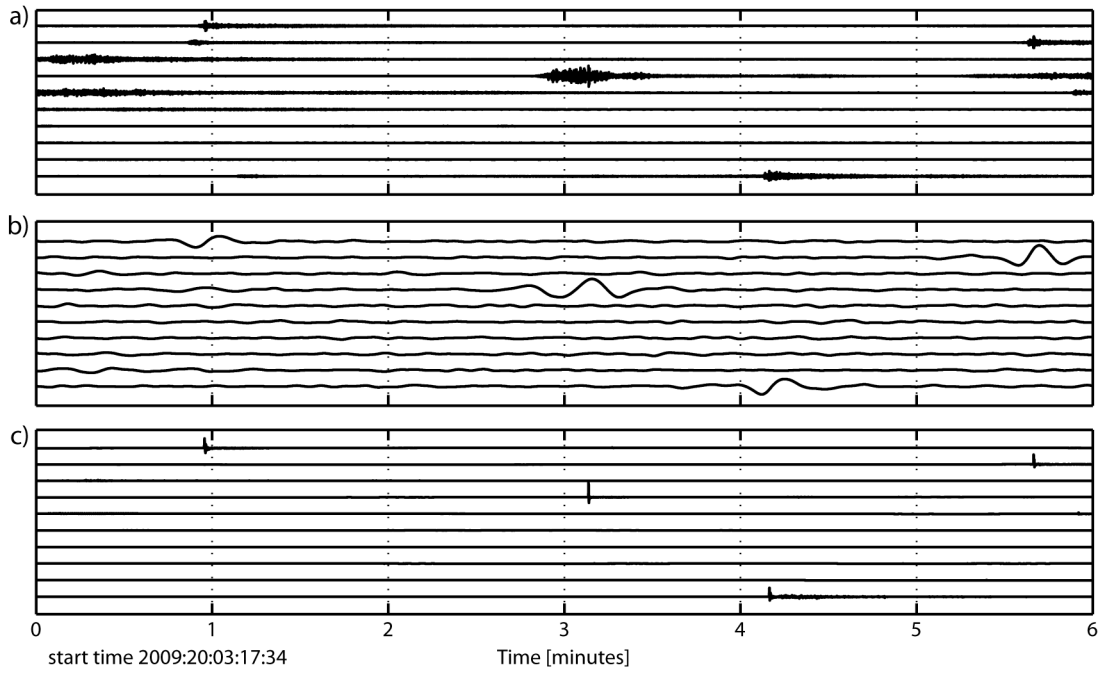

Figure 3.2. A 60 minute plot of short-period (SP) seismic (a), VLP seismic (b) and SP infrasound (c) data. The SP data is filtered from 0.5 – 10 Hz and the VLP data is filtered from 10 – 60 s, using a zero-phase-shift, two-pole Butterworth filter. This was a particularly active hour in which there were four large explosions that produced clear VLP signals.

Explosions have impulsive onsets and higher frequency energy dominates the broadband signal (Figure 3.4). The highest energy portion of the broadband portion of the signal lasts for 10 – 15 s, but the VLP signal lasts at least 30 s. The VLP waveforms across our network are distinctly different between the horizontal and vertical channels, as illustrated by a representative event recorded on 21 January in Figure 3.4b. At stations north of the vent, horizontal channels display a clear compression-dilatation-compression sequence, while the vertical channels show a dilatation-compression-dilatation sequence. At F9SW, the horizontal channels have the opposite polarity, but the vertical signal is similar to the rest of the network.

The VLP waveforms remain remarkably similar over the 19 days of recording as shown by a plot of all the large explosions recorded at our longest running station, F900 in Figure 3.5. VLP waveforms were identified automatically by assigning the first recorded explosive VLP as the master event and then cross-correlating that event with the entire database in each channel. The cross-correlation was performed with a 60 s window moving in 1 s steps over the signal band-pass filtered from 30 – 10 s. A summed correlation coefficient across the three channels of 2.55 provided a preliminary VLP database, but also contained signals not associated with explosions. We used the infrasound record to limit the VLP database to only waveforms associated with infrasound transients of greater than 100 Pa. The resulting 53 VLP waveforms are aligned according to the maximum cross-correlation value in the vertical channel. Figure 3.5 clearly shows the dilatation-compression-dilatation sequence in the vertical channel and the compression-dilatation-compression sequence in the horizontal channels. The similarity of the VLP waveforms suggests a repetitive, stable source mechanism.

Particle motion plots may provide additional evidence that the VLP source was relatively stable over the course of the experiment. Figure 3.6 shows particle motions for the stacked VLP events at the closest station sites in the network. The rectilinear traces of stacked particle motions may indicate that the source was invariant for the explosions. Particle motion plots are also useful for approximating epicentral source locations, and Figure 3.6 indicates that the VLP source is located west of the summit crater. However, studies have shown that topography can greatly influence waveforms, so source locations cannot be determined by particle motions alone [*Neuberg and Pointer*, 2000].

3.4. Data Analysis and Results

3.4.1. Waveform Inversion Method

We perform a full-waveform inversion of the largest amplitude VLP event recorded across our network using a method similar to *Chouet et al.* [1995]. The displacement field for a seismic point-source is described by the representation theorem, and can be written as [*Chouet et al.*, 2003; *Waite et al.*, 2008]

$$u_n(\vec{r},t) = F_p(t) * G_{np}(\vec{r},t) + M_{pq}(t) * G_{np,q}(\vec{r},t), \quad p,q = x,y,z \tag{3.1}$$

where $u_n(\vec{r},t)$ is the n-component of the displacement at time t and receiver position $\vec{r}$, $F_p(t)$ is the time history of the force applied in the p-direction, $M_{pq}(t)$ is the time history of the pq component of the moment tensor and $G_{np}(\vec{r},t)$ is the tensor of Green functions relating the n-component of seismic displacement to the p-component of impulsive force at the source position. Inversion of our data following equation (1) is done following *Ohminato et al.* [1998] and *Chouet et al.* [2003], but in the frequency domain. The source location is fixed and the source-time functions for each moment and force component are found by minimizing the square of the residual error between the data and the calculated synthetics.

3.4.2. Calculation of Green Functions

We generate synthetic Green functions with the three-dimensional (3D) finite-difference method of *Ohminato and Chouet* [1997] using a model that includes the 3D

topography of Fuego. A homogenous velocity model is assumed because no velocity models exist for Fuego and because in the 10 – 30 s band wavelengths are 10s of km so should not be greatly influenced by small scale velocity heterogeneities. Our model compressional wave velocity is 3.5 km/s, shear wave velocity is 2 km/s and density is 2650 kg/m^3. The Green functions are convolved with a cosine smoothing function in order to ensure inversion stability:

$$S_t = \begin{cases} \frac{1}{2}\left[1 - \cos\left(\frac{2\pi t}{t_p}\right)\right], & 0 \le t \le t_p \\ 0, & t > t_p \end{cases} \tag{3.2}$$

where t_p = 0.5 s. A t_p of 0.5 s yields frequencies from 0 – 4 Hz in the cosine smoothing function.

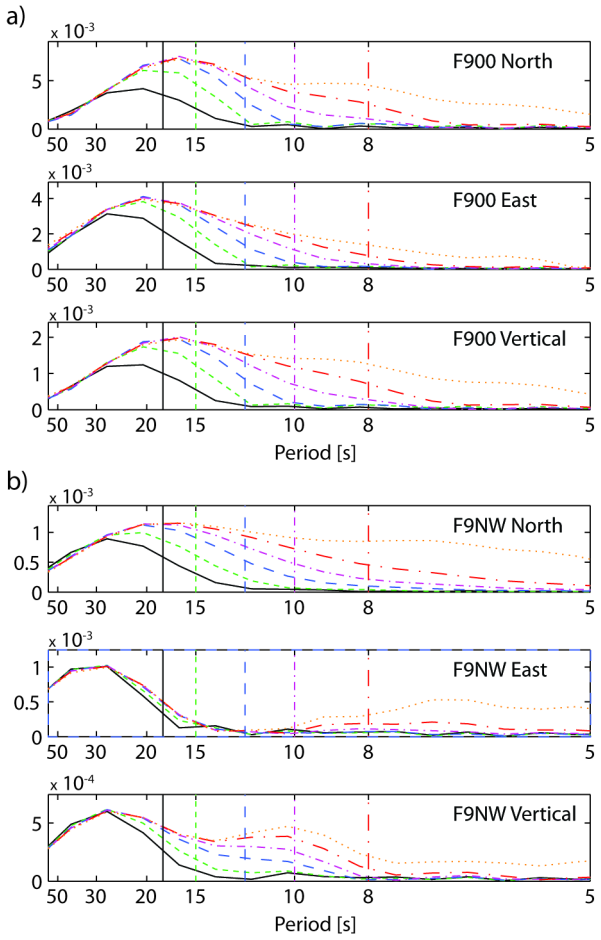

Figure 3.3. Power spectra of an explosion VLP showing the effect of varying the upper and lower corner of the bandpass. The low corner is set at 30 s (a) and 60 s (b) based on the low corner of the instrument and the upper corner varies: 18, 15, 12, 10, 8 and 5 s. The color, line-style and location of the vertical bars correspond to the upper corner for that spectral trace. A broad peak in VLP energy exists from 14 s to 21 s in the 30 s instrument (a) and the north channel of the 60 s instrument (b). VLP energy in the east and vertical channels of the 60 s instrument peaks at slightly longer periods, but still above 30 s, showing that our 10 – 30 s bandpass captures most of the VLP energy without introducing significant microseism noise.

Our model space is centered at the summit of Fuego and has dimensions of 11.72 km east – west, 8.96 km north – south and 6 km in the vertical, yielding a 294 × 225 × 151 node mesh at 40 m spacing. The 40 m grid spacing of the model ensures that the minimum number of 25 grid nodes per wavelength established by *Ohminato and Chouet*

[1997] is satisfied but that the model space is sufficiently compact to allow timely calculations of Green functions.

The best-fit source location is determined by performing a grid search over an initial source volume 1080 m by 360 m by 600 m in the east, north and vertical directions, respectively, extending downward from the surface topography. Figure 3.6 indicates the lateral extent of the source volume grid which is shifted west to initially focus on the area indicated by the particle motion plots. A coarse spacing of 120 m for the initial search indicates a best fits in a region 120 – 360 m west, 0 – 120 m south and 0 – 480 m below the summit. We then search over a volume 240 m × 240 m × 480 m centered over the initial best fit region at a 40 m grid spacing to find a best fit point source. A total of 1,090 source locations are investigated to determine the best VLP source location.

3.4.3. Evaluation of Results

The inversions for a best-fit source location consider three possible source mechanisms: 1) three single-force components, 2) six moment components and 3) six moment components and three single-force components. Choice of the optimal mechanism is based on the squared error, the relevance of the free parameters used in the model and the physical plausibility of the resulting source mechanism. We use two expressions of squared error to compare the synthetic results and data in the time domain [*Chouet el al*., 2003]

$$E_1 = \frac{\sum_{n=1}^{N_t}\sum_{p=1}^{N_s} (u_n^0(p\Delta t) - u_n^s(p\Delta t))^2}{\sum_{n=1}^{N_t}\sum_{p=1}^{N_s} (u_n^0(p\Delta t))^2} \times 100 \tag{3.3}$$

and

$$E_2 = \frac{1}{N_r}\sum_{n=1}^{N_r}\left[\frac{\sum_{1}^{3}\sum_{p=1}^{N_r}(u_n^0(p\Delta t) - u_n^s(p\Delta t))^2}{\sum_{1}^{3}\sum_{p=1}^{N_r}(u_n^0(p\Delta t))^2}\right] \times 100 \tag{3.4}$$

where $u_n^0(p\Delta t)$ is the pth sample of the nth data trace, $u_n^s(p\Delta t)$ is the pth sample of the nth synthetic trace, N_t is the number of data traces, N_s is the number of samples in each trace and N_r is the number of three-component receivers. In equation (4), larger amplitude signals from stations closer to the source dominate the error, and the error will remain low despite potentially large misfits between the data and synthetics for low-amplitude signals if good matches exist between the synthetics and data at high amplitude stations. In equation (5), the error is normalized by station so that all stations contribute equally to the error. We report both values but prefer to focus on the E_1 results due to the much larger signal to noise ratios for stations closer to the source. While this creates a bias towards the stations nearest the summit, we think it is justified due to the sparse nature of our network and reliance on distant stations with low amplitude for azimuthal coverage.

The influence of the number of free parameters in each source model is assessed by calculating Akaike's information criterion (AIC) [*Akaike*, 1974] defined as

$$AIC = N_t N_s \ln E + 2 N_m N_f \tag{3.5}$$

where E is the squared error from equations (4) or (5), N_m is the number of source mechanisms and N_f is the number of frequencies in the passband of interest. The best fits are generally with nine components (6 moment and 3 single forces), and the use of more free parameters is considered justified when both the squared error and AIC are reduced. However, the final test of the validity of a solution rests on whether or not it has physical relevance. The moment tensor solution must have consistent waveforms among the components in order to produce an interpretation of the source mechanism that is physically plausible.

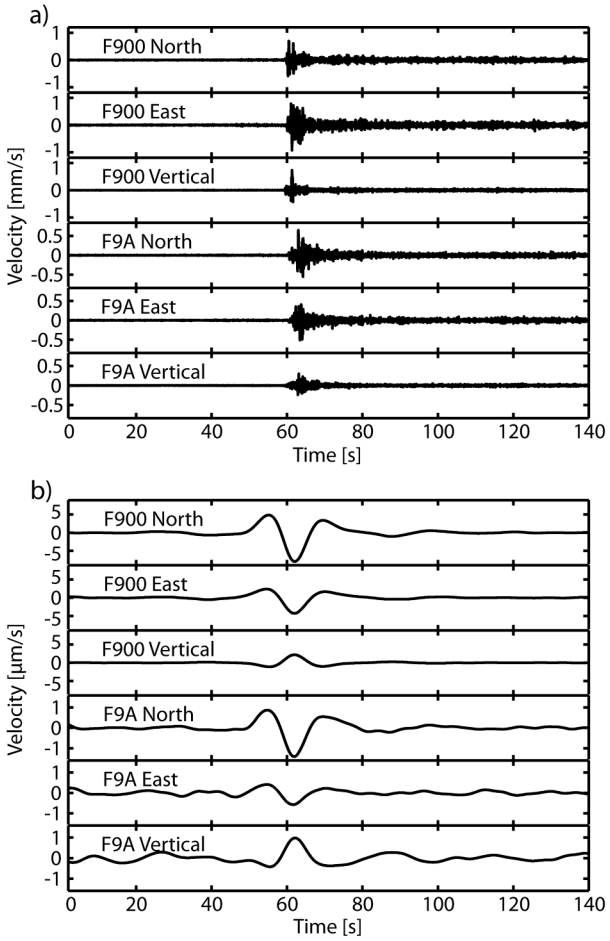

3.4. Broadband (a) and VLP (b) seismograms of a representative explosion recorded at stations F900 and F9A. VLP waveforms have consistent shapes across the network. The VLP waveforms recorded on the vertical channels have dilatation-compression-dilatation motion, while the waveforms recorded on the horizontal channels show compression-dilation-compression motion.

3.4.4 Results

We modeled the explosion VLP of a representative event from 19 January 2009 because the event was clearly recorded on the closest stations and the signal was recorded on all stations except F9SE. Table 1 shows the inversion results with the minimum residual errors for three single forces, six moment components and three single-forces plus six moment components. The three single-force synthetics do not fit the data well

and have source-time functions that are physically unrealistic so they are eliminated from further consideration. The nine-component inversion has residual errors and AIC values that are lightly lower than the six moment tensor only model, and the best-fit source locations overlap. However, the source-time functions of the nine-component model can not be interpreted in terms of a reasonable physical model (discussed below); therefore, we focus our results and discussion on the six moment tensor component model. Because we have relatively few data (17 channels) it may be too optimistic to expect to be able to fit a model with nine free parameters. As discussed by *Dawson et al.* [2011], the single-force components can be difficult to resolve in a sparse network, especially when the signal-to-noise ratio is not quite large (>20).

Table 3.1. VLP Inversion Results

Inverted Parameters	E1	E2	AIC(E_1)	AIC(E_2)
3 forces	0.316	1.924	-80143	45678
6 moments	0.020	0.215	-272310	-108580
3 forces + 6 moment	0.008	0.084	-335240	-172380
1 crack[a]	0.210	0.391	-108610	-65363
1 pipe[a]	0.252	0.496	-95880	-48714
1 crack + 1 pipe	0.038	0.345	-227060	-73005
2 pipes[a]	0.096	0.548	-163080	-41761
2 cracks	0.050	0.422	-207950	-59930

[a]Errors are calculated using 17 channels with equations 4 and 5. The eigenstatistics for these model geometries do not match the results from the free inversion.

The best-fit source location for a model with six moment components lies west of the summit crater at 3480 m elevation (Figure 3.7). The source position is 300 m west and 300 m below the active summit crater. The minimum residual errors for this best-fit source location, calculated with 17 channels, are $E_1 = 0.02$ and $E_2 = 0.21$ (Table 1). We

estimate source location error by taking horizontal and vertical slices of the source centroid and contouring residual errors in 1% increments above the E_1 minimum error (Figure 3.7). The 5% error contour gives an uncertainty of 80 m the east-west direction, 120 m in the north-south direction and 50 m in the vertical.

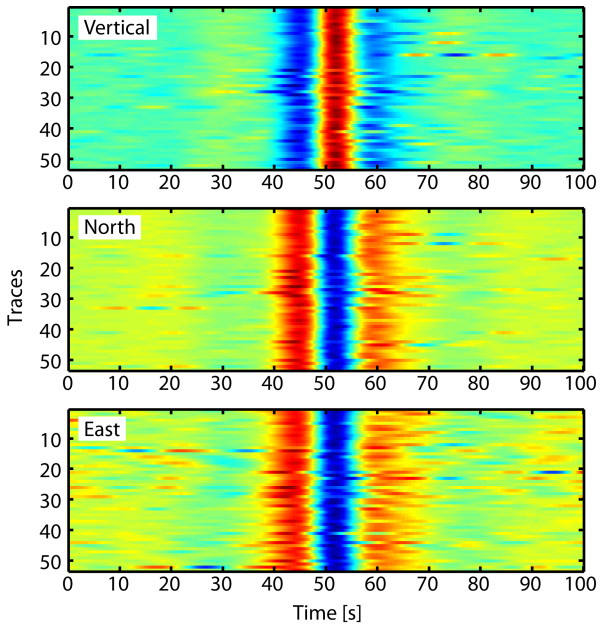

Figure 3.5. Station F900, our most reliable station, operated for 19 days and recorded 53 explosion VLPs, which we align based on the maximum cross-correlation values in the vertical (a) channel; events with cross-correlation coefficients of 0.85 and higher are plotted. The waveforms are highly similar over the course of the experiment, suggesting a stable and repetitive source. Note the difference in the motion of the vertical and horizontal channels.

The data (black traces) and synthetic (red traces) waveforms for the inversion at the best-fit point-source location for the six stations used in the inversion are shown in Figure 3.8. Stations F9SE, F9NE, F9D and F9E were not used in the inversion because the VLP signals were absent, had low signal-to-noise, or, in the case of F9NE, the station had been damaged. The east component of station F9B was not functioning and was not

used in the inversion. The synthetics for most channels fit the data well, although a poorer fit occurs on the vertical and north channels of the farthest station, F9SW.

Figure 3.9 depicts the source-time functions for the mechanism containing six moment components plus three forces (red traces) and the six moment components only (black traces). The volumetric components dominate the moment-tensor solutions for the six-component model and are all in phase. The amplitude of the vertical dipole component, M_{zz}, is nearly twice the amplitude of the east-west, M_{xx}, or the north-south, M_{yy}, components. The non-dipole components have low amplitudes relative to the volumetric components and M_{yz} and M_{xz} are out of phase with the dipole components. The shape of the moment tensor solution for the nine-component model does not match that of the six component only model (Figure 3.9). Large contributions from M_{zz} and M_{yz}, dominate the moment tensor of the nine component mechanism. The single forces are low amplitude to the nine component source-time function, and F_y is the only coherent component among the single forces, which are otherwise appear to be dominated by noise. The ratio of peak-to-peak amplitudes of M_{zz}/F_z = 71,046 m and M_{yy}/F_y = 25,356 m. Based on previous work, which found that the moment and single force components contribute to the solution equally when M_{xx}/F_x on the order of 200 – 2000 m, we infer that the single forces here are not significant [*Waite et al.*, 2008]. In addition, the incoherence in the waveforms and small amplitude, noisy single force time series result in a source-time function that does not relate to a physically plausible source model.

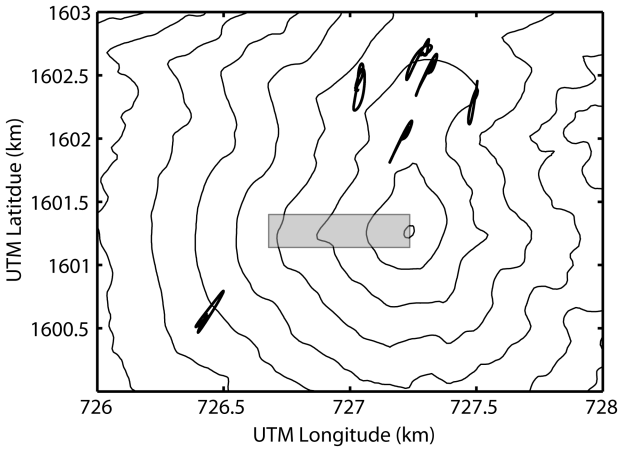

Figure 3.6. Horizontal particle velocities, normalized by station, for stacks of VLP waveforms plotted on a station map. Particle motions are rectilinear and point to an area west of the summit vent. The gray box indicates the horizontal extent of the region of potential point source locations used in the waveform inversion.

The source-time functions derived from the moment-only solution are dominated by in-phase dipole components, with small contributions from off-diagonal components, indicating a source with volume change. We perform a detailed examination of this moment tensor through a point-by-point eigenvector analysis of the source-time function. This method highlights the time-dependant properties of the eigenvectors and assesses the stability of the source mechanism over the entire source-time function. Figure 3.10 shows the eigenvector statistics sampled every 0.05 s over the source time history of the moment components in Figure 3.9 (black traces). The eigenvector orientation is defined by the azimuth, $\emptyset$, measured clockwise from north and the plunge, θ, measured from vertical. Figures 10a and 10b show rose diagrams of the dominant, intermediate and minimum eigenvector sorted into 5° bins. Histograms of the ratio of the smallest to dominant and intermediate to dominant eigenvalues are shown in Figures 10c and 10d, respectively. The weighted arithmetic mean, $\bar{x}$, of the ratios, with the maximum

eigenvalue normalized to 2, are [0.48:0.75:2.00]. The narrow distribution of eigenvectors in Figure 3.10 is evidence of the stability of the source mechanism through time, and the standard deviations show that the minimum and intermediate are significantly different. The maximum eigenvector is dipping 30° to the southwest, which, for a crack source, suggests the VLP source has a similar orientation.

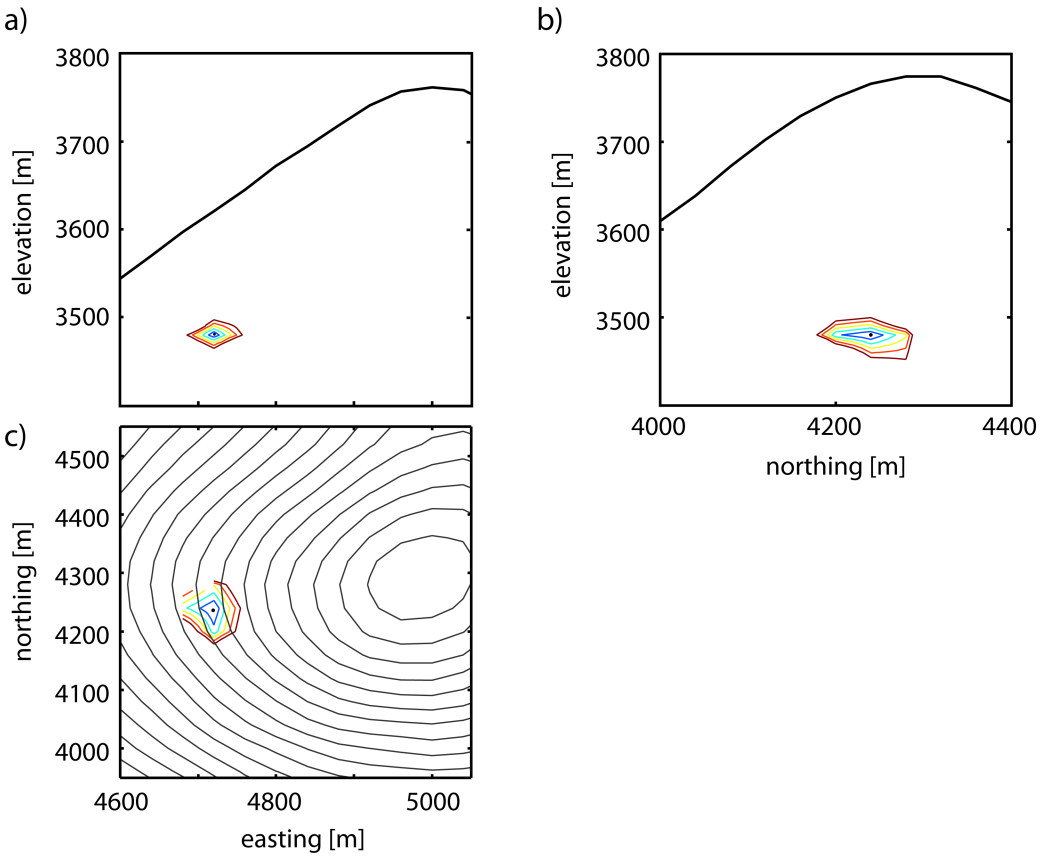

Figure 3.7. Location of the point source (black dot) that produces the minimum residual error using 6 moment tensor components for the 19 January 2009 explosion VLP. East-west (a) and north-south (b) cross-sections through the point source, including surface topography of Fuego. Map view (c) of the point source including the summit region of Fuego (20 m contours). Each colored line around the best fit point contours E_1 in 1% increments. The best-fit location is 300 m west of the summit crater.

We assess the results of the eigenvector decomposition by comparing our calculated eigenvalue ratios with theoretical ratios of potential source geometries, including cracks, pipes and combinations thereof [*Chouet et al*., 2005]. A tensile crack can be represented using the three components of the diagonalized moment tensor, where the dominant dipole is oriented normal to the crack plane. The amplitudes of the dipole components are $\lambda\Delta V$, $\lambda\Delta V$ and $(\lambda + 2\mu)\Delta V$, where λ and μ are the Lamé parameters of the host rock and ΔV is the volume change associated with opening and closing of the crack [*Waite et al.*, 2008]. The moment tensor for a hot, magma-filled crack would have dipole ratios of [1:1:2], assuming a Poisson ratio $v = 1/3$ ($\lambda = 2\mu$) [*Chouet et al.*, 2003; *Chouet et al.*, 2005; *Chouet et al.*, 2010; *Dawson et al.*, 2011; *Ohminato et al.*, 1998; *Waite et al.*, 2008]. We can also represent the dipole components of a volcanic pipe, where $\emptyset$ and θ describe the orientation of the pipe axis. Assuming $v = 1/3$, the ratios of the principle axes are [1:1.5:1.5], where the orientation of the pipe axis is described by the minimum eigenvector [*Aki and Richards*, 1980; *Chouet*, 1996a]. While neither the single crack nor the single pipe ratios match our data reasonably well, we can construct a number of composite sources that match our results closely. For example, the combination of two cracks with one contributing 1/3 of the energy in the opposite polarity as the other, is obtained by the vector operation [1:1:2] - (1/3)[2:1:1] = [0.33:0.67:1.67], which yields [0.40:0.80:2.00] after normalizing. We use this result to guide the forward modeling of source geometries detailed in the following section.

3.4.5 Source Reconstruction

We conduct a systematic search for the best source model geometry using reconstructed moment tensors for a single crack, a single pipe, two intersecting pipes, two intersecting cracks and a pipe intersecting a crack. The crack and pipe moment tensors are generated using equations (15) and (16) of *Chouet* [1996a], assuming $\nu = 1/3$ ($\lambda = 2\mu$). Despite having some information about the source geometry from the eigenvector statistics, we perform a grid search over all the possible crack/pipe combinations in order to include geometries that could provide a better result. We calculate Green functions for crack, pipe and composite mechanisms over all possible orientations, initially varying $\emptyset$ and θ in 15° intervals. Once the minimum residual orientation is identified in the course search, $\emptyset$ and θ are reduced to 5° intervals to identify the orientations that yield the lowest residuals. Crack orientations are described by the pole to the crack plane (i.e., the maximum eigenvector) where azimuth, $\emptyset$, is measured counterclockwise from east. For clarity we will refer to the dip of the crack plane, θ, rather than the plunge of the pole to the crack plane. Pipe axis azimuth, $\emptyset$, is measured clockwise from north in the direction of plunge, θ, from vertical (0°).

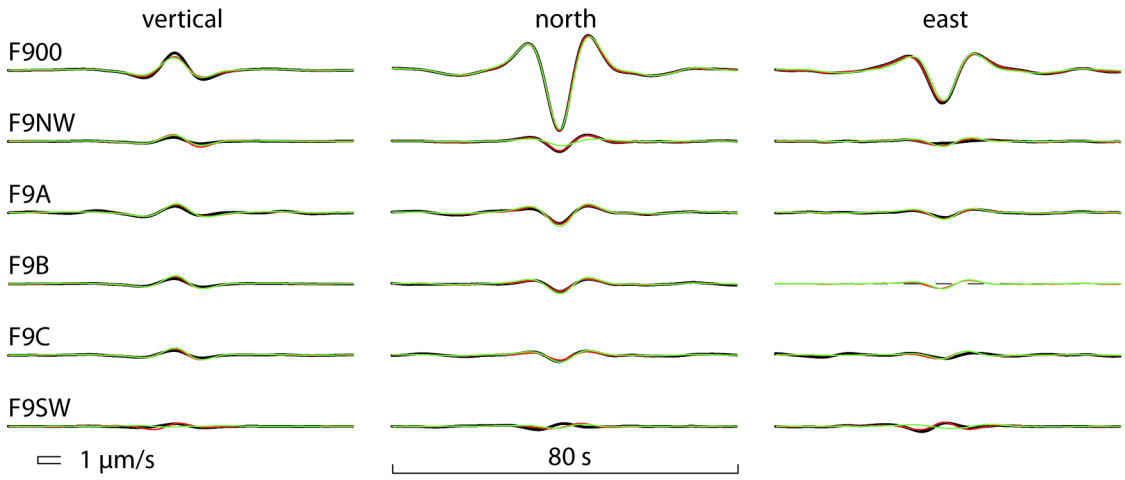

Figure 3.8. Velocity data for the 19 January 2009 explosion VLP (black traces) used in the inversion and synthetic waveforms (red traces) generated using the minimum residual error (E_1) location for the six moment tensor source. Synthetic waveforms for a two-crack model (θ_1 = 35°, $\varnothing_1$ = 225°, θ_2 = 65° and $\varnothing_2$ = 35°) are also shown (green traces). The two-crack model fits most stations well, with the exception of the furthest station, F9SW, and the horizontal components of F9NW.

The best fitting single crack has an orientation θ = 30° and $\varnothing$ = 75° and residual errors of E_1 = 0.21 and E_2 = 0.39 (Table 1). The best fitting pipe has an orientation of θ = 60° and $\varnothing$ = 315° and residual errors of E_1 = 0.25 and E_2 = 0.50 (Table 1). Both single component models have residual errors much higher than the six moment component free inversion and AIC values that indicate that a greater number of free parameters may be necessary to better fit the data (Table 1). These results combined with the eigenvector statistics allow us to discount either a single crack or single pipe as a likely source mechanism.

The best fitting model combining two pipes has residual errors of E_1 = 0.096 and E_2 = 0.548 (Table 1) by the combination of one pipe plunging 30° to the west and the other plunging 30° to the northeast. The errors for this model and the AIC value for E_1 are lower than the single component models, but still substantially higher than the six

moment component free inversion. The shape of the reconstructed source-time functions and the eigenvector statistics are both substantially different than the six component free inversion, suggesting that the combination of two pipes is not a realistic source geometry.

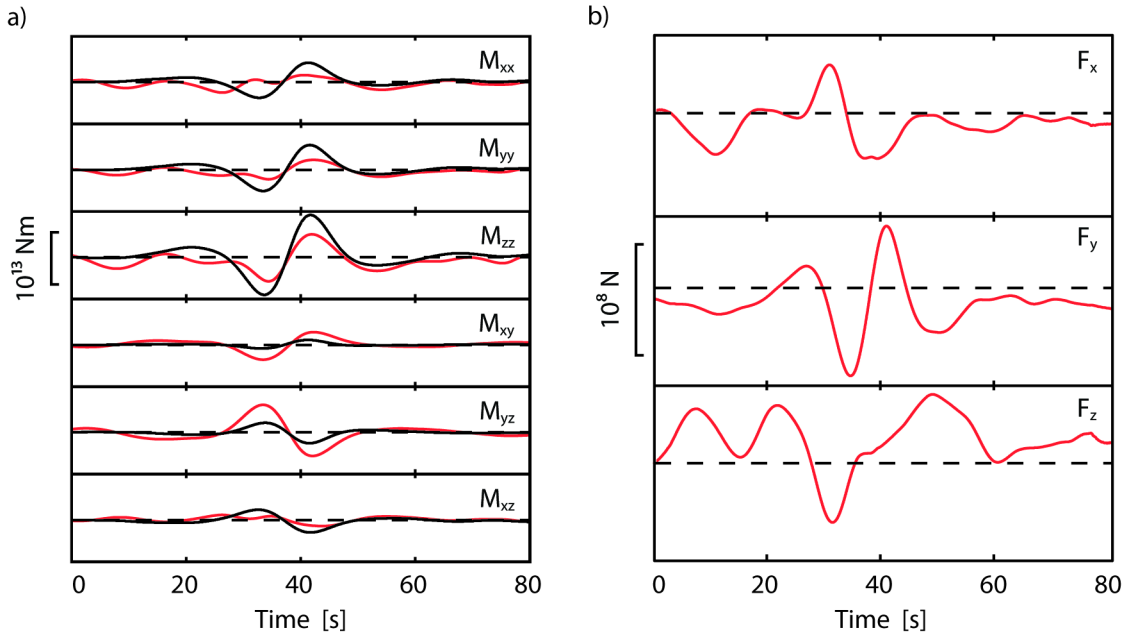

Figure 3.9. The source-time function of the 19 January 2009 explosion VLP for the six moment tensor components only (black) solution. The six moment component only solution (a) is dominated by the three dipole components, which are in phase indicating a volumetric source. The nine component solution, including the single forces (b) is shown in red for comparison and cannot be related to a reasonable physical mechanism.

The best fitting two-crack model has residual errors of $E_1 = 0.050$ and $E_2 = 0.422$ (Table 1) and consists of one crack dipping to the southwest ($\theta = 35°$ and $\varnothing = 225°$) and a crack dipping steeply toward to the northeast ($\theta = 65°$ and $\varnothing = 35°$). The AIC values for E_1 and the E_1 error are substantially lower than the single crack model and closer to the values for the six moment component free inversion (Table 1). The eigenvector statistics calculated from the two-crack reconstructed moment tensor source-time

functions are [0.65:0.88:2.00], which are close to the statistics for the six-moment free inversion. The waveform fit, the shape of the reconstructed moment tensor source-time functions and the eigenvector statistics suggest that the two crack model is a possible model for the VLP source.

Similar results are derived for the combination of a crack and a pipe. The residual errors are slightly lower than the two-crack model, $E_1 = 0.038$ and $E_2 = 0.345$ (Table 1), for a crack dipping to the southwest ($\theta = 30°$ and $\varnothing = 220°$) and a pipe plunging steeply to the south ($\theta = 75°$ and $\varnothing = 270°$). The eigenvector statistics for the single crack and pipe are [0.59:0.86:2.00], similar to the two-crack model and close to those of the six-moment free inversion. The shapes of the reconstructed source-time functions also match the six-moment free inversion, making the single crack and single pipe model another potentially viable source model for the VLP signal.

We now have two prospective conduit geometries suggested by the seismic inversion and forward modeling. In both cases, a crack dipping to the southwest at 30 – 35° dominates the reconstructed source-time function. The dominant crack accounts for 82% of the volume change in the two-crack model and 72% of the volume change in the combined crack-pipe model. In order to distinguish which model is a more likely candidate, we consider the geological plausibility of each model. The best-fit source location from the free inversion lies 300 m west and 300 m below the summit crater, which, when considering the steep topography of the upper cone of Fuego, places the source centroid 150 m below the surface. This location limits the geologically possible geometric interpretations if we stipulate that the projection of one of the geometric

components of either model must intersect the surface within the surface crater, the source of all observed explosive activity during the experiment. The mathematical representation of these models does not distinguish intersecting cracks and pipes from geometries that are connected at a bend, and it may be more appropriate to think of one geometrical component above or below the other.

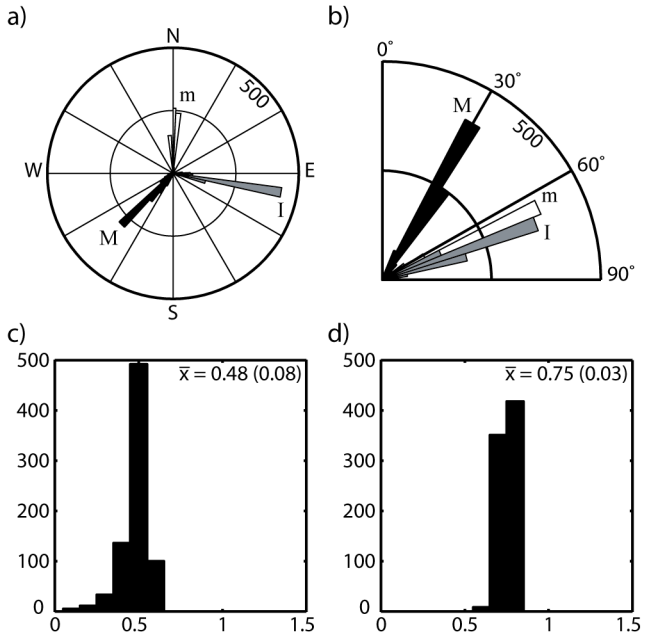

Figure 3.10. Eigenvector statistics for the moment tensor only solution in Figure 3.9. The minimum (m), intermediate (I) and maximum (M) eigenvectors (a and b) are shown in white, gray and black, respectively. Histograms show the amplitude ratio of the largest to smallest (c) and the largest to intermediate (d) dipole, with the largest dipole normalized to 2. The arithmetic mean $\bar{x}$ and one standard deviation (in parenthesis) are also shown.

The combined crack-pipe model consists of a nearly horizontal pipe plunging towards the east and a crack dipping 30° to the southwest. Since the surface projection of the pipe does not intersect the crater the crack would need to be above the pipe. In this case, the magma would be supplied to the crack from a nearly horizontal pipe, which is

an unlikely orientation for a deep feeder pipe. The low angle (~45°) between the pipe and the crack would represent a sharp corner in the conduit that seems unrealistic given the relatively open magmatic pathway that exists at Fuego. The dominant crack in the two-crack model also must also be located above the non-dominant crack in order for one of the components to intersect the crater. However, this leads to a more geologically plausible conduit geometry consisting of a subvertical dike dipping to the northeast feeding a southwest dipping crack that provides a magma pathway to the summit crater.

We test the sensitivity of the two-crack and combined crack and pipe models to angular deviations from the respective best-fit orientation as a final evaluation of the reliability of the forward modeling results. We independently vary azimuth and dip or plunge of each crack and pipe in 5° increments from the best-fit result and invert for these orientations (Table 2). Each orientation was varied by six increments (30°) above and below the best fit, except where the dip or plunge reached 0° or 90°. The standard deviation of the residual errors for each element of the orientation is used as a metric to assess how sensitive each model is to variations in that component (Table 2). The result of angular variation from the best-fit location for each component of the two-crack and combined crack and pipe models are shown in Figures 10a and 10b, respectively. The two-crack model results show that the dominant crack components are more sensitive to variations than the nondominant crack, with the dip of the dominant crack being more sensitive than the azimuth. The secondary crack is relatively insensitive to changes in dip, and is the least sensitive component in either model (Table 2, Figure 3.11a). The azimuth of the nondominant crack has an asymmetric sensitivity about the best-fit

location, with a little sensitivity to clockwise rotation but a high degree of sensitivity to counter-clockwise rotation.

The combined crack and pipe model results show that the dip of the dominant crack is the most sensitive component of this geometry, and the most sensitive component in either model (Table 2). The azimuth of the dominant crack is slightly more sensitive than the plunge or azimuth of the pipe, which have similar sensitivities. These tests confirm that the orientation of the dominant crack is most important in terms of residual errors for either geometry, in particular

Table 3.2. Inversion Error Sensativity to Changes in the Orientation of Model Source Geometry[a]

2 crack model

θ_1	$Ø_1$	θ_2	$Ø_2$	E_1	E_2	θ_1	**$Ø_1$**	θ_2	$Ø_2$	E_1	E_2	θ_1	$Ø_1$	**θ_2**	$Ø_2$	E_1	E_2	θ_1	$Ø_1$	θ_2	**$Ø_2$**	E_1	E_2
5	225	65	35	0.19	0.88	35	**195**	65	35	0.10	0.66	35	225	**35**	35	0.06	0.57	35	225	65	**5**	0.29	1.33
10	225	65	35	0.16	0.80	35	**200**	65	35	0.08	0.63	35	225	**40**	35	0.06	0.53	35	225	65	**10**	0.19	1.03
15	225	65	35	0.13	0.68	35	**205**	65	35	0.07	0.59	35	225	**45**	35	0.05	0.50	35	225	65	**15**	0.13	0.79
20	225	65	35	0.10	0.54	35	**210**	65	35	0.06	0.54	35	225	**50**	35	0.05	0.47	35	225	65	**20**	0.09	0.62
25	225	65	35	0.07	0.44	35	**215**	65	35	0.06	0.49	35	225	**55**	35	0.05	0.45	35	225	65	**25**	0.07	0.51
30	225	65	35	0.06	0.40	35	**220**	65	35	0.05	0.44	35	225	**60**	35	0.05	0.44	35	225	65	**30**	0.05	0.45
35	225	65	35	0.05	0.42	35	**225**	65	35	0.05	0.42	35	225	**65**	35	0.05	0.42	35	225	65	**35**	0.05	0.42
40	225	65	35	0.06	0.48	35	**230**	65	35	0.06	0.44	35	225	**70**	35	0.05	0.41	35	225	65	**40**	0.05	0.42
45	225	65	35	0.08	0.53	35	**235**	65	35	0.07	0.50	35	225	**75**	35	0.05	0.40	35	225	65	**45**	0.06	0.43
50	225	65	35	0.10	0.55	35	**240**	65	35	0.08	0.59	35	225	**80**	35	0.05	0.40	35	225	65	**50**	0.06	0.45
55	225	65	35	0.13	0.55	35	**245**	65	35	0.10	0.69	35	225	**85**	35	0.05	0.40	35	225	65	**55**	0.07	0.48
60	225	65	35	0.16	0.53	35	**250**	65	35	0.11	0.78	35	225	**90**	35	0.05	0.40	35	225	65	**60**	0.08	0.52
65	225	65	35	0.19	0.52	35	**255**	65	35	0.13	0.84	n/a	n/a	**n/a**	n/a	n/a	n/a	35	225	65	**65**	0.09	0.56
standard deviation				0.05	0.14	standard deviation				0.02	0.13	standard deviation				0.00	0.05	standard deviation				0.07	0.27

1 crack, 1 pipe model

θ_1	$Ø_1$	θ_2	$Ø_2$	E_1	E_2	θ_1	**$Ø_1$**	θ_2	$Ø_2$	E_1	E_2	θ_1	$Ø_1$	**θ_2**	$Ø_2$	E_1	E_2	θ_1	$Ø_1$	θ_2	**$Ø_2$**	E_1	E_2
n/a	n/a	n/a	n/a	n/a	n/a	30	**190**	75	270	0.11	0.51	30	220	**45**	270	0.08	0.46	30	220	75	**240**	0.11	0.82
5	220	75	270	0.25	1.43	30	**195**	75	270	0.09	0.50	30	220	**50**	270	0.07	0.43	30	220	75	**245**	0.09	0.70
10	220	75	270	0.17	1.13	30	**200**	75	270	0.07	0.47	30	220	**55**	270	0.06	0.40	30	220	75	**250**	0.07	0.57
15	220	75	270	0.11	0.76	30	**205**	75	270	0.05	0.44	30	220	**60**	270	0.06	0.37	30	220	75	**255**	0.05	0.47
20	220	75	270	0.07	0.49	30	**210**	75	270	0.05	0.40	30	220	**65**	270	0.05	0.35	30	220	75	**260**	0.04	0.40
25	220	75	270	0.05	0.35	30	**215**	75	270	0.04	0.36	30	220	**70**	270	0.04	0.34	30	220	75	**265**	0.04	0.36
30	220	75	270	0.04	0.35	30	**220**	75	270	0.04	0.35	30	220	**75**	270	0.04	0.35	30	220	75	**270**	0.04	0.35
35	220	75	270	0.06	0.49	30	**225**	75	270	0.04	0.36	30	220	**80**	270	0.04	0.39	30	220	75	**275**	0.04	0.34
40	220	75	270	0.11	0.70	30	**230**	75	270	0.05	0.41	30	220	**85**	270	0.06	0.51	30	220	75	**280**	0.04	0.34
45	220	75	270	0.20	0.77	30	**235**	75	270	0.06	0.50	30	220	**90**	270	0.10	0.71	30	220	75	**285**	0.04	0.35
50	220	75	270	0.29	0.68	30	**240**	75	270	0.07	0.63	n/a	n/a	**n/a**	n/a	n/a	n/a	30	220	75	**290**	0.05	0.35
55	220	75	270	0.34	0.61	30	**245**	75	270	0.09	0.76	n/a	n/a	**n/a**	n/a	n/a	n/a	30	220	75	**295**	0.05	0.36
60	220	75	270	0.36	0.65	30	**250**	75	270	0.11	0.89	n/a	n/a	**n/a**	n/a	n/a	n/a	30	220	75	**300**	0.06	0.38
standard deviation				0.11	0.30	standard deviation				0.03	0.16	standard deviation				0.02	0.11	standard deviation				0.02	0.15

[a]Gray field denotes the orientation of the 2 crack and combined crack and pipe model geometries that yield the lowest error. Bold field indicates which component of the model geometry is varying.

the dip of the dominant crack. The results of the two-crack model show that the steeply dipping nondominant crack from the best-fit orientation could be a vertical dike with only a 0.004 increase in E_1 and a decrease in E_2 (Table 2). However, the results of the combined crack and pipe model show that pipe plunging 45°, an orientation more geologically plausible (i.e., more towards vertical), results in large increases in E_1 and E_2

of 0.42 and 0.115, respectively (Table 2). These results further support our preference of the two-crack model over the combined crack and pipe model.

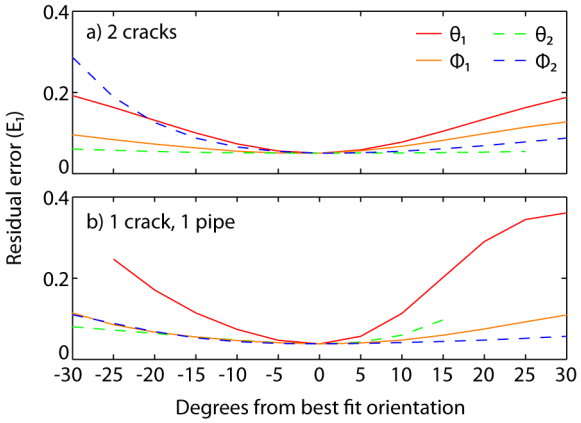

Figure 3.11. Error sensitivities (E_1) to inversions performed at 5° increments above and below the best fit orientations for the two-crack (a) and combined crack and pipe (b) models. Six increments (30°) on either side of the best orientation were inverted, except where theta reached 0° or 90°. The dip of the dominant crack (θ_1) is the most sensitive component of orientation in both models (see Table 2).

The synthetic waveforms from the two-crack model are plotted in Figure 3.7 in green along with the data and the synthetic waveforms from the best-fit free inversion. Fits between the two-crack synthetics and the other data are generally good, except for noticeable differences in the horizontal components of F9NW and F9SW. To confirm that the two-crack model is consistent with the free inversion, we reconstruct the moment tensor for the two-crack model by summing each pair of corresponding components for the respective source-time functions. The reconstructed moment component source-time functions and the best-fit free inversion source-time functions are shown in Figure 3.12a, and are clearly consistent. Figure 3.12b shows the source-time functions of the two cracks chosen as our best-fit source geometry. We estimate the maximum volume

change during one oscillation in the source-time function of the dominant crack from the amplitude $(\lambda + 2\mu)\,\Delta V$, assuming $\nu = 1/3$ ($\lambda = 2\mu$). We estimate a shear modulus for the crack wall rock following experiments on Mt. Etna basalts that found $\mu = 0 – 30$ GPa over a temperature range of 522 – 1071° C [*Chouet*, 1996a]. The explosions accompanying the VLP signals all ejected incandescent tephra and bombs, so we assume the walls of the conduit are relatively hot so that the shear modulus is at the lower end of this range ($\mu = 10$ GPa). This results in a volume change in the dominant crack of 1570 m^3 and in the subdominant crack of 84 m^3 (Figure 3.12b). While the residual errors and AIC values are somewhat higher for the two-crack model than for the free inversion, we consider this model to be a reasonable representation of the VLP source geometry. Greater station coverage on the east side of the volcano would likely improve the free-inversion source location and source-time functions and result in an improved model of the source.

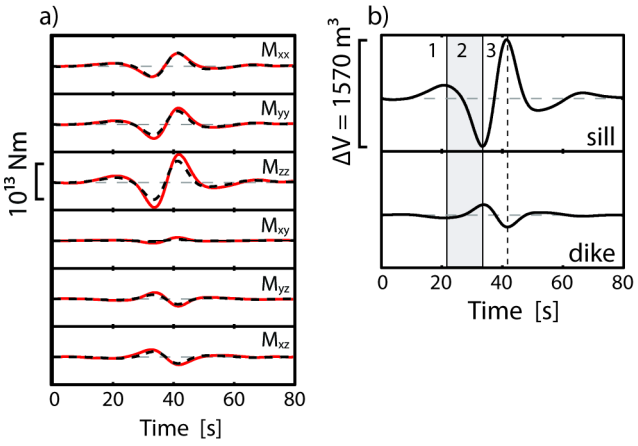

Figure 3.12. The source-time function of the 19 January 2009 explosion VLP (red, a) and the reconstructed source-time function (dashed black, a) calculated using the source-time function for the two-crack model (θ_1 = 35°, $\varnothing_1$ = 225°, θ_2 = 65° and $\varnothing_2$ = 35°). The maximum volume change in the dominant sill (b) is 1570 m^3, assuming μ = 7 GPa. Numbers in (b) represent the pressure history in the sill: 1) final stages of pressurization, 2) explosive depressurization and 3) repressurization.

3.4.6. Other VLP Events

We recorded 52 VLP events that had cross-correlation coefficients greater than 0.85 and were coincident with explosions at our longest running station (F900), in addition to the well-studied event from 19 January. Assuming the waveform similarity indicates that the same source process was operating over the duration of the study, we can compare the waveform inversion results to the other VLP events using a simple linear relationship. Figure 3.13a shows the maximum estimated volume change for each explosion VLP recorded during our experiment based on the volume change in the dominant crack (Figure 3.12b) and the amplitude of the reference event relative to the other events. The estimated volume changes vary greatly, with an average, $\Delta\overline{V}$, of 1041 m^3, and one standard deviation of 480 m^3. The largest and smallest events represent volume changes of 2062 m^3 and 192 m^3, respectively. The cumulative ΔV over the

course of the study (red line in Figure 3.13a) is 5.5 x 10^4 m^3. Despite the variability in the size of the VLPs, the rate of volume change is relatively constant over the course of the study. The gray box in Figure 3.13a spans a power outage during which data was not recorded. The slope of the first continuous cumulative volume line (m_1) is 21.7 ($\Delta V/\Delta t$ (in seconds)) and the slope of the second cumulative volume line (m_2) is 20.9, suggesting a steady input of gas and/or magma into the system. Figure 3.13b shows the maximum VLP amplitude plotted against the time since the previous event. The amplitude of the VLP events seems to be generally unrelated to the interevent time, however, it seems that larger events should be expected after long (>14 hours) interevent times.

3.5. Discussion

3.5.1. Source Dynamics

In order to understand the significance of the source mechanism for the VLP source, we examine additional data collected from Fuego. Visual observations and ultraviolet SO_2 images showed that two vents were active in the summit crater during our 2009 experiment, but the exact location of the vents is unknown because aerial surveys over the vent were not conducted. Thermal images and photos from flights over the vent in January and March 2008 show two hot zones, one located near the western edge of the crater and another centrally located nearer the southern margin of the crater floor [W. Rose, personal communication, 2008]. The hot areas generally coincide with the locations of two pit craters within the main crater, and are likely candidates for the two vents that were active in 2009 [G. Chigna, personal communication, 2008]. The summit

crater had a wide breach to the west in 2008, which broadly agrees with observations of the preferential emplacement of lava flows to the west and southwest in recent years and may indicate a westward migration of the vent.

Our VLP source is modeled as two intersecting cracks, and for simplicity in the discussion we will describe the shallowly dipping crack as a sill and the steeply dipping crack as a dike. The modeling assumes a point source, but given the predicted orientation of the two cracks the sill is most likely located above the dike. The dip of the sill (35°) is the same as the slope of the upper cone of Fuego and we suggest that the magma pathway near the surface is controlled by a competent layer; potentially buried lava flows. The southwest orientation of the sill agrees with the point-source location of the VLP source and the eigenvector analysis of the source-time function, and indicates that the dike may be supplying magma ~300 m west of the summit crater. As the dike nears the surface, it encounters a resistant lava flow or series of flows, which is easier to follow to the summit than to pierce and establish a new vent on the western flank. The location of the VLP source centroid represents a geometrical discontinuity in the conduit at the upward transition from dike to sill (Figure 3.7). This elbow in the conduit must efficiently couple pressure changes to the conduit walls in order to satisfy our observations that the VLP source is temporally stable and spatially well-resolved. The VLP source location may also have important hazard implications for Fuego given past voluminous edifice collapses [1996a] and a westward step in activity that accompanied the past southward migration of the eruptive center (Figure 3.1).

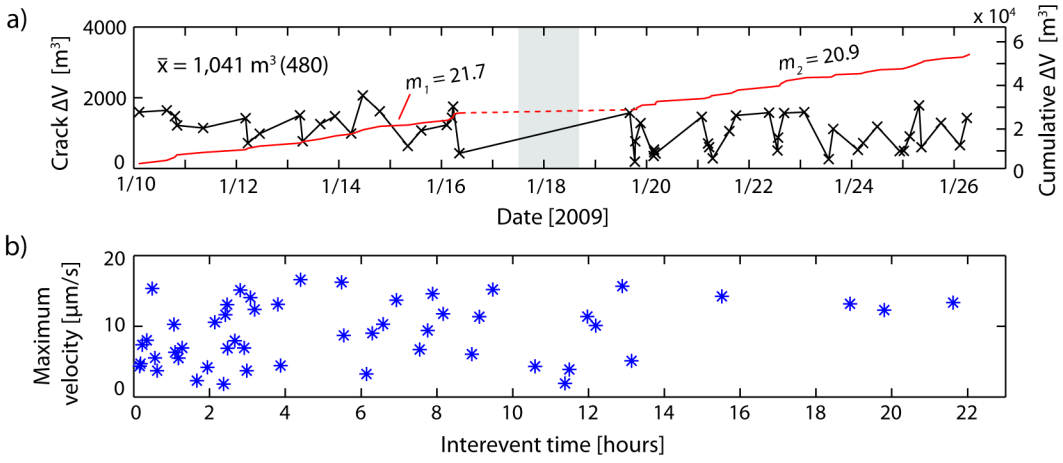

Figure 3.13. Volume estimates (a) of the 52 VLP events recorded at station F900 based on the volume change (Figure 3.11b) and amplitude of the 19 January 2009 reference event. Volumes vary from 192 – 2062 m^3 and the arithmetic mean $\bar{x}$ and one standard deviation (in parenthesis) are also shown. The gray box shows a period when the station was not recording due to a power outage. Cumulative volume change is plotted in red and the slope of the two continuous line segments (m_1 and m_2) show that the volume change is stable over the course of the study. Maximum VLP amplitude and the time since the previous explosion VLP (b) do not show a significant correlation, except when the interevent times exceed 14 hours.

The volumetric components of the moment tensor for the best-fit free inversion display a source process that goes through an inflation-deflation-inflation sequence where the second inflation has a significantly higher amplitude than the first (Figure 3.12a). We propose that this pattern represents a pressurization-depressurization-repressurization cycle in the dominant sill which occurs over ~1 minute in the VLP bandwidth (Figure 3.12b), keeping in mind that the interpreted duration of the source process is constrained by the band-limited VLP signal. This pressure pattern has been observed in other VLP studies of explosive degassing and attributed to conduit processes controlled by conduit geometry, coupling of energy between fluid and solids and magma composition and rheology. At Stromboli volcano, *Chouet et al.* [2008] attribute the pressure history to the

formation and release of a slug of gas that rises and bursts near the surface. Accompanying the movement of the gas slug are changes in the level of the magmatic head as the slug rises through the magma column and as magma drains back onto the column following slug burst. Degassing bursts from the Halemaumau vent of Kilauea volcano similarly involve gas slug ascent through relatively low-viscosity magma, but the VLP signal is excited by the rapid expansion and burst of the gas slug at the magma surface [*Chouet et al.*, 2010]. The VLP energy in this case is produced near the surface but travels down the conduit as an interface wave, not coupling to the conduit wall until a geometrical discontinuity is encountered at ~1 km depth. The source of the energy and the location of the source imaged by the waveform inversion are separated spatially by ~700 m, illustrating the potential complexity of interpreting these signals.

Chouet et al. [2005] proposed that VLP pressure cycles associated with vulcanian explosions at Popocatépetl volcano were driven by volatile supersaturation of stagnant magma due to groundmass crystallization. Initial inflation is caused by diffusive bubble growth, which proceeds until the yield strength of the viscous magma is overcome and flow is induced. Brittle failure and the development of fracture networks results from viscous shear along the conduit walls. Bubble collapse and coalescence occurs as the fractures propagate, leading to a rapid pressure drop in the conduit which collapses the transient fractures and blocks further gas escape. The sudden pressure drop causes diffusion of gas from the melt into bubbles, thereby reinflating the conduit. This process is termed diffusion pumping by *Chouet et al.* [2005] and was further modeled by *Chouet et al.* [2006] to show that repeated pressure recovery could be expected due to small

pressure drops for supersaturated rhyolitic magmas, while also promoting brittle failure of the magma at the conduit interface. *Dawson et al.* [2011] explain the pressure history of VLP signals accompanying vulcanian explosions at Augustine volcano using the diffusion pumping model.

3.5.2. Additional Explosion-Related Data

Although Fuego erupts basalts and basaltic andesites, when we integrate our VLP results with data from apparent tilt, SO_2 emissions and infrasound observations, the rise and burst of gas slugs as the driver of the explosions and source of the VLP energy recorded in 2009 seems unlikely. While the duration of the VLP source process is band-limited to the response of the broadband sensor, we gain further insight into the dynamics driving the explosive eruptions by calculating apparent tilt from the broadband seismic signal. The horizontal components of broadband seismometers are sensitive to tilt, through variable acceleration. The effect of tilt on the broadband signal becomes more significant than translation at longer periods and can become dominant at periods beyond 100 s [2006]. Apparent tilt in radians, Θ(t), can be extracted from the broadband record using:

$$\Theta(\boldsymbol{t}) = \boldsymbol{a}_x(\boldsymbol{t}) / \boldsymbol{g} \tag{3.6}$$

where $\boldsymbol{a_x(t)}$ is apparent ground acceleration and $\boldsymbol{g}$ is gravitational acceleration [2006]. We deconvolve the signal in the 100 – 600 s passband, differentiate to acceleration and remove the effect of gravity to obtain tilt as a function of time. The tilt traces were rotated into radial and tangential from the summit crater, and tilt is defined as positive when it is away from the summit. The dominant period of the tilt signal is ~350 s, well

below the 30 s corner of the instrument closest to the summit (F900). However, we are able to recover the tilt signal because acceleration beyond the corner frequency drops off only linearly, whereas velocity falls off quadratically [*Wielandt and Forbriger*, 1999].

Figure 3.14 shows an explosion that produced a VLP signal and also a positive radial tilt signal of 80 nanoradians (nrad) on 10 January. The onset of tilt away from the summit begins 5 minutes prior to the impulsive expression of the explosion in the broadband seismic and acoustic data. The positive tilt signal is followed by a rapid decrease in tilt of 100 nrad over 1 minute. The tilt cycles may represent pre-explosion pressurization of a relatively shallow portion of the conduit.

High sample rate (~2 Hz) ultraviolet SO_2 emissions were recorded concurrent with our seismic and acoustic data and provide additional for the role of gas accumulation in the explosions. *Nadeau et al.* [2011] recorded slow decreases in SO_2 emissions prior to explosions, sometimes lasting tens of minutes, followed by sharp increases in emissions after the explosions. The duration of these events is inconsistent with bubble rise rates, as is the pattern of emissions. *Nadeau et al.* [2011] invoked rheologic stiffening of the magma in the upper to explain the degassing pattern and explosive activity.

Figure 3.14a shows a typical infrasound signal generated by explosions associated with VLP events. The infrasound waveform displays a relatively simple compression-rarefaction sequence with a characteristic asymmetry skewed toward the initial compression (Figure 3.14a). While short-lived, the explosive infrasound releases a broad spectrum of energy from ~80 s – 2 Hz. Infrasound records of explosions recorded across

the network do not display a linear relationship of decreasing amplitude with increasing distance, which is expected for acoustic waves propagating at atmospheric velocity. Instead, the amplitude of the infrasound at the closest station (F900) is much higher than at more distant stations. Non-linear propagation of acoustic waves is attributed to high energy explosions (vulcanian or plinian), and are not associated with strombolian behavior [2011].

3.5.3. Degassing Crystallization and Brittle Failure

Persistently degassing volcanoes with relatively constant SO_2 emissions indicate a large, deep supply of SO_2-rich mafic magma and a permeable or convecting conduit that is capable of a near-steady gas supply despite different styles of eruptive behavior [*Shinohara*, 2008]. The degassing and eruptive history of Fuego and its magma composition suggest that this model broadly applies [*Chesner and Rose*, 1984; *Lyons et al.*, 2010; *Martin and Rose*, 1981; *Rodríguez et al.*, 2004], but our observations indicate that in January 2009 a different process dominated in the shallow conduit. Fuego magmas, like many other arc basalts, have high water content at depth (2.1 – 6.1 wt% H_2O) [*Roggensack*, 2001; *Sisson and Layne*, 1993], and the precipitous loss of water as the magma nears the surface may explain why Fuego basalts seem to behave like more silicic magmas. Undercooling of magmas by degassing triggers nucleation and growth of crystals in the magma, which rapidly increase melt viscosity and allow for the development of basalts with high yield strengths [*Sparks and Pinkerton,* 1978].

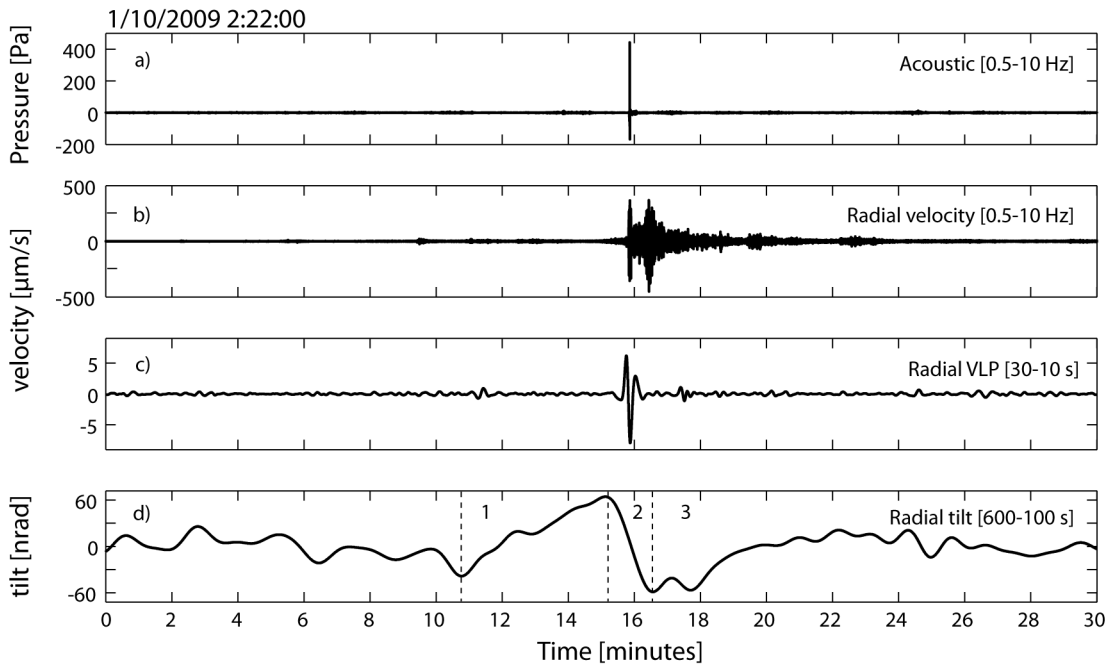

Figure 3.14. An explosion on 10 January 2009 that generated a clear tilt signal at station F900 starting 5 minutes prior to the arrival of high-amplitude seismic and acoustic energy. The north seismic channel is rotated to be oriented radially from the summit crater. Infrasound (a), radial SP velocity (b), radial VLP velocity (c) and apparent radial tilt (d) are plotted for comparison with the bandpass for each trace shown in brackets. Positive tilt is motion away from the summit. Numbers in (d) indicate the phases of the tilt sequences associated with large explosions: 1) inflation of the upper edifice due to pressurization, 2) rapid depressurization and 3) slow recovery of the edifice.

The rate of cooling due to water loss is about 20° C per 1 wt% [*Boyd,* 1961], and using the VolatileCalc program [*Newman and Lowenstern,* 2002] we estimate that for a basalt similar to Fuego basalts the solubility of water at the depth of our VLP source and 900° C is 0.73 wt%. Assuming a starting concentration of 5 wt%, Fuego basalts are undercooled by 80° C by the time they reach our VLP source depth. *Kirkpatrick* [1976; 1977] shows that maximum nucleation and crystal growth rates for basalts occur at undercooling of 50 – 100° C, so we anticipate significant crystallization and changes to rheology as Fuego magmas near the surface. Plagioclase crystals would be expected to

grow to 1 mm in 1 – 2 hours at 80° C of undercooling, so a highly crystallized plug of magma could quickly form and reform at the top of the magma column, especially during periods of low mass eruption rate [*Kirkpatrick* , 1976; 1977]].

Crystallization of anhydrous mineral phases from a volatile-saturated melt results in exsolution of volatile phases. *Tait et al.* [1989] show that at the depth of our VLP source (4 – 5 MPa) that 25% crystallization of the melt generates overpressure of ~3 MPa, which is sufficient to break the magma and cause an explosion. *Melnik and Sparks* [1999] modeled the change in magmatic overpressure and porosity with depth at Soufriére Hills volcano using well-constrained physical parameters derived from the andesitic magma regularly erupted in vulcanian explosions and dome collapses. They achieve maximum overpressures of 4 – 8 MPa, typically at several hundred meters below the vent, with maximum porosity occurring at the same depth.

Voight et al. [1999] observed cycles of ground deformation and seismicity accompanying vulcanian explosions and lava dome growth and collapse between 1996 and 1998. They recorded inflation-deflation cycles with periods of 6 – 8 hours in which peak inflation was associated with dome collapses or vulcanian explosions. The cyclic activity is attributed to overpressurization of the upper-most conduit due to crystallization-induced degassing and rheologic stiffening which creates a pressurized plug that resists steady pressure to flow from the magma chamber. When the tensile strength of the plug was overcome, the plug was forced from the conduit by brittle failure causing partial dome collapses or vulcanian explosions. Following the release of overpressure, fresh magma flowed upward and the cycle of degassing and crystallization

began again. *Voight et al.* [1999] modeled the depth of the pressure source from tilt meter data to be at ~400 m below the surface of the dome, similar to the results of *Melnik and Sparks* [1999]. They also estimate an 8 order increase in viscosity due to the process of degassing and crystallization, from 10^6 to 10^{14} Pa s.

A similar model was invoked to explain six vulcanian explosions at Galeras volcano during a period from 1992 – 1995 in which no active dome growth was occurring [*Stix et al.,* 1996]. In this case, overpressurization of a magma plug in the conduit due to degassing crystallization is the dominant explosion driver. However, they also partially attribute the pressurization of the system to the development of a hydrothermal system, which deposits silica minerals in fracture networks, eventually sealing these degassing pathways. These fractures are most likely to develop along the conduit margins where cooling and shear stress are focused. Shear-enhanced permeability would allow degassing pathways to develop and degassing to continue even after the development of a pressurized, rheologically stiffened plug [*Stasiuk et al.,* 1996]. In our case, effective sealing of fractures through annealing, expansion of the magma by diffusive bubble growth or the precipitation of secondary minerals must occur in order to inflate the conduit and restrict SO_2 emissions.

3.5.4. Fuego Explosion Cycles and Conduit Dynamics

The Fuego data and examples from silicic volcanoes suggest that during our experiment explosive behavior was controlled by degassing induced crystallization and brittle failure. This provides a framework for us to interpret the pressurization-depressurization-repressurization sequence of the VLP source mechanism and we

envisage the following pattern: 1) initial inflation records the final, band-limited stages of conduit pressurization, 2) overpressure exceeds the tensile strength of the magma plug and brittle failure occurs, advecting pyroclasts and depressurizing the sill and 3) the sudden pressure drop allows fresh magma to flow upward, re-establishing the magmastatic head and reinflating the sill, where degassing crystallization and pressurization begin again. This mechanism describes a somewhat more general version of the diffusion pumping model proposed by *Nishimura* [2004] and extended by *Chouet et al.* [2005; 2006] which, according to Figure 3 in *Nishimura* [2004], is a potentially viable mechanism for Fuego magmas. However, we prefer a more general model because many of the magma and volatile characteristic needed to solve the system of equations that describes diffusion pumping are unknown for Fuego (e.g., melt viscosity, volatile diffusivity, initial bubble radius, bubble number density). A more general model also allows us to consider the tilt and SO_2 data, as well the timing of the depressurization and repressurization portions of the VLP.

The period of inflation prior to explosions recorded in the tilt signals typically lasts ~4 – 6 minutes, which is relatively short compared to similar signals at Soufriére Hills. The consistency of the timing suggests that once the system becomes effectively sealed, overpressure increases to the failure point of the magma within about 5 minutes. However, we are estimating tilt from broadband seismometers, rather than tiltmeters, which are less sensitive to longer periods as discussed above. The SO_2 emission rates are much more variable, and small explosions and exhalations are more common than the large explosions that accompany VLP events. We interpret this as a sign that complete

sealing of fractures either through expansion of the magma by diffusive bubble growth or by complete crystallization of the carapace of the magma plug is difficult to achieve. Partial sealing of non-interconnected fracture networks could lead to localized overpressures that result in small explosions. Gas preferentially accumulating in fractures on the upper side of the inclined sill may also lead to small gas exhalations and explosions keeping these fractures open longer than fractures on the underside of the sill [*Lane et al.,* 2001].

Unlike in many silicic cases where partial collapse of a dome provides the rapid depressurization to initiate fragmentation of the underlying magma, the fragmentation of the Fuego magma occurred in the conduit. We envisage brittle failure of the upper most layer of the pressurized plug, which triggers a fragmentation wave that propagates downward, triggering a layer-by-layer fragmentation due to the pressure gradient between newly exposed free surfaces and the low pressure area vacated by the previous layer [*Fowler et al.,* 2010]. This failure mechanism has been repeatedly observed in laboratory experiments and the velocity of the fragmentation wave was measured for Mt. Unzen dacites [*Scheu et al.,* 2006] and Soufriére Hills andesites [*Kennedy et al*, 2005]. Both studies found that the porosity of the sample had the greatest effect on the fragmentation threshold (overpressure), with greater percentages of open porosity reducing the fragmentation threshold pressure and the fragmentation speed. At 3 – 5 MPa of overpressure (our estimate of Fuego overpressure), samples needed ~40% porosity in order to fail, and the fragmentation speed would be 10 – 20 m/s. Assuming that fragmentation progresses for approximately as long as the depressurization phase in

the source-time function, we could expect 100 – 300 m of the upper magma column would fragment. Approximating the geometry of the conduit as a long, thin sill, the volume fragmented broadly agrees with the maximum volume change estimated in our dominant sill (Figure 3.12b). Fragmentation will stop when either the porosity decreases or the overpressure drops below the fragmentation threshold [*Scheu et al.,* 2006].

The final repressurization of the sill is most likely the combined effect of fresh magma rapidly flowing back into the sill to reoccupy the volume evacuated in the explosions and coeval expansion of the bubbles in the melt due to depressurization and diffusive growth. *Chouet et al.* [2006] demonstrated that for rhyolitic melts the timescales of diffusion pumping and crack response can vary from 1 μs to 1000 s. The response time is particularly sensitive to diffusivity, bubble number density, conduit aspect ratio and initial bubble size. These values are poorly constrained at Fuego, making it difficult to discern how much of the repressurization response can be attributed to diffusive bubble growth. Experimental work is underway on Fuego magmas that should provide constraint on some of the magma characteristics critical to accurately modeling diffusive bubble growth following a pressure drop [Robert and Whittington, personal communication, 2011]. A striking difference exists between the timing of the repressurization of the sill (15 s, Figure 3.12b) and the recovery of the tilt signal (5 minutes, Figure 3.14d). This may be due to different timescales of elastic response between the sill walls and the entire edifice. An in-depth investigation of the tilt signal is the subject of future work.

3.6. Conclusions

We investigate eruption dynamics at Fuego volcano by analyzing VLP signals associated with explosions in 2009. The results of a full waveform inversion in the VLP band image a source 300 m below and 300 m west of the summit crater. Eigenvector ratios of the source-time function are stable for the duration of the source process and consistent with a crack dipping gently to the southwest. We refine the inversion results through forward modeling and find that two intersecting cracks provide the most viable model. The dominant crack is shallowly dipping to the southwest while the subordinate crack is steeply dipping to the northwest. We interpret the cracks to represent a near-vertical dike feeding a sill that dips 35° to the southwest. We interpret the cracks to represent a near-vertical dike feeding a sill that dips 35° to the southwest. The orientation of the dominant sill suggests that it is defined by a strong layer, such as a lava flow at depth, which is easier to follow to the surface than to break through and establish a new vent on the western flank. However, this may indicate that the main feeder dike has migrated southwestward from directly beneath the summit crater, which has potential hazard implications since the edifice is buttressed to the north and the volcanic complex has a history of edifice collapse.

We interpret the source-time functions to represent a pressurization-depressurization-repressurization cycle in the sill. Apparent tilt, SO_2 emissions and infrasound data all provide evidence that the VLP signal and explosions are consistent with a model in which repeated degassing-driven crystallization and brittle failure in the upper most portion of the magma column drives explosive activity and VLP generation.

Fuego magmas become significantly undercooled during ascent due to water loss causing microphenocryst growth, further volatile exsolution and rheologic stiffening of the magma. This results in a pressurized, highly viscous plug of magma effectively sealing the conduit, as evidenced by a decrease in SO_2 emissions and inflation in the tilt data minutes prior to explosions. Brittle failure of the most viscous portion of the plug occurs as the overpressure rises above the tensile strength of the basalt, causing a downward propagating fragmentation front that evacuates the high porosity plug. Fresh magma rapidly flows into the sill and inflates due to rapid bubble expansion following the depressurization, and the cycle begins again. This process has been proposed as the driver of vulcanian explosions at more silicic volcanoes, but we are not aware of this process having been recorded in other basaltic systems. More research is needed at other explosively erupting basaltic volcanoes in order to better understand the variability that leads to different eruptive styles over short timescales. This study illustrates the utility of broadband seismometers in elucidating shallow eruption dynamics, conduit geometry and volcano deformation, and highlights the value of multi-parameter investigations at active volcanoes.

Acknowledgements

We gratefully acknowledge field support from Edgar Barrios, Kyle Brill, Chris Brown, Amilcar Calderas, Gustavo Chigna, Mari Dalton, Jemile Erdem, Tricia Nadeau, Josh Richardson, Jesse Silverman, INGUAT and INSIVUMEH. Thanks to PASSCAL

for data acquisition support and equipment. Research and travel was supported by NSF PIRE 0530109. Thanks to Rüdiger Escobar and Bill Rose for stimulating discussion that improved the manuscript.

CHAPTER 4

Inflation-Deflation Cycles Recorded with Broadband Seismometers at Fuego Volcano: The Effect of Steep Topography on Tilt

4.1. Introduction

The dynamics of small (VEI < 2), transient volcanic explosions are becoming increasingly understood through the use of portable broadband seismometers, which allow for investigation of signals over a wide range of timescales. Very-long-period (VLP) signals have been used to image conduit geometry and unravel the source mechanism of strombolian and vulcanian explosions, and these studies typically make use of signal down to the natural period of the instrument [e.g., *Chouet et al.*, 2003; *Dawson et al.*, 2011; *Waite et al.*, 2008]. Several studies have extended the timescale of observation beyond the low corner of portable seismic sensors to investigate small ground rotation signals accompanying short-lived explosions that can be extracted from the horizontal components of broadband sensors [*Aoyama and Oshima*, 2008; *Genco and Ripepe*, 2010; *Wielandt and Forbriger*, 1999]. The ability to recover information about ground displacement and tilt with a single instrument greatly facilitates the study and understanding of volcanic eruptions, particularly in places where more permanent installations of dedicated tiltmeters are impossible.

Inflation – deflation sequences related to slow accumulation of pressure and explosive degassing have been well-documented using tiltmeters and broadband seismometers for large eruptions at Soufriere Hills [*Voight et al.*, 1999], Merapi [*Voight et al.*, 2000], and Anatahan [*Wiens et al.*, 2005]. However, similar sequences over shorter timescales have been recorded using broadband seismic records of strombolian explosions [*Genco and Ripepe*, 2010; *Wielandt and Forbriger*, 1999]. In other cases, tilt from broadbands have recorded deflations associated with phreatic explosions at

Meakan-dake [*Aoyama and Oshima*, 2008] and small pyroclastic explosions at Santiaguito [*Johnson et al.*, 2009]. The timescale and pattern of volcano deformation accompanying explosions facilitates the interpretation of eruption dynamics, especially when recorded in conjunction with other remote sensing data.

In this paper, we report observations of tilt recorded on broadband seismometers associated with explosions from Fuego volcano, Guatemala, recorded over 20 days in January 2009. Fuego is a 3800 m stratovolcano that regularly produces strombolian and weak vulcanian explosions, which we recorded on a temporary network of broadband seismic (Güralp CMG-3ESPC and CMG-40T sensors, 60 and 30 s corners, respectively) and infrasound sensors (All Sensors differential pressure transducers, 0.001 – 50 s) deployed 800 m to 2 km from the summit crater (Figure 4.1). The strongest recorded explosions generated impulsive infrasound and seismic signals, ejected incandescent bombs and tephra, and were associated with repetitive VLP seismicity. A waveform inversion of a VLP event locates the source centroid 300 m west and 300 m below the level of the summit crater, and the source mechanism is interpreted to be an inflation-deflation-reinflation cycle in a shallowly dipping sill [*Lyons and Waite*, 2011].

The stations that most reliably recorded tilt were located on the steep upper cone of the volcano, which contains a prominent ridge extending to the north (Figure 4.1). We record a correlation between tilt polarity and sensor location that suggests the influence of the topography on the tilt signal. The effects of topography on tilt signals have been modeled numerically [e.g., *Cayol and Cornet*, 1998; *McTigue and Segall*, 1988; *Rodgers*, 1968], but we are unaware of other natural datasets that display this effect at active

volcanoes. We attempt to model this effect and constrain the depth and geometry of the tilt source with the three-dimensional (3D) finite-difference method of *Ohminato and Chouet* [1997], including the 3D topography of Fuego. We interpret the tilt signal to represent inflation of the shallow conduit prior to the explosive release of overpressure due to the formation of a plug with high yield strength through extensive degassing crystallization, and show that topography must be considered in modeling source depth and geometry on steep volcanoes.

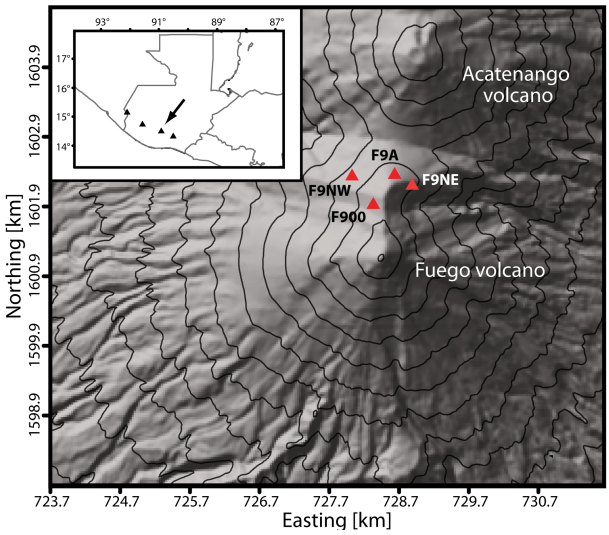

Figure 4.1. Digital elevation model of Fuego volcano indicating the locations of the broadband seismic stations that recorded a tilt signal associated with explosions in January 2009. Notice the steep topography the stations were installed on and the prominent ridge extending north from the summit of Fuego. Contour interval is 200 m.

4.2. Tilt Data

The horizontal components of broadband seismometers are sensitive to tilt through gravitational acceleration. *Rodgers* [1968] characterized the effect of tilting on inertial seismometers and described the relationship between displacement and tilt as a function of angular frequency. A recent experiment by *Aoyama and Oshima* [2008]

confirms that the horizontal components of modern force-feedback broadband seismometers are also susceptible to tilt. The broadband signal is more susceptible to tilt with increasing period so that tilt dominates translation at periods below the sensor corner if the seismometer experiences substantial rotation [*Wielandt and Forbriger*, 1999]. Tilts associated with relatively weak strombolian and vulcanian explosions can be quite small, but some tilt signal can still be recovered from the broadband record because the CMG-40T and CMG-3ESPC sensors have a flat response to tilt below the natural period [*Aoyama and Oshima*, 2008; *Genco and Ripepe*, 2010]. This allows us to calculate tilt $S_T(\omega)$ from the response to displacement $S_U(\omega)$ by using a tilt transfer factor $T_F(\omega)$ determined from the poles and zeros of a given instrument [*Aoyama and Oshima*, 2008]:

$$S_T(\omega) = -T_F(\omega) S_U(\omega) \tag{1}$$

For the CMG-40T and CMG-3ESPC, the tilt transfer factor can be determined from the poles p_n, zeros z_n, normalizing factor c, and the number of poles and zeros N_p, N_z,:

$$c\left[\frac{\prod_{m=1}^{N_z}(i\omega - z_m)}{\prod_{n=1}^{N_p}(i\omega - p_n)}\right] \tag{2}$$

where *i* indicates a complex number. The tilt transfer factors for the two sensor types are plotted in Figure 4.2 and clearly show the constant amplitude response below the natural period. *Genco and Ripepe* [2010] proposed simpler method to calculate the tilt transfer factor based solely on the natural period ω_0 of the sensor $T_F(\omega_0) = \omega_0^2 / g$. Figure 4.2

shows that for these two sensors the methods are in agreement, and that the tilt transfer factor is 4.47×10^{-3} rad/m for the CMG-40T and 1.11×10^{-3} rad/m for the CMG-3ESPC.

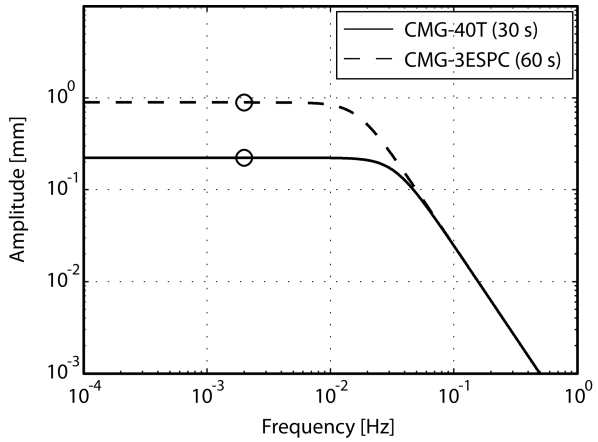

Figure 4.2. Synthetic amplitude transfer curves for CMG-40T and CMG-3ESPC sensors with natural periods of 30 and 60s, respectively generated using the poles, zeros, and normalizing functions for each instrument. These represent the apparent displacement expected for a 1 μrad tilt. The open circles indicate the values determined using the *Genco and Ripepe* [2010] method described above evaluated at 0.002 Hz.

Both sensor responses are proportional to velocity, so we extract the tilt signal by 1) removing the mean, 2) integrating the instrument velocity response to displacement, 3) low-pass filtering below the natural period of the instrument and 4) multiplying by the tilt transfer factor and the digitizer and seismometer sensitivity factors. The tilt signals that we recorded are weak (nanoradians) and this method of extracting tilt can be controversial, particularly when dealing with filtering over an impulsive explosions signal. To ensure that the tilt signals were not function of filtering, we initially extracted only displacement from the full sample-rate, unfiltered velocity record in windows centered on the times of known explosions that produced an infrasound pulse of >100 Pa at station F900. The unfiltered displacement plots show strong instrument drift and other

spurious noise, possibly due to someone walking near the sensor or barometric effects, and a simple S/N evaluation was used to discard especially noisy traces. The station nearest the vent, F900, has the highest signal to noise ratio, and a clear pattern emerges in the unfiltered displacement traces when the events are plotted together (Figure 4.3). This is unequivocal evidence that a repetitive signal is recorded ~20 – 30 minutes prior to the explosions, and that this is not a filter or signal processing artifact. The strength of the tilt signal decreases rapidly with distance, but through stacking we are able to detect coherent signal at the four closest stations. In some cases the sensor drift and the tilt signal have the same polarity, increasing the difficulty of observing the signal. However, the drift in the vertical channel also provides another check that we are recording real signal on the horizontal channels and not an effect of stacking noise (Figure 4.4).

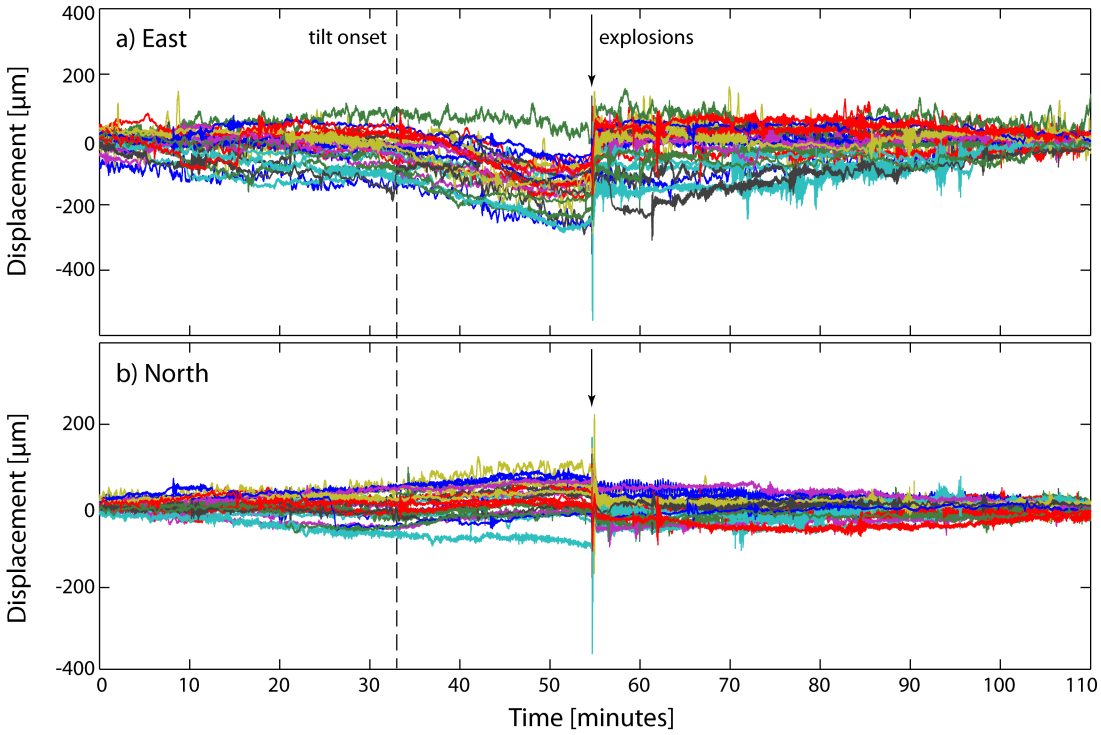

Figure 4.3. Unfiltered displacement traces for 24 explosions recorded at station F900, including the linear correction from counts to m/s. The sensor response was not deconvolved, in order to simplify the interpretation. Instrument drift and other high-frequency noise produce significant variation in the traces but a clear, consistent trend occurs at ~32 minutes (vertical dashed line) that indicates the onset of a coherent tilt signal. The impulsive explosions occur at ~54 minutes (arrow), more than 20 minutes after the initial tilt signal.

Figure 4.5 shows tilt stacks of 24, 12, 14 and 29 events for stations F900, F9NE, F9NW and F9A, respectively. These plots represent unfiltered, full sample-rate displacement that were then stacked, decimated to 10 sps to improve filter stability, and then low-pass filtered below the natural period of the instrument (40T = F900, F9A; 3ESPC = F9NE, F9NW). A single pass, causal filter was used in order to avoid production of any spurious signal sometimes caused by non-causal filters. However, a non-causal filter was also used to investigate filter artifacts and we found that when following this signal processing routine, minimal changes to the tilt signals were

introduced. The tilt onset times vary from ~20 – 30 minutes prior to the explosion onset, with earlier onsets recorded at the stations with 60 s instruments, possibly indicating greater sensitivity to longer period tilt.

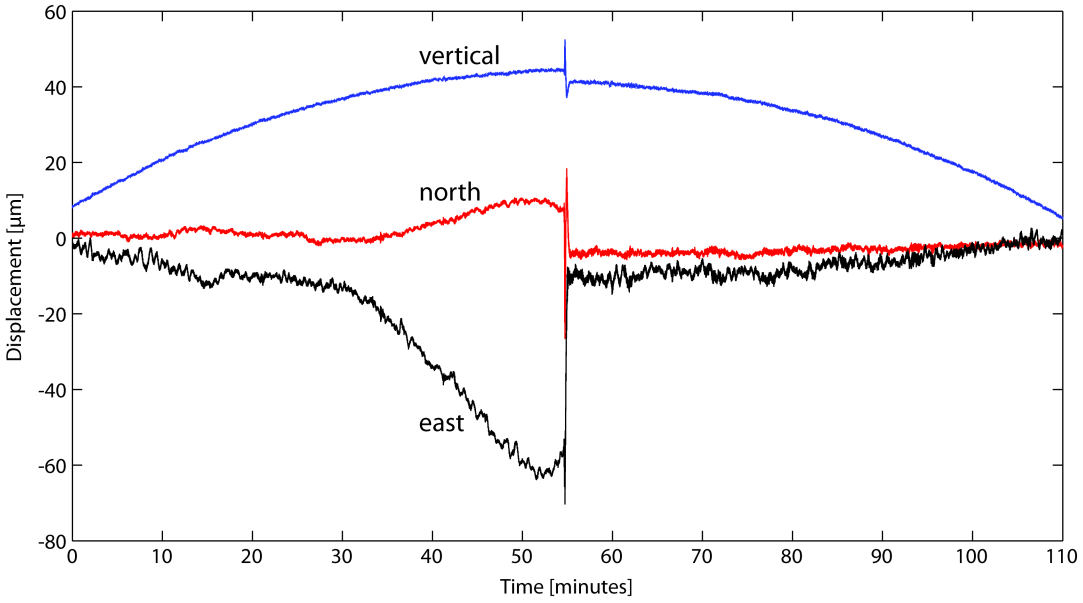

Figure 4.4. Unfiltered displacement stacks of the 24 explosions from Figure 4.3. The tilt signal clearly starts at ~31 minutes in the north and east channel, while the vertical channel only records instrument drift until the explosions occurs at ~55 minutes.

The topography at Fuego is extreme and irregular, with a sharp north-south trending ridge extending north from Fuego's summit that terminates in a steep north-facing slope (Figure 4.1). The change in tilt polarity at different station locations on this topography is striking. Westward tilt dominates at F900 and F9NW, while F9A displays only northward motion and F9NE shows mostly north tilt, with a minor east component (Figures 4.5 and 4.6). While it is possible that individual site effects or inhomogeneous substrate strength could cause this relationship, the systematic variation in polarity with station location on the steep and irregular topography of Fuego is a more likely candidate.

Thus, any estimation of tilt source depth and geometry must include the topography of Fuego's upper edifice.

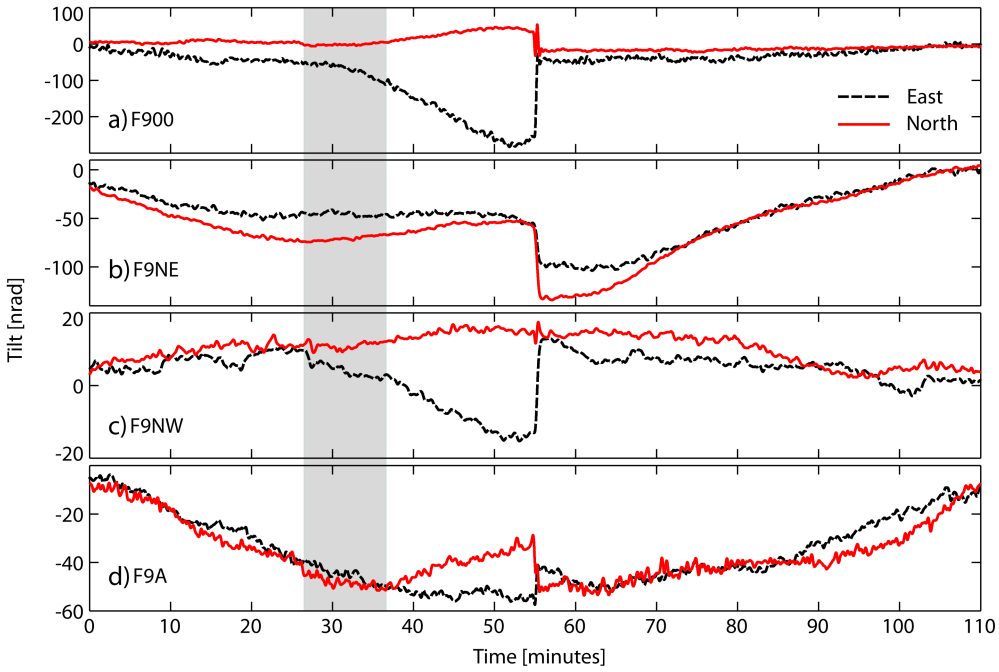

Figure 4.5. Stacks of tilt signals preceding explosions at stations F900 (24 events), F9NE (12 events), F9NW (14 events), and F9A (29 events). The gray box indicates the span of tilt onsets at the different stations. Instrument drift is clear in all the stations except F900 due to the low amplitude of the tilt signal at the stations further from the summit. Tilt away from the summit (inflation) last ~25-30 minutes before the explosion onset (at minute 55).

4.3. Modeling the Tilt Source

Volcanic deformation is often modeled using either an isotropic volumetric point source [*Mogi*, 1958] or an Okada dislocation surface (dike or sill) [*Okada*, 1985] due to the simplicity of these models and the ease of implementation. However, these models do not incorporate topography which has been modeled to have a strong effect on the deformation field, particularly for slopes above 20° [*Cayol and Cornet*, 1998; *Meo et al.*,

2008], and neither of these models are able to replicate the tilt signals we recorded. Based on these results, we choose to include the 3D topography in forward models of the tilt signal through the finite-difference method of *Ohminato and Chouet* [1997]. Our model space is centered at the summit of Fuego and extends 12 km east – west, 9 km north – south and 6 km in the vertical, with 40 m grid spacing. We use a homogeneous velocity model because the velocity profile of Fuego is unknown. The compressional wave velocity is 3.5 km/s, shear wave velocity is 2 km/s and density is 2650 kg/m^3. Synthetic Green functions of the curl of the displacement field (equal to twice the tilt) are generated with the finite-difference code. We convolve the Green functions with a 20 s cosine stabilizing function that has energy in periods longer than 10 s. While we tested much longer-duration source-time functions, this 20 s signal produces synthetic rotations with the same simple shape and amplitude, thus decreasing computing time and increasing the number of source locations were able to consider.

We consider three potential source geometries: single pipes, single cracks and isotropic sources. The pipe and crack moment tensors are generated using equations (15) and (16) of *Chouet* [1996], assuming $v = 1/3$ ($\lambda = 2\mu$). Crack orientations are described by the pole to the crack plane with azimuth, $\emptyset$, measured counterclockwise from east. Pipe azimuth, $\emptyset$, is measured counterclockwise from east in the direction of plunge, θ, from vertical. Although we have some information about the geometry of the conduit from the VLP waveform inversion [*Lyons and Waite*, 2011], we initially vary θ in 15° intervals and $\emptyset$ in 30° over all possible crack and pipe orientations for source locations

extending 500 m west, 100 m east, 300 m north – south and 500 m below the summit crater.

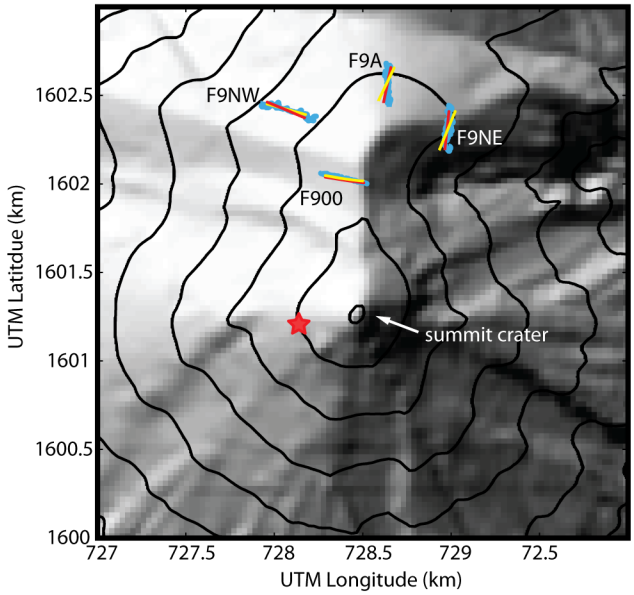

Figure 4.6. Tilt particle motions plotted at the station locations on a DEM of Fuego's upper cone. Blue traces are the stacked data, red traces are for the best synthetic crack and yellow traces are the best synthetic pipe. Amplitudes are normalized by station. The red star represents the location of the best-fit synthetic pressure source. Contour intervals are 200 m.

4.3.1 Model Results

Rather than performing a full-waveform inversion, we chose to simply compare the tilt direction and magnitude of the real data and synthetics. As discussed in the previous section, there are subtle differences in the tilt waveforms between the 60 s and 30 s sensors, which hint at possible errors in the tilt estimates. We are unable to quantify the uncertainty in the absolute tilt values determined using different types of broadband seismometers. However, we expect reasonably consistent values from both horizontal channels of the same sensor, meaning the ratio of the two channels should be reliable.

Therefore we chose to model the tilt "particle motions" rather than the whole waveform. We then examined the tilt magnitudes to help discriminate between different models. The synthetic results are compared with the data by determining the covariance between the north and east components of the particle motion, extracting the maximum eigenvalue and related eigenvector, and calculating the RMS error of the difference between the pairs of maximum eigenvectors for each station.

Table 4.1 shows the crack, pipe and isotropic models that produce the lowest RMS residual between the synthetic and real tilt directions. The polarities of the synthetic tilts with the lowest RMS error were then compared with the data because polarities close to 180° from actual particle motion can also produce low errors. In every case, the isotropic sources produced polarities opposite the real data, indicating deflation prior to each explosion rather than inflation. The crack and pipe models with lowest RMS errors all produced polarities consistent with the data and with inflation preceding each eruption. As a complimentary test of the crack and pipe model results, we compared the standard deviation of the amplitude ratios between the east and north components of tilt for the data and synthetics for the models with the lowest RMS values. Generally, the models with lowest RMS values are associated with low standard deviations in amplitude; however, some variation between the two values for different models exists, indicating that the model geometry is not well constrained.

Table 4.1. Synthetic tilt results based on RMS error[a]

Geometry	RMS error	Amplitude SD[b]	Node[c]	Theta	Phi
Crack	0.1308	9.42	119_107_141	45	150
Crack	0.1805	6.45	119_107_139	60	310
Crack	0.1886	8.99	119_107_139	45	300
Pipe	0.1477	22.79	119_107_141	45	60
Pipe	0.1561	383.44	119_107_141	45	50
Pipe[d]	0.1855	11.49	119_107_141	90	210
Isotropic[d]	0.298	–	121-107-143	–	–
Isotropic[d]	0.304	–	119-107-83	–	–

[a]RMS error is expressed as the angluar difference (in degrees) between the real and synthetic tilt particle motions.

[b]Standard deviation of real and synthetic data for east to north tilt at all stations.

[b]Summit crater is located at node 125-107-145. Model nodes decrease to east, south and down in 40 m increments.

[d]Tilt polarity of these synthetics do not match the data.

All the best fit cracks and pipes are located ~300 m west and between 200 – 300 m below the summit crater, which is near the location of the VLP source centroid identified by *Lyons and Waite* [2011] (Figure 4.6). The cracks with the lowest RMS error are all northeast-southwest striking with dips of 45 – 60 degrees; however, the best-fitting crack dips to the northwest while the others dip to the southeast (Table 4.1). The best-fitting pipes with polarities matching the real data are plunging 45 degrees to the north-northeast (Table 4.1). Both of these geometries are substantially different than the conduit geometry inferred from the VLP analysis of *Lyons and Waite* [2011], which is interpreted as a northeast trending, near-vertical dike located below a sill that dips shallowly to the southwest and intersects the summit crater. However, this discrepancy is likely the result of a tilt signal generated by an extended source and modeling performed assuming a point source. In this case, it is possible that the best-fit crack and pipe

synthetic geometries actually represent the compilation of more than one pressurizing conduit geometry. Figure 4.6 shows that the particle motions for the lowest RMS crack and pipe models both fit the tilt data reasonably well, and in particular both models fit the closest station, F900, very well. This result strongly suggests that the steep topography of Fuego has a significant influence on the tilt signal.

We estimate the volume change needed to generate the synthetic tilts for the best-fit crack and pipe geometry and compare these values to the volume change estimate derived from the VLP signal (1570 m^3) by *Lyons and Waite* [2011]. To estimate a volume change, we calculate the ratio of the maximum real amplitude γ_d to the maximum synthetic amplitude γ_m for each horizontal channel of each station s_c, scale the ratio based on the moment required to produce the synthetic tilt M_m, and divide by the shear modulus μ:

$$\Delta V = \frac{\gamma_d^{s_c}}{\gamma_m^{s_c}} M_m \mu^{-1} \tag{3}$$

We use the same shear modulus (10 GPa) as *Lyons and Waite* [2011] and the moment used in our modeling is 1 N·m. The volume estimates vary significantly between stations, primarily as a result of higher recorded tilt amplitudes at F900 than at F9NW and F9NE (Figure 4.3). This is most likely due to the rapid decrease in tilt amplitude with increased distance from the source. The volume change estimates based on the amplitudes of the best-fit crack model vary from 1743 to 25,600 m^3, and the estimated volume changes from the best-fit pipe model are 2000 to 127,400 m^3. These estimates are lower limits and represent volume changes from 1.1 to 81 times greater than that

estimated by the VLP signal. Although the volume change is poorly constrained, we consider the range to be adequate given the uncertainties in actual tilt magnitude and small number of stations used to constrain the model. The fact that the tilt-derived volume change exceeds that determined from the VLP signals suggests that the tilt inflation is occurring over a larger region in the upper conduit.

4.4. Discussion

Inflation – deflation deformation cycles associated with volcanic explosions in silicic systems have been attributed to the pressurization of the conduit beneath a degassed and crystallized plug of magma in the upper-most conduit [*Iguchi et al.*, 2008; *Voight et al.*, 1999; *Voight et al.*, 2000]. In more mafic systems, similar cycles have been recorded and are considered to be the result of gas bubble growth and magma ascent in a relatively open conduit [*Genco and Ripepe*, 2010; *Nishimura*, 2009]. Fuego magmas are basaltic andesites and could conceivably produce the observed tilt signals due to either of these processes, depending on magma supply rate and conduit conditions, which are poorly constrained. However, the duration of the tilt signal, explosion observations, and high infrasound overpressures (> 100 Pa at 1km) suggest that these explosions were not strombolian bubble bursts. *Lyons and Waite* [2011] showed that extensive plagioclase crystallization is expected for Fuego magmas at depths around the best-fit tilt source model due to degassing crystallization. They invoke the destruction of a pressurized plug as the source of the Fuego explosions that produced VLP signals. High sample rate SO_2 emissions were recorded with a UV camera during a portion of the seismic and acoustic

experiment [*Nadeau et al.*, 2011]. The SO_2 emissions show a slow decline over tens of minutes prior to some explosions, followed by a sharp increase after an explosion. *Nadeau et al.* [2011] suggest that this pattern is due to the slow sealing of the degassing pathways at the top of the conduit.

The tilt signals at stations located north of Fuego appear to be at least partially controlled by the steep and unique topography that includes a steep north-south ridge. All stations display motion away from the summit prior to explosions as the result of inflation, but stations west of the ridge tilt to the northwest while stations north and east of the ridge tilt north and east. We attempted to model this effect using the most commonly used models (Mogi and Okada), which do not include topography, but were unable to reproduce the characteristics of the tilt signal. To include the possible effect of topography, we used the 3D finite-difference code of *Ohminato and Chouet* [1997] with the model surface defined by the actual topography of Fuego derived from a DEM. Three model source geometries were considered: a crack, a pipe and an isotropic source. The isotropic source was incapable of reproducing the recorded tilt signals, which is significant since many studies assume an isotropic source. The pipe and crack models both produced geometries capable of reproducing the correct tilt polarity at all the stations. The location of the best-fit point source for these models is located ~300 m west and 200 – 300 m below the summit, which is near the location of the VLP signal located by *Lyons and Waite* [2011]. The geometries of the best-fit pipe and crack are significantly different than the geometry of the conduit determined from the VLP analysis

and we attribute this to the limitation of modeling the tilt using a point source when an extended source is more probable.

4.5. Conclusions

We record deformation associated with explosions at Fuego volcano by extracting tilt from the horizontal components of broadband seismometers. The tilt data record slow inflations prior to explosions and rapid deflations coincident with broadband seismic and infrasound explosion onsets. The tilt data is significantly affected by the steep topography of the upper cone of the volcano. We model the source location and geometry using a finite-difference model that includes the 3D topography of Fuego. Best-fit model results place the pressure source centroid ~300 m west and 200 – 300 m below the summit crater. Isotropic sources are unable to reproduce the tilt motion and suggest that topogaphy must be considered in order to realistically model deformation source locations and geometry on volcanoes with steep topography. Seismic data and gas emissions both suggest that these tilt data are the result of pressure accumulation beneath a plug of degassed magma that effectively seals degassing pathways. The ability to record deformation with portable broadband seismometers aids in unraveling eruption mechanics, particulalry when combined with other geophysical data.

Acknowledgements

We gratefully acknowledge field support from Edgar Barrios, Kyle Brill, Chris Brown, Amilcar Calderas, Gustavo Chigna, Mari Dalton, Jemile Erdem, Tricia Nadeau,

Josh Richardson, Jesse Silverman, INGUAT and INSIVUMEH. Thanks to PASSCAL for data acquisition support and equipment. Research and travel was supported by NSF PIRE 0530109. Thanks to Minoru Takeo, Hiroyuki Kumagai, Takeshi Nishimura, Rüdiger Escobar, Bill Rose and Tricia Nadeau for stimulating discussions about tilt from broadbands and Fuego's activity.

Chapter 5

Summary

This body of work represents the culmination of seven years of observing and thinking about Fuego and its activity. In late April of 2005, as I was preparing to leave for two years in Guatemala, Bill gave me the sage advice to watch and listen to the volcano carefully, and take good notes. The observations I made over the course of two years did not seem to amount to much at the end of the two years and I feared that I was not going to be able to squeeze a quantitative contribution about Fuego's activity out of two years of work. It took returning to Tech and reading others' observations of volcanoes very similar and different to Fuego in order to begin to crystallize what all the different types of activity, event durations and characteristics might mean. The process of just observing the volcano taught me a great deal.

Volcanology is increasingly quantitative, which is a good thing, but for students and those coming from non-geology backgrounds the time spent just listening and watching the behavior lays the foundation for deeper understanding and interpretation of future data. I can write this with confidence because it is certainly true in my case. Having come from a background in petrology and geochemistry, it has been very challenging and often frustrating to make the switch to geophysics. However, I hope that having a somewhat broader background will positively influence the rest of my career and is hopefully represented in the four previous chapters. Despite the very different levels of research and knowledge that these chapters convey, in each case I attempted to incorporate ideas and data from different spheres of volcanology, geophysics, petrology and remote sensing in order to make the salient points more clearly.

5.1. Eruptive Behavior and Cyclic Activity at Fuego

The data and observations in the first chapter are really only a jumping off point for future research on Fuego. Although there have not been any of the paroxysmal eruptions since 2007, the capture of just one of these events with high quality seismic, infrasound, thermal and gas data is something akin to the holy grail for understanding the current activity. Admittedly, it will take luck or perseverance in order to properly study one of the short-lived, high energy eruptions at Fuego, but I think that there are huge gaps in knowledge about the more passive effusive and explosive activity that could be feasibly be addressed. New techniques of analyzing ash particles are revealing incredible amounts of information about the differences in Strombolian eruptions. Despite the difficult access, a quantification of the variability in CO_2 during passive degassing and for explosions should be a future goal. Similar long-term studies are hard to conceptualize without the use of Peace Corps volunteers or more intimate relationships with the volcano observers. The Peace Corps relationship seems to have gone a bit cold toward INSIVUMEH and volcano-based volunteers, but this is a critical relationship and should be nourished. The simple method of tracking lava flow length and recording the qualitative size of eruption noises or column heights should be ongoing by Edgar and Amilcar at the Fuego observatory. They should have daily digital records that could be mined for possible trends in volcanic activity, as well as climate information.

5.2. Explosive Energy Partitioning

The partitioning of explosive energy likely has a great deal of promise, particularly as infrasound sensors become more widely used at observatories. However, I believe that in my naivety I thought that this method would be more powerful for distinguishing between different styles of explosions and more useful for interpreting source information than it is. The results from chapter 2 do reveal some information that can be attributed to source kinetics, but without supporting information like a systematic waveform cluster analysis of the seismic and acoustic data or something similar in the frequency band the results lack weight. I still think that the real utility of this ratio would be best explored using data from an observatory that has permanent stations. A great project for a student would be to get some long records and attempt to work out the details in effectively automating this calculation for Earthworm or other observatory software.

5.3. VLP Waveform Inversion

The waveform inversion in the 30 – 10 s band and forward modeling of the VLP provided a wealth of new information about Fuego's explosions and about the current conduit geometry. As far as I know, this method is one of the most powerful available to currently for imaging the conduit and locating events using short deployments and sparse networks. We were able to locate the source of the VLP energy to a point 300 m west and 300 m beneath the summit crater that currently issues all the explosions. Considering that the Fuego-Acatenango complex has a history of southward migration with westward

steps, this finding raises significant questions about what the future holds for the activity at Fuego. Probably the most important thing to do at this point would be to deploy stations with better azimuthal coverage that we had in 2009 and repeat the inversion. In addition to the seismic VLPs, we also regularly recorded infrasound VLPs but were unable to relate the two in any meaningful way and so they were unfortunately left out of the VLP manuscript. These signals had high amplitudes for such long periods and were almost certainly a source effect, and probably represent a great deal of the story of the explosion dynamics that we are currently missing. A proper method of inverting the infrasound VLP is desperately needed.

5.4. Apparent Tilt from Broadband Seismometers

The ability to recover volcano deformation using the horizontal channels of a portable broadband seismometer was an incredible discovery for me and provided a wealth of knowledge about shallow conduit mechanics at Fuego. However, non-causal filtering, water-level deconvolution and filtering in the frequency domain can all distort short-lived, high-amplitude explosion signals into something that looks like a ultra-long-period tilt signal, so a great deal of care must be taken when processing seismic data to investigate potential tilt. This method is not new but has only been used at a few volcanoes worldwide, most likely because the weak signal is so hard to recover over noise. The tilts recorded at Fuego in association with explosions showed a strong topographic effect, which we were able to model using the same finite-difference method used to in the waveform inversion. We increased the length of the smoothing function to

look at longer period events since the period of the tilts extended out to ~20 minutes. Remarkably, the best-fit location of the pressure source is located in the same area as the VLP source centroid. This suggests that either the methods are working or that the same bias is propagating through both sets of data. The tilts derived from the seismometers are apparent tilts because, unlike tilt meters, the seismometers cannot record tilts down to DC, so the tilt signal is likely band-limited. An interesting future study would be to co-locate tilt meters and broadband seismometers in order to validate and calibrate the signal derived from the seismometers. Additionally, tilt signals exist in the 2009 data set that are not associated with explosions and may indicate a deeper source, which bears investigation.

References

Akaike, H. (1974), A New Look at the Statistical Model Identification, *IEEE Transactions of Automatic Control*, *19*(6), 716-723.

Aki, K., and P. G. Richards (1980), *Quantitative Seismology*, Freeman, New York.

Allard, P., M. Burton, and F. Mure (2005), Spectroscopic Evidence for a Lava Fountain Driven by Previously Accumulated Magmatic Gas, *Nature*, *433*(7024), 407-410.

Alparone, S., D. Andronico, L. Lodato, and T. Sgroi (2003), Relationship between Tremor and Volcanic Activity During the Southeast Crater Eruption on Mount Etna in Early 2000, *Journal of Geophysical Research*, *108*(B52241), 2241-2254, doi: 10.1029/2002JB001866.

Alparone, S., A. Cannata, and S. Gresta (2007), Time Variation of Spectral and Wavefield Features of Volcanic Tremor at Mt. Etna (January-June 1999), *Journal of Volcanology and Geothermal Research*, *161*(4), 318-332.

Alparone, S., A. Cannata, S. Gambino, S. Gresta, V. Milluzzo, and P. Montalto (2010), Time-Space Variation of Volcano-Seismic Events at La Fossa (Vulcano, Aeolian Islands, Italy): New Insights into Seismic Sources in a Hydrothermal System, *Bulletin of Volcanology*, *72*(7), 803-816, doi: 10.1007/s00445-010-0367-6.

Andres, R. J., W. I. Rose, R. E. Stoiber, S. N. Williams, O. Matías, and R. Morales (1993), A Summary of Sulfur Dioxide Emission Rate Measuremnts from Guatemalan Volcanoes, *Bulletin of Volcanology*, *55*(5), 379-388, doi: 10.1007/bf00301150.

Aoyama, H., and H. Oshima (2008), Tilt Change Recorded by Broadband Seismometer Prior to Small Phreatic Explosion of Meakan-Dake Volcano, Hokkaido, Japan, *Geophysical Research Letters*, *35*(6), 6307-6314, doi: 10.1029/2007gl032988.

Arciniega-Ceballos, A., B. A. Chouet, and P. Dawson (1999), Very Long-Period Signals Associated with Vulcanian Explosions at Popocatepetl Volcano, Mexico, *Geophysical Research Letters*, *26*(19), 3013-3016, doi: 10.1029/1999GL005390.

Aster, R., S. Mah, P. Kyle, W. McIntosh, N. Dunbar, J. Johnson, M. Ruiz, and S. McNamara (2003), Very Long Period Oscillations of Mount Erebus Volcano, *Journal of Geophysical Research*, *108*, 148-170, doi: 10.1029/2002jb002101.

Aster, R., D. Zandomeneghi, S. Mah, S. McNamara, D. B. Henderson, H. Knox, and K. Jones (2008), Moment Tensor Inversion of Very Long Period Seismic Signals

from Strombolian Eruptions of Erebus Volcano, *Journal of Volcanology and Geothermal Research*, *177*(3), 635-647, doi: 10.1016/j.jvolgeores.2008.08.013.

Battaglia, J., K. Aki, J. Montagner, and P (2000), Tilt Signals Derived from a Geoscope Vbb Station on the Piton De La Fournaise Volcano, *Geophysical Research Letters*, *27*(5), 605-608, doi: 10.1029/1999gl010916.

Benoit, J. P., and S. R. McNutt (1997), New Constraints on Source Processes of Volcanic Tremor at Arenal Volcano, Costa Rica, Using Broadband Seismic Data, *Geophysical Research Letters*, *24* (4), 449-452.

Blackburn, E. A., L. Wilson, and R. S. J. Sparks (1976), Mechanisms and Dynamics of Strombolian Activity, *Journal of the Geological Society of London*, *132*(4), 429-440, doi: 10.1144/gsjgs.132.4.0429.

Boyd, F. R. (1961), Welded Tuffs and Flows in the Rhyolite Plateau of Yellowstone Park, Wyoming, *Geological Society of America Bulletin*, *72*(3), 387-426, doi: 10.1130/0016-7606(1961)72[387:WATAFIT]2.0.CO.

Buckingham, M. J., and M. A. Garcés (1996), Canonical Model of Volcano Acoustics, *Journal of Geophysical Research*, *101*(B4), 23, 8129-8152.

Burton, M., P. Allard, F. Muré, and A. L. Spina (2007), Magmatic Gas Composition Reveals the Source Depth of Slug-Driven Strombolian Explosive Activity, *SCIENCE*, *317*, 227-229, doi: 10.1126/science.1141900.

Calvari, S., L. Spampinato, L. Lodato, A. J. L. Harris, M. R. Patrick, J. Dehn, M. R. Burton, and D. Andronico (2005), Chronology and Complex Volcanic Processes During the 2002-2003 Flank Eruption at Stromboli Volcano (Italy) Reconstructed from Direct Observations and Surveys with a Handheld Thermal Camera, *Journal of Geophysical Research*, *110*, 2201-2215, doi: 10.1029/2004JB003129.

Caplan-Auerbach, J., and S. R. McNutt (2003), New Insights into the 1999 Eruption of Shishaldin Volcano, Alaska, Based on Acoustic Data, *Bulletin of Volcanology*, *65*(6), 405-417.

Carn, S. A., A. J. Krueger, S. Arellano, N. A. Krotkov, and K. Yang (2008), Daily Monitoring of Ecuadorian Volcanic Degassing from Space, *Journal of Volcanology and Geothermal Research*, *176*(1), 141-150, doi: 10.1016/j.jvolgeores.2008.01.029.

Carr, M. J., L. C. Patino, and M. D. Feigenson (2002), Petrology and Geochemistry of Lavas, in *Central America: Geology, Resources, and Hazards*, edited by J. Bundschuh and G. E. Alvarado, pp. 565-590, Taylor and Francis.

Cayol, V., and F. H. Cornet (1998), Effects of Topography on the Interpretation of the Deformation Field of Prominent Volcanoes - Application to Etna, *Geophysical Research Letters*, *25*(11), 1979-1982, doi: 10.1029/98gl51512.

Chouet, B. (1985), Excitation of a Buried Magmatic Pipe: A Seismic Source Model for Volcanic Tremor, *Journal of Geophysical Research*, *90*(B2), 13-35.

Chouet, B., P. Dawson, T. Ohminato, M. Martini, G. Saccorotti, F. Giudicepietro, G. De Luca, G. Milana, and R. Scarpa (2003b), Source Mechanisms of Explosions at Stromboli Volcano, Italy, Determined from Moment-Tensor Inversions of Very-Long-Period Data, *J. Geophys. Res.*, *108*(B1), 2019-2045, doi: 10.1029/2002JB001919.

Chouet, B., P. Dawson, and A. Arciniega-Ceballos (2005), Source Mechanism of Vulcanian Degassing at Popocatépetl Volcano, Mexico, Determined from Waveform Inversions of Very Long Period Signals, *Journal of Geophysical Research*, *110*(B7), 7301-7324, doi: 10.1029/2004jb003524.

Chouet, B., P. Dawson, and M. Nakano (2006), Dynamics of Diffusive Bubble Growth and Pressure Recovery in a Bubbly Rhyolitic Melt Embedded in an Elastic Solid, *Journal of Geophysical Research*, *111*(B7), 310-333, doi: 10.1029/2005jb004174.

Chouet, B., P. Dawson, and M. Martini (2008), Shallow-Conduit Dynamics at Stromboli Volcano, Italy, Imaged from Waveform Inversions, *Geological Society, London, Special Publications*, *307*(1), 57-84, doi: 10.1144/sp307.5.

Chouet, B., P. Dawson, M. R. James, and S. J. Lane (2010), Seismic Source Mechanism of Degassing Bursts at Kilauea Volcano, Hawaii: Results from Waveform Inversion in the 10-50 S Band, *Journal of Geophysical Research*, *115*(B9), 9311-9332, doi: 10.1029/2009jb006661.

Chouet, B. A. (1996a), New Methods and Future Trends in Seismological Volcano Monitoring, in *Monitoring and Mitigation of Volcano Hazards*, edited by R. Scarpa and R. I. Tilling, pp. 23-97, Springer-Verlag, Berlin.

Chouet, B. A. (1996b), Long-Period Volcano Seismicity: Its Source an Use in Eruption Forecasting, *Nature*, *380*, 309-316, doi: 10.1038/380309a0.

Dawson, P. B., B. A. Chouet, and J. Power (2011), Determining the Seismic Source Mechanism and Location for an Explosive Eruption with Limited Observational Data: Augustine Volcano, Alaska, *Geophysical Research Letters*, *38*(3), 3302-3312, doi: 10.1029/2010gl045977.

Falsaperla, S., H. Langer, and S. Spampinato (1998), Statistical Analyses and Characteristics of Volcanic Tremor on Stromboli Volcano (Italy), *Bulletin of Volcanology*, *60*(2), 75-88.

Fee, D., and M. Garcés (2007), Infrasonic Tremor in the Diffraction Zone, *Geophysical Research Letters*, *34*(16), 16826-16841, doi: 10.1029/2007gl030616.

Fee, D., A. Steffke, and M. Garces (2010), Characterization of the 2008 Kasatochi and Okmok Eruptions Using Remote Infrasound Arrays, *Journal of Geophysical Research*, *115*, 10-26, doi: 10.1029/2009jd013621.

Flynn, L., R. Wright, H. Garbeil, A. Harris, and E. Pilger (2002), A Global Thermal Alert System Using Modis: Initial Results from 2000-2001, *Advances in Environmental Monitoring and Modelling*, *1*(1), 37-69.

Garcés, M. A., M. T. Hagerty, and S. Y. Schwartz (1998), Magma Acoustics and Time-Varying Melt Properties at Arenal Volcano, Costa Rica, *Geophysical Research Letters*, *25*(13), 2293-2296, doi: 10.1029/98gl01511.

Genco, R., and M. Ripepe (2010), Inflation-Deflation Cycles Revealed by Tilt and Seismic Records at Stromboli Volcano, *Geophysical Research Letters*, *37*(12), 2302-2317, doi: 10.1029/2010gl042925.

Gilbert, J. S., and S. J. Lane (2008), The Consequences of Fluid Motion in Volcanic Conduits, *Geological Society of London Special Publications*, *307*(1), 1-10, doi: 10.1144/sp307.1.

Green, D. N., J. Neuberg, and V. Cayol (2006), Shear Stress Along the Conduit Wall as a Plausible Source of Tilt at Soufrière Hills Volcano, Montserrat, *Geophysical Research Letters*, *33*(10), 10306-10321, doi: 10.1029/2006gl025890.

Hagerty, M. T., S. Y. Schwartz, M. A. Garcés, and M. Protti (2000), Analysis of Seismic and Acoustic Observations at Arenal Volcano, Costa Rica, 1995-1997, *Journal of Volcanology and Geothermal Research*, *101*(1-2), 27-65.

Harris, A., J. Dehn, and S. Calvari (2007), Lava Effusion Rate Definition and Measurement: A Review, *Bulletin of Volcanology*, *70*(1), 1-22.

Head, J. W., and L. Wilson (1989), Basaltic Pyroclastic Eruptions: Influence of Gas-Release Patterns and Volume Fluxes on Fountain Structure, and the Formation of Cinder Cones, Spatter Cones, Rootless Flows, Lava Ponds and Lava Flows, *Journal of Volcanology and Geothermal Research*, *37*(3-4), 261-271.

Iguchi, M., H. Yakiwara, T. Tameguri, M. Hendrasto, and J.-i. Hirabayashi (2008), Mechanism of Explosive Eruption Revealed by Geophysical Observations at the Sakurajima, Suwanosejima and Semeru Volcanoes, *Journal of Volcanology and Geothermal Research*, *178*(1), 1-9, doi: DOI: 10.1016/j.jvolgeores.2007.10.010.

James, M. R., S. J. Lane, B. Chouet, and J. S. Gilbert (2004), Pressure Changes Associated with the Ascent and Bursting of Gas Slugs in Liquid-Filled Vertical and Inclined Conduits, *Journal of Volcanology and Geothermal Research*, *129*(1-3), 61-82, doi: 10.1016/s0377-0273(03)00232-4.

Jaupart, C., and S. Vergniolle (1988), Laboratory Models of Hawaiian and Strombolian Eruptions, *Nature*, *331*(6151), 58-60.

Jaupart, C., and S. Vergniolle (1989), The Generation and Collapse of Foam Layer at the Roof of a Basaltic Magma Chamber *Journal of Fluid Mechanics*, *203*, 347-380.

Johnson, J. B., J. M. Lees, and E. I. Gordeev (1998), Degassing Explosions at Karymsky Volcano, Kamchatka, *Geophysical Research Letters*, *25*(21), 3999-4002.

Johnson, J. B., and J. M. Lees (2000), Plugs and Chugs-Seismic and Acoustic Observations of Degassing Explosions at Karymsky, Russia and Sangay, Ecuador, *Journal of Volcanology and Geothermal Research*, *101*(1-2), 67-82.

Johnson, J. B. (2003), Generation and Propagation of Infrasonic Airwaves from Volcanic Explosions, *Journal of Volcanology and Geothermal Research*, *121*, 1-14, doi: 10.1016/S0377-0273(02)00408-0.

Johnson, J. B., R. C. Aster, and P. R. Kyle (2004), Volcanic Eruptions Observed with Infrasound, *Geophysical Research Letters*, *31*, 1-4, doi: 10.1029/2004GL020020.

Johnson, J. B., and R. C. Aster (2005), Relative Partitioning of Acoustic and Seismic Energy During Strombolian Eruptions, *Journal of Volcanology and Geothermal Research*, *148*(3-4), 334-354.

Johnson, J. B. (2007), On the Relation between Infrasound, Seismicity, and Small Pyroclastic Explosions at Karymsky Volcano, *Journal of Geophysical Research*, *112*, 1-21, doi: 10.1029/2006JB004654.

Johnson, J. B., R. Sanderson, J. Lyons, R. Escobar-Wolf, G. Waite, and J. M. Lees (2009), Dissection of a Composite Volcanic Earthquake at Santiaguito, Guatemala, *Geophysical Research Letters*, *36*, 5476-54892, doi: 10.1029/2009gl039370.

Julian, B. R. (1994), Volcanic Tremor: Nonlinear Excitation by Fluid Flow, *Journal of Geophysical Research*, *99*(B6), 11,859-811,878, doi: 10.1029/93JB03129.

Kaufman, Y. J., C. O. Justice, L. P. Flynn, J. D. Kendall, E. M. Prins, L. Giglio, D. E. Ward, W. P. Menzel, and A. W. Setzer (1998), Potential Global Fire Monitoring from Eos-Modis, *Journal of Geophysical Research*, *103*, 97-112.

Kim, K., and J. M. Lees (2011), Finite-Difference Time-Domain Modeling of Transient Infrasonic Wavefields Excited by Volcanic Explosions, *Geophysical Research Letters*, *38*(6), 6804-6828, doi: 10.1029/2010gl046615.

Kinoshita, S. (2008), Tilt Measurement Using Broadband Velocity Seismograms, *Bulletin of the Seismological Society of America*, *98*(4), 1887-1897, doi: 10.1785/0120070230.

Kirkpatrick, R. J. (1976), Towards a Kinetic Model for the Crystallization of Magma Bodies, *Journal of Geophysical Research*, *81*(14), 2565-2571, doi: 10.1029/JB081i014p02565.

Kirkpatrick, R. J. (1977), Nucleation and Growth of Plagioclase, Makaopuhi and Alae Lava Lakes, Kilauea Volcano, Hawaii, *Geological Society of America Bulletin*, *88*(1), 78-84, doi: 10.1130/0016-7606(1977)88[78:NAGOPM]2.0.CO.

Lane, S. J., B. A. Chouet, J. C. Phillips, P. Dawson, G. A. Ryan, and E. Hurst (2001), Experimental Observations of Pressure Oscillations and Flow Regimes in an Analogue Volcanic System, *Journal of Geophysical Research*, *106*(B4), 6461-6476, doi: 10.1029/2000jb900376.

Lautze, N. C., A. J. L. Harris, J. E. Bailey, M. Ripepe, S. Calvari, J. Dehn, S. K. Rowland, and K. Evans-Jones (2004), Pulsed Lava Effusion at Mount Etna During 2001, *Journal of Volcanology and Geothermal Research*, *137*(1-3), 231-246.

Lees, J. M. (2004), Scattering from a Fault Interface in the Coso Geothermal Field, *Journal of Volcanology and Geothermal Research*, *130*, 61-75, doi: 10.1016/S0377-0273(03)00281-6.

Lees, J. M., E. I. Gordeev, and M. Ripepe (2004), Explosions and Periodic Tremor at Karymsky Volcano, Kamchatka, Russia, *Geophysical Journal International*, *158*(3), 1151-1167.

Lees, J. M., and M. Ruiz (2008), Non-Linear Explosion Tremor at Sangay, Volcano, Ecuador, *Journal of Volcanology and Geothermal Research*, *176*(1), 170-178.

Lipman, P. W., N. G. Banks, and J. M. Rhodes (1985), Degassing-Induced Crystallization of Basaltic Magma and Effects on Lava Rheology, *Nature*, *317*(6038), 604-607.

Lodato, L., L. Spampinato, A. Harris, S. Calvari, J. Dehn, and M. Patrick (2007), The Morphology and Evolution of the Stromboli 2002–2003 Lava Flow Field: An Example of a Basaltic Flow Field Emplaced on a Steep Slope, *Bulletin of Volcanology*, *69*, 661–679, doi: 10.1007/s00445-006-0101-6.

Lokmer, I., and C. J. Bean (2010), Properties of the near-Field Term and Its Effect on Polarisation Analysis and Source Locations of Long-Period (Lp) and Very-Long-Period (Vlp) Seismic Events at Volcanoes, *Journal of Volcanology and Geothermal Research*, *192*(1-2), 35-47, doi: 10.1016/j.jvolgeores.2010.02.008.

Lumpkin, G. R. (2006), Ceramic Waste Forms for Actinides, *ELEMENTS*, *2*(6), 365-372, doi: 10.2113/gselements.2.6.365.

Lyons, J., G. Waite, W. Rose, and G. Chigna (2010), Patterns in Open Vent, Strombolian Behavior at Fuego Volcano, Guatemala, 2005–2007, *Bulletin of Volcanology*, *72*(1), 1-15, doi: 10.1007/s00445-009-0305-7.

Lyons, J. J., J. B. Johnson , G. P. Waite, and W. I. Rose (2007), Observations of Cyclic Strombolian Eruptive Behavior at Fuego Volcano, Guatemala Reflected in the Seismo-Acoustic Record, *Eos Transactions, American Geophysical Union*, *88*(52).

Lyons, J. J., and G. P. Waite (2011), Dynamics of Explosive Volcanism at Fuego Volcano Imaged with Very-Long-Period Seismicity, *Journal of Geophysical Research*, *in press*, doi: 10.1029/2011JB008521.

Martin, D. P., and W. I. Rose (1981), Behavioral Patters of Fuego Volcano, Guatemala, *Journat of Volcanology and Geothermal Research*, *10*, 67-81.

Matoza, R. S., M. A. H. Hedlin, and M. A. Garcés (2007), An Infrasound Array Study of Mount St. Helens, *Journal of Volcanology and Geothermal Research*, *160*(3-4), 249-262, doi: 10.1016/j.jvolgeores.2006.10.006

McGreger, A. D., and J. M. Lees (2004), Vent Discrimination at Stromboli Volcano, Italy, *Journal of Volcanology and Geothermal Research*, *137*, 169– 185, doi: 10.1016/j.jvolgeores.2004.05.007.

McNutt, S. R. (1986), Observations and Analysis of B-Type Earthquakes, Explosions, and Volcanic Tremor at Pavlof Volcano, Alaska, *Bulletin of the Seismological Society of America*, *76*(1), 153-175.

McNutt, S. R. (2005), Volcanic Seismology, *Annual Review of Earth and Planetary Sciences*, *33*(1), 461-491, doi: doi:10.1146/annurev.earth.33.092203.122459.

McTigue, D. F., and P. Segall (1988), Displacements and Tilts from Dip-Slip Faults and Magma Chambers beneath Irregular Surface Topography, *Geophysical Research Letters*, *15*(6), 601-604, doi: 10.1029/GL015i006p00601.

Melnik, O., and R. S. J. Sparks (1999), Nonlinear Dynamics of Lava Dome Extrusion, *Nature*, *402*, 37-41.

Meo, M., U. Tammaro, and P. Capuano (2008), Influence of Topography on Ground Deformation at Mt. Vesuvius (Italy) by Finite Element Modelling, *International Journal of Non-Linear Mechanics*, *43*(3), 178-186, doi: 10.1016/j.ijnonlinmec.2007.12.005.

Métrich, N., A. Bertagnini, P. Landi, and M. Rosi (2001), Crystallization Driven by Decompression and Water Loss at Stromboli Volcano (Aeolian Islands, Italy), *Journal of Petrology*, *42*(8), 1471-1490, doi: 10.1093/petrology/42.8.1471.

Métrich, N., P. Allard, N. Spilliaert, D. Andronico, and M. Burton (2004), 2001 Flank Eruption of the Alkali- and Volatile-Rich Primitive Basalt Responsible for Mount Etna's Evolution in the Last Three Decades, *Earth and Planetary Science Letters*, *228*(1-2), 1-17.

Mogi, K. (1958), Relations between the Eruptions of Various Volcanoes and the Deformations of the Ground Surface around Them, *Bull. Earthquake Res. Inst. Univ. Tokyo*, *36*, 99-134.

Mori, J., H. Patia, C. McKee, I. Itikarai, P. Lowenstein, P. De Saint Ours, and B. Talai (1989), Seismicity Associated with Eruptive Activity at Langila Volcano, Papua New Guinea, *Journal of Volcanology and Geothermal Research*, *38*(3-4), 243-255.

Mori, T., and M. Burton (2009), Quantification of the Gas Mass Emitted During Single Explosions on Stromboli with the So2 Imaging Camera, *Journal of Volcanology and Geothermal Research*, *188*(4), 395-400.

Murase, T., and A. R. McBirney (1973), Properties of Some Common Igneous Rocks and Their Melts at High Temperatures, *Geological Society of America Bulletin*, *84*(11), 3563-3592, doi: 10.1130/0016-7606.

Murata, K. J., C. Dondoli, and R. Saenz (1966), The 1963-65 Eruption of Irazú Volcano, Costa Rica (the Period of March 1963 to October 1964), *Bulletin Volcanologique*, *29*(2), 765-796.

Nadeau, P. A., J. L. Palma, and G. P. Waite (2011), Linking Volcanic Tremor, Degassing, and Eruption Dynamics Via So2 Imaging, *Geophysical Research Letters*, *38*(1), 1304-1312, doi: 10.1029/2010gl045820.

Nairn, I. A. (1976), Atmospheric Shock Waves and Condensation Clouds from Ngauruhoe Explosive Eruptions, *Nature*, *259*(5540), 190-192.

Neuberg, J., and T. Pointer (2000), Effects of Volcano Topography on Seismic Broad Band Waveforms, *Geophysical Journal International*, *143*(1), 239-248.

Nishimura, T. (2009), Ground Deformation Caused by Magma Ascent in an Open Conduit, *Journal of Volcanology and Geothermal Research*, *187*(3-4), 178-192, doi: 10.1016/j.jvolgeores.2009.09.001.

Ohminato, T., and B. A. Chouet (1997), A Free-Surface Boundary Condition for Including 3d Topography in the Finite-Difference Method, *Bull. Seism. Soc. Am.*, *87*(2), 494-515.

Ohminato, T., B. A. Chouet, P. Dawson, and S. Kedar (1998), Waveform Inversion of Very Long Period Impulsive Signals Associated with Magmatic Injection beneath Kilauea Volcano, *Journal of Geophysical Research*, *103*(B10), 23,839-823,862, doi: 10.1029/98JB01122.

Ohminato, T., M. Takeo, H. Kumagai, T. Yamashima, J. Oikawa, K. Etsuro, H. Tsuji, and T. Urabe (2006), Vulcanian Eruptions with Dominant Single Force Components Observed During the Asama 2004 Volcanic Activity in Japan, *Earth Planets Space*, *58*, 10-26.

Okada, Y. (1985), Surface Deformation Due to Shear and Tensile Faults in a Half-Space, *Bulletin of the Seismological Society of America*, *75*(4), 1135-1154.

Parfitt, E. A., and L. Wilson (1994), The 1983-86 Pu'u `O'o Eruption of Kilauea Volcano, Hawaii: A Study of Dike Geometry and Eruption Mechanisms for a Long-Lived Eruption, *Journal of Volcanology and Geothermal Research*, *59*(3), 179-205.

Parfitt, E. A., and L. Wilson (1995), Explosive Volcanic Eruptions Ix. The Transition between Hawaiian-Style Lava Fountaining and Strombolian Explosive Activity, *Geophysical Journal International*, *121*(1), 226-232, doi: doi:10.1111/j.1365-246X.1995.tb03523.x.

Parfitt, E. A. (2004), A Discussion of the Mechanisms of Explosive Basaltic Eruptions, *Journal of Volcanology and Geothermal Research*, *134*(1-2), 77-107.

Parks, M. M., J. Biggs, T. A. Mather, D. M. Pyle, F. Amelung, M. L. Monsalve, and L. N. Medina (2011), Co-Eruptive Subsidence at Galeras Identified During an Insar Survey of Colombian Volcanoes (2006-2009), *Journal of Volcanology and Geothermal Research*, *202*(3-4), 228-240, doi: 10.1016/j.jvolgeores.2011.02.007.

Patrick, M. R., J. L. Smellie, A. J. L. Harris, R. Wright, K. Dean, P. Izbekov, H. Garbeil, and E. Pilger (2005), First Recorded Eruption of Mount Belinda Volcano (Montagu Island), South Sandwich Islands, *Bulletin of Volcanology*, *67*(5), 415-422.

Ripepe, M., M. Rossi, and G. Saccorotti (1993), Image Processing of Explosive Activity at Stromboli, *Journal of Volcanology and Geothermal Research*, *54*(3-4), 335-351.

Rodgers, P. W. (1968), The Response of the Horizontal Pendulum Seismometer to Rayleigh and Love Waves, Tilt, and Free Oscillations of the Earth, *Bulletin of the Seismological Society of America*, *58*(5), 1385-1406.

Rodríguez, L. A., I. M. Watson, W. I. Rose, Y. K. Branan, G. J. S. Bluth, G. Chigna, O. Matías, D. Escobar, S. A. Carn, and T. P. Fischer (2004), So2 Emissions to the Atmosphere from Active Volcanoes in Guatemala and El Salvador, 1999-2002, *Journal of Volcanology and Geothermal Research*, *138*(3-4), 325-344, doi: 10.1016/j.jvolgeores.2004.07.008.

Roggensack, K. (2001), Unraveling the 1974 Eruption of Fuego Volcano (Guatemala) with Small Crystals and Their Young Melt Inclusions, *Geology*, *29*(10), 911–914.

Rose, W., A. T. J. Anderson, L. G. Woodruff, and S. B. Bonis (1978), The October 1974 Basaltic Tephra from Fuego Volcano: Description and History of the Magma Body., *Journal of Volcanology and Geothermal Research*, *4*, 3-53.

Rose, W. I., Jr, R. E. Stoiber, and L. L. Malinconico (1982), Eruptive Gas Compositions and Fluxes of Explosive Volcanoes: Budget of S and Cl Emitted from Fuego Volcano, Guatemala in *Andesites: Orogenic Andesites and Related Rocks*, edited by R. S. Thorpe, pp. 669-676, Wiley, New York, NY.

Rose, W. I. J., A. T. J. Anderson, L. G. Woodruff, and S. B. Bonis (1978), The October 1974 Basaltic Tephra from Fuego Volcano: Description and History of the Magma Body., *Journal of Volcanology and Geothermal Research*, *4* (1-2), 3-53.

Rowe, C. A., R. C. Aster, P. R. Kyle, J. W. Schlue, and R. R. Dibble (1998), Broadband Recording of Strombolian Explosions and Associated Very-Long-Period Seismic Signals on Mount Erebus Volcano, Ross Island, Antarctica, *Geophysical Research Letters*, *25*(13), 2297-2300, doi: 10.1029/98gl01622.

Rowe, C. A., R. C. Aster, P. R. Kyle, R. R. Dibble, and J. W. Schlue (2000), Seismic and Acoustic Observations at Mount Erebus Volcano, Ross Island, Antarctica, 1994-1998, *Journal of Volcanology and Geothermal Research*, *101*(1-2), 105-128.

Ruiz, M., J. Lees, and J. Johnson (2006), Source Constraints of Tungurahua Volcano Explosion Events, *Bulletin of Volcanology*, *68*(5), 480-490.

Schlindwein, V., J. Wassermann, and F. Scherbaum (1995), Spectral Analysis of Harmonic Tremor Signals at Mt. Semeru Volcano, Indonesia *Geophysical Research Letters*, *22*(13), 1685-1688.

Shinohara, H. (2008), Excess Degassing from Volcanoes and Its Role on Eruptive and Intrusive Activity, *Reviews of Geophysics*, *46*, 67-91, doi: 10.1029/2007rg000244.

Sisson, T. W., and G. D. Layne (1993), H20 in Basalt and Basaltic Andesite Glass Inclusions from Four Subduction-Related Volcanoes, *Earth and Planetary Science Letters*, *117*, 619-635.

Smithsonian Institution (1999), Global Volcanism Program, *12(1,8)*, 78-79.

Sparks, R. S. J., and H. Pinkerton (1978), Effect of Degassing on Rheology of Basaltic Lava, *Nature*, *276*(5686), 385-386.

Sparks, R. S. J. (2003), Dynamics of Magma Degassing *Volcanic degassing*, 5-22.

Stasiuk, M. V., J. Barclay, M. R. Carroll, C. Jaupart, J. C. Ratté, R. S. J. Sparks, and S. R. Tait (1996), Degassing During Magma Ascent in the Mule Creek Vent (USA), *Bulletin of Volcanology*, *58*(2), 117-130, doi: 10.1007/s004450050130.

Stix, J., R. C. Torres, L. Narváez M, G. P. Cortés J, J. A. Raigosa, D. Gómez M, and R. Castonguay (1997), A Model of Vulcanian Eruptions at Galeras Volcano, Colombia, *Journal of Volcanology and Geothermal Research*, *77*(1-4), 285-303, doi: 10.1016/S0377-0273(96)00100-X.

Swanson, D. A., W. A. Duffield, D. B. Jackson, and D. W. Peterson (1979), Chronological Narrative of the 1969-71 Mauna Ulu Eruption of Kilauea Volcano, Hawaii, edited by U. S. D. o. t. Interior, U.S. Government Printing Office, Washington, D.C. .

Tait, S., C. Jaupart, and S. Vergniolle (1989), Pressure, Gas Content and Eruption Periodicity of a Shallow, Crystallising Magma Chamber *Earth and Planetary Science Letters*, *92*, 107-123.

Vallance, J. W., L. Siebert, W. I. Rose, J. R. Girón, and N. G. Banks (1995), Edifice Collapse and Related Hazards in Guatemala, *Journal of Volcanology and Geothermal Research*, *66*(1-4), 337-355, doi: 10.1016/0377-0273(94)00076-s.

Vallance, J. W., S. P. Schilling, O. Matías, W. I. Rose, and H. M.M. (2001), Volcano Hazards at Fuego and Acatenango, Guatemala, *U.S. Geological Survey Open-File Report*, *01-431*.

Vergniolle, S., and C. Jaupart (1986), Separated Two-Phase Flow and Basaltic Eruptions, *Journal of Geophysical Research*, *91*(B12), 12842-12860.

Vergniolle, S., and C. Jaupart (1990), Dynamics of Degassing at Kilauea Volcano, Hawaii, *Journal of Geophysical Research*, *95*, 1290-1302.

Vergniolle, S., and G. Brandeis (1994), Origin of the Sound Generated by Strombolian Explosions, *Geophysical Research Letters*, *21*(18), 1959-1962.

Voight, B., et al. (1999), Magma Flow Instability and Cyclic Activity at Soufriere Hills Volcano, Montserrat, British West Indies, *SCIENCE*, *283*(5405), 1138-1142.

Voight, B., et al. (2000), Deformation and Seismic Precursors to Dome-Collapse and Fountain-Collapse Nuées Ardentes at Merapi Volcano, Java, Indonesia, 1994-1998, *Journal of Volcanology and Geothermal Research*, *100*(1-4), 261-287, doi: 10.1016/s0377-0273(00)00140-2.

Waite, G. P., B. A. Chouet, and P. B. Dawson (2008), Eruption Dynamics at Mount St. Helens Imaged from Broadband Seismic Waveforms: Interaction of the Shallow Magmatic and Hydrothermal Systems, *Journal of Geophysical Research*, *113*(B2), 2305-2323, doi: 10.1029/2007jb005259.

Waite, G. P., and J. J. Lyons (2009), Relative Slowness Estimates for Locations of Repeating Low-Frequency Earthquakes and Narrow-Band Tremor at Fuego Volcano, Guatemala, *Eos Transactions, American Geophysical Union*, *90(52)*, Fall Meet. Suppl., Abstract V31G-08.

Wallace, P. J. (2005), Volatiles in Subduction Zone Magmas: Concentrations Anf Fluxes Based on Melt Inclusion and Volcanic Gas Data, *Journal of Volcanology and Geothermal Research*, *140*, 217-240, doi: 10.1016/j.jvolgeores.2004.07.023.

Werner, C., M. Doukas, and P. Kelly (2011), Gas Emissions from Failed and Actual Eruptions from Cook Inlet Volcanoes, Alaska, 1989–2006, *Bulletin of Volcanology*, *73*(2), 155-173, doi: 10.1007/s00445-011-0453-4.

Wielandt, E., and T. Forbriger (1999), Near-Field Seismic Displacement and Tilt Associated with the Explosive Activity of Stromboli, *Annals of Geophysics*, *42*, 407-416.

Wiens, D. A., S. H. Pozgay, P. J. Shore, A. W. Sauter, and R. A. White (2005), Tilt Recorded by a Portable Broadband Seismograph: The 2003 Eruption of Anatahan Volcano, Mariana Islands, *Geophysical Research Letters*, *32*(18), 18305-18310, doi: 10.1029/2005gl023369.

Wilson, L., and J. W. Head (1981), Ascent and Eruption of Basaltic Magma on the Earth and Moon *Journal of Geophysical Research*, *86*(B4), 2971-3001.

Wright, R., L. Flynn, H. Garbeil, A. Harris, and E. Pilger (2002), Automated Volcanic Eruption Detection Using Modis, *Remote Sensing of Environment*, *82*(1), 135-155.

Wright, R., and L. P. Flynn (2004), Space-Based Estimate of the Volcanic Heat Flux into the Atmosphere During 2001 and 2002, *Geology*, *32*(3), 189-192, doi: 10.1130/g20239.1.

Wright, R., L. P. Flynn, H. Garbeil, A. J. L. Harris, and E. Pilger (2004), Modvolc: Near-Real-Time Thermal Monitoring of Global Volcanism, *Journal of Volcanology and Geothermal Research*, *135*(1-2), 29-49.

Wright, R., S. A. Carn, and L. P. Flynn (2005), A Satellite Chronology of the May-June 2003 Eruption of Anatahan Volcano, *Journal of Volcanology and Geothermal Research*, *146*(1-3), 102-116.

Appendix A

%% Displacement from Fuego 2009 40T and 3ESPC broadband recordings, with loop through all large (>100 Pa @ station F900) explosions

```
clear all, close all
% Fuego 2009 data via winston_db and GISMO
% first identify the datasource
cd….
C:\Users\John\Documents\Data\Fuego_data_waveform_db\MATLAB_waveform_objects\2009
ds_mat=datasource('file','%s%s%04d%02d%02d.mat','station','channel','year','month','day');
%internet access of database ds_winston = datasource('winston','141.219.61.148',16022);
javaaddpath('C:\Users\John\Documents\MATLAB\usgs.jar');
load F09_a2_100pa_times; % this loads explosion start times as variable a2
load Fuego2009_scnlobject; % this loads all the station, channel, location objects for

% accessing the database, choosing the station of interest
fuego09_40T = [F9C];% F9A F900]; fuego09_3ESP = [F9SW];;
% fuego09_3ESP=[F9SW F9NE F9NW]; % same method for 3ESPC stations

% extract 2 hours of data around every explosion, integrate to displacement and save the new waveforms along with timing and station, channel metadata in a structured array
for t=1:length(a2)
   VLPstart=a2(t);
% this loads one hour of data before and after the explosion time
   VLPt1=VLPstart-(3600/86400);
   VLPt2=VLPstart+(3600/86400);
   timevec1=datestr(VLPt1);
   timevec2=datestr(VLPt2);

   % access waveforms (E,N,Z) for all the 40T stations
   for d = 1:length(fuego09_40T)
      data40 = waveform(ds_mat,fuego09_40T(d),timevec1, timevec2);
      t4=isempty(data40);
      if t4~=1
         data40=fix_data_length(demean(data40));
         sta=get(data40,'station');
         cha=get(data40,'channel');
         mattime40=get(data40,'TIMEVECTOR');
         sps=get(data40(1),'freq');
         stacha=horzcat(sta,cha);
         data40=get(data40,'data');
```

```
            % cumtraptz is a built-in MATLAB function that performs a cumulative
            trapezoidal numerical integration
            displ_data40T=cumtrapz(data40)/sps;
            %build a structured array of waveform data
            F09displ_40T(t,d).data=displ_data40T;
            F09displ_40T(t,d).timevec=mattime40;
            F09displ_40T(t,d).stacha=stacha;
          end
    end
end
cd C:\Users\John\Documents\Data\Tilt
save('F09displ_40T_F9C_fullsps_struct','F09displ_40T');
```

%% At this point a simple routine must be written to access the structured array of displacement waveforms for each station (not included) and then plotting and filtering can be done. During this data housekeeping, any bad data, extremely noisy traces, etc. are thrown out and the stacks of the unfiltered, unshifted, full sample rate displacement waveforms are stacked using the MATLAB 'sum' command.

%% This code calculates the tilt transfer factor that allows calculation of tilt from displacement after filtering below the natural period of the instrument.

```
clear all
close all
% compute amplification factor
% use the Guralp CMG-40T seismometer poles and zeros
p=[complex(-23.56e-3,23.56e-3),complex(-23.56e-3,-23.56e-3),-50];
z=[0 0 159];
% convert poles and zeros to radians/sec
z=z*2*pi;
p=p*2*pi;

%normalization factor
normfac=-0.314;
% convert by multiplying by (2pi)^(numpoles - numzeros)
% since there are equal numbers of poles and zeros, there is nothing to do here

% set the frequency vector
f=logspace(-4,0,1000);
% convert from Hz to radians/sec
w=2*pi*f;

% eq(2) from Aoyama and Oshima (2008, GRL)
```

```
num=(i*w-z(1)).*(i*w-z(2)).*(i*w-z(3));
den=(i*w-p(1)).*(i*w-p(2)).*(i*w-p(3));
Cv=normfac*num./den;

% and eq(1) from Aoyama and Oshima (2008, GRL)
tilt=1e-6; %  [micro radians]
Ct=Cv.*(-9.8*tilt./w.^2); % units [m rad/s^2]/[rad^2/s^2]
ampfac=abs(Ct)*1e3; % convert units from m to mm
loglog(f,ampfac)
ylabel('amplitude [mm]')
xlabel('frequency [Hz]')
hold on
%%
clear all

% compute amplification factor for Guralp CMG-3ESPC
% use the seismometer poles and zeros
p=[complex(-11.78e-3,11.78e-3),complex(-11.78e-3,-11.78e-3),-160,-80,-180];
z=[0 0];
% convert poles and zeros to radians
z=z*2*pi;
p=p*2*pi;
%normalization factor
normfac=2304000;
% convert by multiplying by (2pi)^(numpoles - numzeros)
normfac=normfac*(2*pi)^3;

% set the frequency)
f=logspace(-4,0,1000);
w=2*pi*f;

% eq(2) from Aoyama and Oshima (2008, GRL)
num=(i*w-z(1)).*(i*w-z(2));
den=(i*w-p(1)).*(i*w-p(2)).*(i*w-p(3)).*(i*w-p(4)).*(i*w-p(5));
Cv=normfac*num./den;

% and eq(1) from Aoyama and Oshima (2008, GRL)
tilt=1e-6; %  [micro radians]
Ct=Cv.*(-9.8*tilt./w.^2);  % units [m rad/s^2]/[rad^2/s^2]
ampfac=abs(Ct)*1e3; % convert units from m to mm
loglog(f,ampfac,'r--')
ylim([1e-4 2])

legend('40T','3ESPC')
```

```
title('conversion factor for long period tilt mm/\murad')
%%
% compute the factor the simple Genco & Ripepe way
nat=1/30;
nat=2*pi*nat;
T40ampfac=1/(1e3*nat.^2/9.8)
hold on;
loglog(1/500,T40ampfac,'ob')

nat=1/60;
nat=2*pi*nat;
ESPC3ampfac=1/(1e3*nat.^2/9.8)
loglog(1/500,ESPC3ampfac,'or')
ylim([10^-3 10^1])
xlim([10^-4 10^0])
grid minor
%%
% loglog([1/30 1/30],[1e-4 10],'k--')
% loglog([1/60 1/60],[1e-4 10],'k--')
```

%% Details of filtering, decimation and plotting routine in MATLAB

% note that within the structured array access routine (just housekeeping) that we stack the unshifted, unfiltered, full sample rate two-hour traces using the MATLAB 'sum' command.

% Decimate is a MATLAB command and includes a low-pass filter, here we set the filter type to 'FIR' which is a one-pass FIR filter instead of the default Chebyshev IIR filter, although both were tried and caused no noticeable change in displacement waveform.

```
F900displ_stackEdeci = decimate(F900displ_stackE,10,'fir');
```

% After decimation, a single pass (causal) low-pass filter is applied, the details of the filter routine are included below.

```
F900displ_stackElp = lpf1(F900displ_stackEdeci,10,1/30,1/10,1);
F900displ_stackNdeci = decimate(F900displ_stackN,10,'fir');
F900displ_stackNlp = lpf1(F900displ_stackNdeci,10,1/30,1/10,1);

F9Adispl_stackEdeci = decimate(F9Adispl_stackE,10,'fir');
F9Adispl_stackElp = lpf1(F9Adispl_stackEdeci,10,1/30,1/10,1);
F9Adispl_stackNdeci = decimate(F9Adispl_stackN,10,'fir');
F9Adispl_stackNlp = lpf1(F9Adispl_stackNdeci,10,1/60,1/20,1);

F9NWdispl_stackEdeci = decimate(F9NWdispl_stackE,10,'fir');
F9NWdispl_stackElp = lpf1(F9NWdispl_stackEdeci,10,1/30,1/10,1);
F9NWdispl_stackNdeci = decimate(F9NWdispl_stackN,10,'fir');
F9NWdispl_stackNlp = lpf1(F9NWdispl_stackNdeci,10,1/60,1/20,1);

F9NEdispl_stackEdeci = decimate(F9NEdispl_stackE,10,'fir');
```

```
F9NEdispl_stackElp = lpf1(F9NEdispl_stackEdeci,10,1/30,1/10,1);
F9NEdispl_stackNdeci = decimate(F9NEdispl_stackN,10,'fir');
F9NEdispl_stackNlp = lpf1(F9NEdispl_stackNdeci,10,1/30,1/10,1);
```

%% Low-pass filtering routine

```
function y=lpf1(x,fs,fl,fh,np)
% y : lpf1(x,fs,fl,fh,np);
% x : original data column vector
% fs : sampling frequency
% fl : cut frequency
% fh : stop frequency
% rp : pass (3dB)
% rs : stop (50dB)
% np = 1 is single pass (causal); np=2 is double pass (non-causal)
% n : order of the Butter filter (displayed in command window when executed)
% y : filtered data

wp=2*fl/fs; % pass band corner
ws=2*fh/fs; % stop band corner
rp=3; rs=50;
[n,wn]=buttord(wp,ws,rp,rs)
[b,a]=butter(n,wn);
if (np==1)
   y=filter(b,a,x);
else
   y=filtfilt(b,a,x);
end
```

Appendix B

Dear Author,

Journal title:	Bulletin of Volcanology
Article title:	Patterns in Open vent, Strombolian Behavior at Fuego Volcano, Guatemala, 2005-2007
DOI:	10.1007/s00445-009-0305-7
Corresponding Author:	J.J. Lyons
Copyright transferred to:	Springer-Verlag
Transferred on:	Tue Jun 23 17:42:19 CEST 2009

Please note: This e-mail is a confirmation of your copyright transfer and was sent to you only for your own records.

The copyright to this article is transferred to

"Springer-Verlag"

(for U.S. government employees: to the extent transferable) effective if and when the article is accepted for publication. The author warrants that his/her contribution is original and that he/she has full power to make this grant. The author signs for and accepts responsibility for releasing this material on behalf of any and all co-authors. The copyright transfer covers the exclusive right to reproduce and distribute the article, including reprints, translations, photographic reproductions, microform, electronic form (offline, online) or any other reproductions of similar nature.

An author may self-archive an author-created version of his/her article on his/her own website. He/she may also deposit this version on his/her institution's and funder's (funder designated) repository at the funder's request or as a result of a legal obligation, including his/her final version, provided it is not made publicly available until after 12 months of official publication. He/she may not use the publisher's PDF version which is posted on www.springerlink.com for the purpose of self-archiving or deposit. Furthermore, the author may only post his/her version provided acknowledgement is given to the original source of publication and a link is inserted to the published article on Springer's website.

The link must be accompanied by the following text: "The original publication is available at www.springerlink.com".

The author is requested to use the appropriate DOI for the article. Articles disseminated via www.springerlink.com are indexed, abstracted and referenced by many abstracting and information services, bibliographic networks, subscription agencies, library networks and consortia.

After transfer of the copyright by the corresponding author, changes of authorship or in the order of the authors listed will not be accepted by Springer.

This is an automated e-mail; please do not reply to this account. If you have any questions, please go to our help pages.

Thank you very much.

Kind regards,
Springer Author Services